



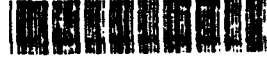
2
111

UNCLASSIFIED

SECURITY CLASSIFICATION OF THIS PAGE

REPORT DOCUMENTATION PAGE				Form Approved OMB No. 0704-0188	
1a. REPORT SECURITY CLASSIFICATION UNCLASSIFIED		1b. RESTRICTIVE MARKINGS			
2a. SECURITY CLASSIFICATION AUTHORITY AUG 10 1993		3. DISTRIBUTION/AVAILABILITY OF REPORT Approved for public release Distribution unlimited			
2b. DECLASSIFICATION/DOWNGRADING SCHEDULE		4. PERFORMING ORGANIZATION REPORT NUMBER(S) USAF -3-92		5. MONITORING ORGANIZATION REPORT NUMBER(S) TR-93-09	
6a. NAME OF PERFORMING ORGANIZATION University College, Galway		6b. OFFICE SYMBOL (If applicable)	7a. NAME OF MONITORING ORGANIZATION EOARD		
6c. ADDRESS (City, State, and ZIP Code) Department of Physics, University College, Galway, Ireland			7b. ADDRESS (City, State, and ZIP Code) Box 14, FPO NY 09510		
8a. NAME OF FUNDING/SPONSORING ORGANIZATION EOARD		8b. OFFICE SYMBOL (If applicable) LRE	9. PROCUREMENT INSTRUMENT IDENTIFICATION NUMBER		
8c. ADDRESS (City, State, and ZIP Code) Box 14, FPO New York 09510			10. SOURCE OF FUNDING NUMBERS		
	PROGRAM ELEMENT NO. 61102 F	PROJECT NO. 2301	TASK NO. D1	WORK UNIT ACCESSION NO.	
11. TITLE (Include Security Classification) Spectroscopy of crystalline, glass, and ceramic media doped with cobalt and nickel. (Unclassified)					
12. PERSONAL AUTHOR(S) Glynn, Thomas J.					
13a. TYPE OF REPORT Final		13b. TIME COVERED FROM 88/9/30 TO 92/9/29		14. DATE OF REPORT 92.5.3	
16. SUPPLEMENTARY NOTATION					
17. COSATI CODES			18. SUBJECT TERMS (Continue on reverse if necessary and identify by block number)		
FIELD	GROUP	SUB-GROUP	Tunable laser media, optical spectroscopy, crystalline media doped with Co, Ni, Cr.		
19. ABSTRACT (Continue on reverse if necessary and identify by block number)					
Studies of media doped with Ni, Co, Cr ions, aimed at identifying new materials for tunable laser applications, are presented. With Co ²⁺ -doping, some new possibilities, based mainly on tetrahedrally-coordinated Co ²⁺ ions and emission from higher excited states of octahedrally-coordinated systems, have been documented. The range of Ni ²⁺ -doped materials studied included MgNb ₂ O ₆ , ZnNb ₂ O ₆ , and Mg ₂ SiO ₄ (in which the luminescence is thermally quenched) and the spinels LiAl ₅ O ₈ and ZnAl ₂ O ₄ (which show evidence of high Q.E. at room temperature). Excited state absorption measurements will be necessary to assess fully these materials. Cr-doped media, added later to the project brief, included materials doped with Cr ³⁺ , Cr ⁴⁺ (and both). None of the Cr ⁴⁺ -doped samples Y ₂ SiO ₃ , Gd ₂ SiO ₅ , and Ca ₃ (VO ₄) ₂ had a luminescence Q.E. comparable to that of forsterite. Two samples doped with Cr ³⁺ ions, BiGaO ₃ and LaSr ₂ Ga ₁₁ O ₂₀ show some promise for laser applications but their potential region of operation overlaps that already covered by Ti:sapphire. A novel pumping possibility is described for BiGaO ₃ .					
20. DISTRIBUTION/AVAILABILITY OF ABSTRACT <input checked="" type="checkbox"/> UNCLASSIFIED UNLIMITED <input type="checkbox"/> SAME AS RPT. <input type="checkbox"/> DTIC USERS			21. ABSTRACT SECURITY CLASSIFICATION UNCLASSIFIED		
22a. NAME OF RESPONSIBLE INDIVIDUAL Dr. Eirug Davies			22b. TELEPHONE (Include Area Code) 44-01-409-6318	22c. OFFICE SYMBOL EOARD/LRE	

93-18765



93 8 11 01 9

INTRODUCTION

Rapid advances are being made in the development of new solid-state laser systems in the near infrared (0.7 - 2.5 μm) - based mainly on crystalline materials which are doped with one or more optically active ions (e.g. Ho, Tm, Cr:YAG). At the visible end of this spectral region, the Ti:sapphire laser is now commercially available but, further into the IR, most systems are based on rare-earth ions. Transition metal ions with their strong coupling to their environment offer the possibility of broadband tunable operation but despite many studies, centered mainly on Co^{2+} and Ni^{2+} -doped (and more recently Cr^{4+} -doped) materials, only a couple of efficient room temperature laser media, based on these dopant ions, have been developed. The aim of this project is to carry out further studies in this area, to investigate the spectroscopy of existing materials, and suggest guidelines or limitations on the development of new materials for tunable operation in the near infrared. The plan of research was simply to investigate the luminescence properties of new media doped with Ni, Co, (and eventually Cr) ions with the aim of identifying materials with suitable properties for this application.

The organisation of this report is as follows. Chapter 1 provides some general theoretical and background information to the project and is intended to provide the context and rationale for the project work. While the experimental results obtained with a wide range of glasses and ceramics were not very encouraging, this part of the work is summarised briefly in Chapter 2. The data on the various Co and Ni-doped materials is gathered together in Chapters 3 and 4, respectively. Chapter 5 is devoted to materials doped with chromium (Cr^{3+} , Cr^{4+}). Copies of various publications arising from the project are contained in the appendix, which follows the Conclusion.

DTIC QUALITY INSPECTED 3

Accession For	
NTIS	<input checked="" type="checkbox"/>
CRA&I	<input checked="" type="checkbox"/>
DTIC TAB	<input checked="" type="checkbox"/>
Unannounced	<input checked="" type="checkbox"/>
Justification	
By	
Distribution /	
Availability Codes	
Dist	Avail and/or Special
A-1	

CHAPTER I

1.1 Introduction.

The development of new tunable solid-state lasers (e.g. Cr-doped forsterite and alexandrite, Ti-doped sapphire) has stimulated a search for new materials doped with transition metal ions which emit efficient phonon-terminated broadband luminescence at room temperature. The principal results of this research are summarised in Tables 1-5, which also summarize the materials and important results identified in the present study. These tables indicate that the vibronic laser materials based on the transition metal ions are made mostly from oxide or fluoride single crystals doped with Ti^{3+} , Cr^{3+} , Cr^{4+} , Co^{2+} , or Ni^{2+} ions. The Cr^{4+} has emerged only in the last few years as a worthwhile laser centre in its own right which can extend the range beyond that of Cr^{3+} in the infrared and new crystal hosts are being sought which can stabilise this oxidation state. Because the outer (3d) electrons, responsible for the optical properties of these materials, are strongly influenced by the local environment, the optical transitions usually take place between levels which have different coupling to the lattice and this usually results in broadband emission (Fig. 1.1). The potential laser transition usually corresponds to emission from the lowest excited state to phonon levels of the ground state. Tables 1-5 provide a useful listing of all the systems¹⁻⁴¹ which have been considered in recent years for tunable laser action as well as, for those which have already lased, their tuning range.

Some general comments can be made on the results presented in these tables.

1. The effective tuning range (except for Ti^{3+} , Co^{2+} systems) is generally much reduced compared with that expected from the emission spectrum - mainly due to excited state absorption.
2. A large number of Cr-doped systems have lased fairly efficiently at room temperature. The most famous are GSGG, alexandrite, and forsterite, and these have been marketed commercially.
3. Systems doped with Ni^{2+} or Co^{2+} are much less numerous, because (i) there are not so many materials which can accept these divalent ions, and (ii) they give rise (in octahedral coordination, to lower energy emissions which are more likely to be quenched by non-radiative processes. Thus, these systems will often only lase at low temperatures (≤ 100 K).

Again, summarising these results in another way, Fig. 1.2 shows the emission domains which can be expected with each of these ions. Although Ti^{3+} and V^{2+} systems have been included for completeness in our review up to now, only Co^{2+} , Ni^{2+} , and Cr-doped systems were investigated in this work. From Fig. 1.2, it should be possible to find laser systems which

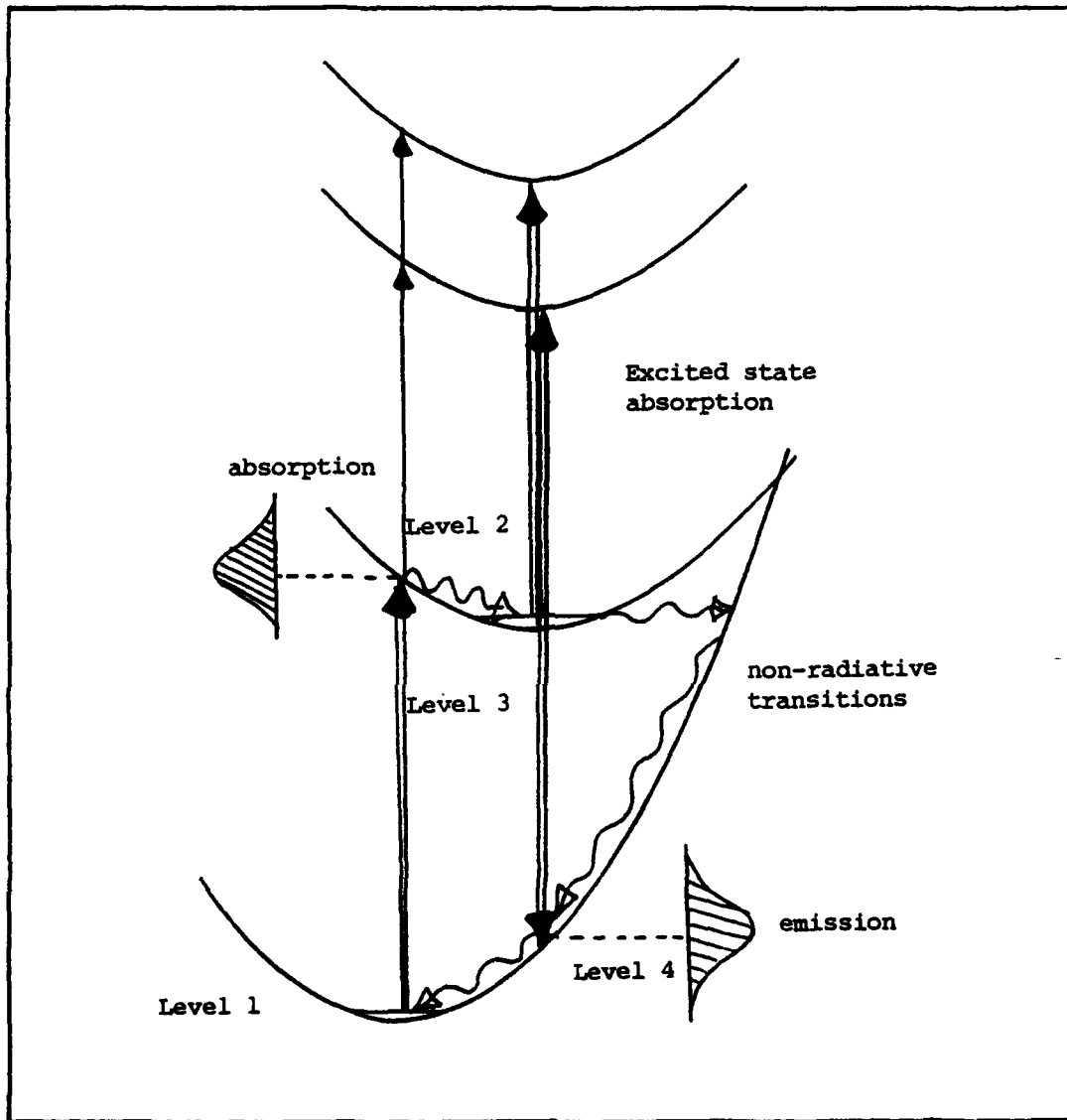


Fig. 1.1. Schematic diagram showing absorption, emission, non-radiative relaxation, and excited state absorption in a vibronic laser system.

TABLE 1.1 Cr-doped systems¹⁻¹⁴

Host matrix	Emission range (μm)	Tuning range (μm) at room temp.
Y ₃ Ga ₅ O ₁₂ (YGG)	0.65 - 0.87	0.73
Gd ₃ Ga ₅ O ₁₂ (GGG)	0.65 - 0.9	0.74 - 0.84
Gd ₃ (Sc,Ga) ₅ O ₁₂ (GSGG)	0.67 - 0.9	0.74 - 0.84
Gd ₃ Sc ₂ Al ₃ O ₁₂ (GSAG)	0.67 - 0.92	0.78
BeAl ₂ O ₄ (alexandrite)	0.67 - 0.83	0.70 - 0.82
CaY ₂ Mg ₂ Ge ₃ O ₁₂ (Camgar)	0.71 - 0.85	
Ca ₃ Al ₂ Ge ₃ O ₁₂	0.7 - 0.8	
MgY ₂ Mg ₂ Ge ₃ O ₁₂	0.71 - 0.9	
Be ₃ Al ₂ (SiO ₃) ₆ (emerald)	0.67 - 0.85	0.73 - 0.81
Mg ₂ SiO ₄ :Cr ⁴⁺	1.0 - 1.4	1.21 - 1.26
ZnWO ₄	0.8 - 1.3	1.03
LaMgAl ₁₁ O ₁₉ (LMA)	0.65 - 0.9	
MgAl ₂ O ₄	0.7 - 1.2	
C ₃ Ga ₂ Ge ₄ O ₁₂	0.87 - 1.2	
La ₃ Ga _{5.5} Ta _{0.5} O ₁₄	0.92 - 1.24	
La ₃ Ga ₅ GeO ₁₄	0.88 - 1.22	
La ₃ Ga ₅ SiO ₁₄	0.82 - 1.12	
KZnF ₃	0.71 - 0.9	0.76 - 0.86
Na ₃ Ga ₂ Li ₃ F ₁₂		0.74 - 0.84
SrAlF ₅	0.72 - 1.05	0.85 - 0.95
LiCaAlF ₆	0.65 - 1.0	0.72 - 0.84
K ₂ NaScF ₆	0.67 - 0.95	
Rb ₂ KGaF ₆	0.69 - 0.80	
Cs ₂ NaYCl ₆	0.83 - 1.25	
<u>New Materials</u>		
BiGaO ₃	0.68 - 0.75	
Mg ₂ SiO ₄ :Cr ³⁺	0.68 - 0.85	
LaSr ₂ Ga ₁₁ O ₂₀ :Cr ³⁺	0.69 - 1.1	
Y ₂ SiO ₅ :Cr ⁴⁺ (YSO)	1.15 - 1.5	
Gd ₂ SiO ₅ :Cr ⁴⁺ (GSO)	1.2 - 1.6	
Gd ₃ Sc ₂ Ga ₃ O ₁₂ :Cr ⁴⁺ (GSGG)		
Ca ₃ (VO ₄) ₂ :Cr ⁴⁺ (CVO)	1.16 - 1.40	

TABLE 1.2 - Ni²⁺-doped systems. ¹⁴⁻²⁹

Host matrix	Emission range (μm)	Tuning range (μm) at LN ₂ temp.
MgF ₂	1.5 - 1.95	1.61 - 1.74
MgO	1.2 - 1.5	1.316 - 1.409
CaY ₂ Mg ₂ Ge ₃ O ₁₂	1.3 - 1.8	1.46
Mg ₂ GeO ₄	1.35 - 1.9	
MgAl ₂ O ₄	1.1 - 1.5	
KMgF ₃	1.53 - 1.95	
KZnF ₃	1.53 - 2.0	
LaMgAl ₁₁ O ₁₉ (LMA)	0.95 - 1.4	
LaMgGa _x Al _{11-x} O ₁₉ (LMGA)	1.0 - 1.6	
GGG	1.3 - 1.8	
LaGaO ₃ (LGO)	1.1 - 1.5	
YAlO ₃ (YALO)	0.95 - 1.3	
RbCdF ₃	1.8 - 1.95	
MgCl ₂		
CdCl ₂		
CsMgCl ₃		
CsCdCl ₃		
<u>New materials</u>		
MgNb ₂ O ₆	1.65 - 1.8	
ZnNb ₂ O ₆	1.65 - 1.8	
ZnAl ₂ O ₄	1.05 - 1.5	
LiAl ₅ O ₈	0.90 - 1.50	
Mg ₂ SiO ₄	0.80 - 1.5 (two bands)	

TABLE 1.3 - Ti³⁺-doped systems. ³⁰⁻³²

Al ₂ O ₃	0.6 - 1.2	0.68 - 1.2
YAlO ₃	0.5 - 0.9	

TABLE 1.4 - Co²⁺-doped systems.³³⁻³⁷

Host matrix	Emission range (μm)	Tuning range (μm) at LN ₂ temp.
MgF ₂	1.5 - 2.5	1.51 - 2.4
KZnF ₃	1.5 - 2.5	1.65 - 2.18
KMgF ₃	1.5 - 2.5	1.62 - 1.9
Mg ₂ GeO ₄	1.4 - 2.8	
ZnGa ₂ O ₄	0.65 - 1.0	
<u>New materials</u>		
MgNb ₂ O ₆	0.82 - 1.20	
MgAl ₂ O ₄	0.7 - 1.5 (several bands)	
LiGa ₅ O ₈	0.65 - 1.6 (several bands)	
LiGaO ₂	0.94 - 1.16	
La ₃ Ga ₅ SiO ₁₄	0.65 - 0.9 (two bands)	

TABLE 1.5 - V²⁺-doped systems.³⁸⁻⁴¹

MgF ₂	1.0 - 1.4	1.07 - 1.15
KMgF ₃	0.9 - 1.2	(gain at 1.065)
CsCdF ₃	1.15 - 1.55	1.24 - 1.32
NaCl	1.4 - 2.5	
CsCdCl ₃	1.4 - 1.8	
RbMnF ₃	1.1 - 1.3	
KMnF ₃	1.08 - 1.23	

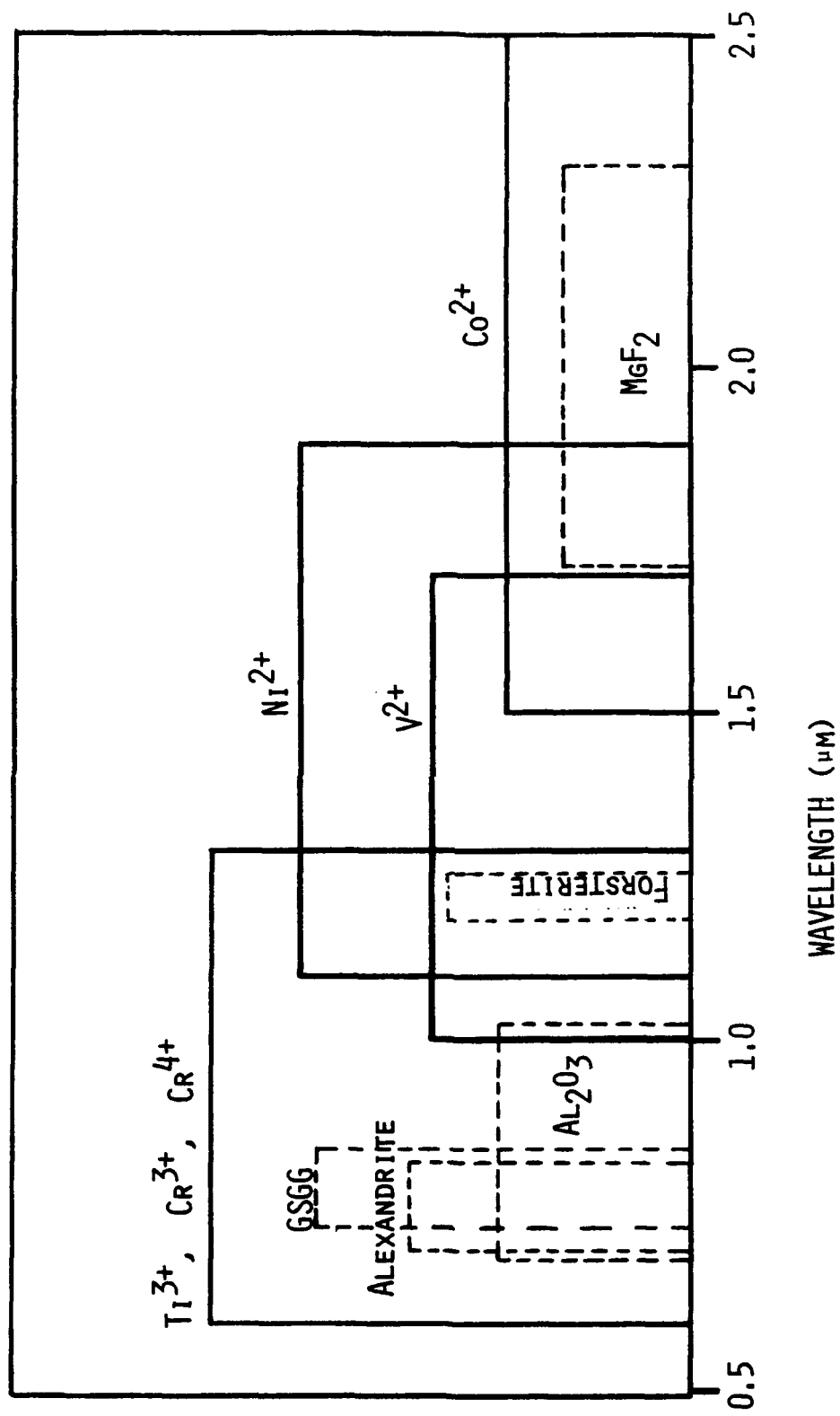


Fig. 1.2 Emission region (full lines) expected for various TM ions together with the tuning range (dashed lines) of commercial systems.

operate from about 1.1 to 1.9 μm with Ni^{2+} , from 0.7 to 2.5 μm with Co^{2+} , and from 0.65 to 1.4 μm for Cr doping, including tetrahedral coordination for Co^{2+} and the possibility of Cr^{4+} doping (also in tetrahedral sites).

1.2 Solid-state lasers vs tunable dye lasers

Research into new solid-state lasers in recent years has been driven by the following advantages⁴² which these systems can offer over dye lasers (besides their availability in wavelength regions which are not attainable at all by dye lasers).

1. Better photochemical stability under laser or flashlamp pumping.
2. Simpler to handle - no solvents or complicated flushing procedures.
3. Slope efficiencies of 10 - 60 %, better than many dye lasers.
4. They are true 4-level systems, which means lower laser thresholds.
5. They have broadband absorption spectra throughout the visible region, allowing pumping by flashlamps or other lasers.

Given the results shown in Tables 1-5, it is surprising that only a few of these laser systems are commercially available (Cr-doped alexandrite, GSGG, forsterite ; Ti-sapphire ; and $\text{MgF}_2:\text{Co}^{2+}$). There are several reasons for this anomaly.

1. Materials growth problems of congruency, stoichiometry, and dopant solubility which can make the optical quality unacceptable or the cost prohibitive.
2. Thermally-induced lensing or birefringence can degrade the laser performance.
3. Excited state absorption at the laser wavelength and non-radiative relaxation processes to the ground state.

It is clearly worthwhile, therefore, to continue the search for new materials by exploring the spectroscopy of new media, and re-examining previously discarded materials, so that luminescent processes in solids may be more deeply understood and reliable ground rules may be developed to guide in crystal growth programs.

While laser action has been achieved in several Co and Ni-doped materials at low temperatures, quenching mechanisms such as non-radiative relaxation and excited state absorption have prevented all systems based on these ions (except $\text{MgF}_2:\text{Co}$) from operating at room temperature. The purpose of this research project was to search for new tunable solid-state laser materials.

1.3 Theoretical background

The Tanabe-Sugano diagrams⁴³, which give the energy levels as a function of the (octahedral) crystal field strength, are shown in Fig. 1.3 for the important laser ions. The abscissa is the ratio Dq/B , where Dq is the local crystal field, assuming a point charge model, and B

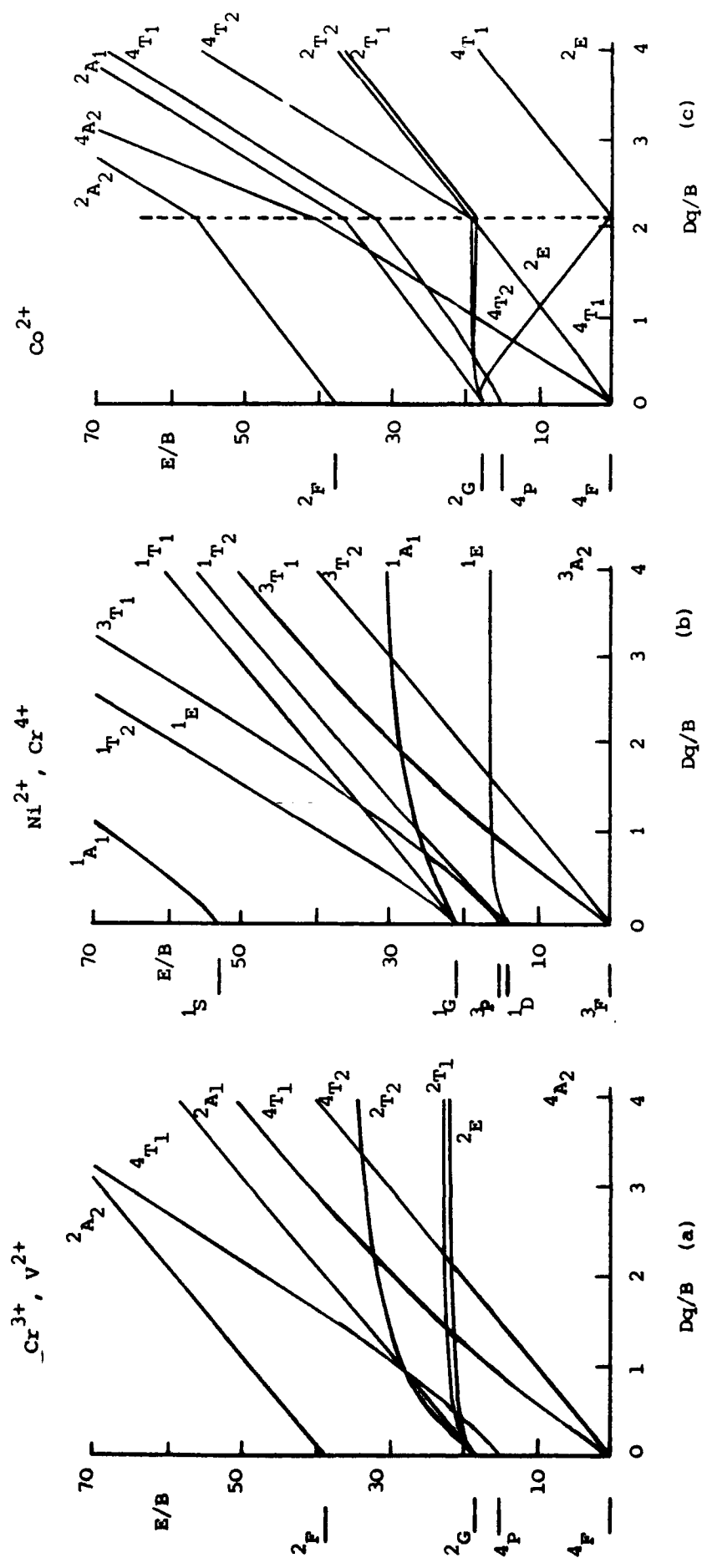


Fig. 1.3 Tanabe-Sugano diagrams for the TM ions of interest for vibronic lasers. (a) corresponds to a d^3 ion in an octahedral field with $B = 640 \text{ cm}^{-1}$, $C/B = 4.8$; (b) corresponds to d^8 , and can represent either Ni^{2+} in an octahedral site, or Cr^{4+} (d^2) in a tetrahedral site ($B = 890 \text{ cm}^{-1}$, $C/B = 4.4$); (c) corresponds to d^7 in an octahedral field ($B = 845$, $C/B = 4.5$). For Co^{2+} in a tetrahedral site, the crystal field split components of the ground 4F state are inverted.

is the Racah parameter which measures the intra-ion electron repulsion. These diagrams only give a crude estimate of the true situation since covalency effects, spin-orbit coupling, and lower symmetry fields at the impurity ion site, are not included. Although only approximations, they provide some insight and guidance in the search for laser media. For systems doped with Cr^{3+} and V^{2+} , the crossing point of the ${}^2\text{E}$ and ${}^4\text{T}_2$ levels takes place when $\text{Dq/B} = 2.3$; below this value, we have "low-field" systems in which the emitting state is the ${}^4\text{T}_2$ state and its coupling to the lattice is very different from that of the ground (${}^4\text{A}_2$) state, resulting in broad-band (tunable) emission. When $\text{Dq/B} < 2.3$, we have "high-field" behaviour (e.g. ruby) characterised by sharp line emission from the ${}^2\text{E}$ level to the ground state. Many broad-band laser systems correspond to the low-field case but where the ${}^4\text{T}_2 - {}^2\text{E}$ separation is so small that the quartet level is populated at room temperature. In this way, the long-lived ${}^2\text{E}$ level provides storage for the ${}^4\text{T}_2$ level with which it is in thermal equilibrium. (GSGG, alexandrite, and emerald are examples of this behaviour).

For systems doped with Ni^{2+} or Co^{2+} , the Dq/B values in typical hosts are such that the emission from the lower excited states are almost always in the form of broad bands at room temperature.

1.3.1 Non-radiative Processes

The non-radiative relaxation rate W_{NR} , which, together with the radiative rate, influences the overall fluorescence lifetime, is a complicated function of the Huang-Rhys parameter S , and of the frequency ν_a and the average number (N_a) of the modes involved in the transition⁴⁴ (see Chapter 3). It also depends on the matrix element $\langle \Gamma_a/\Gamma_p/\Gamma_b \rangle$ where Γ_a , Γ_b are the irreducible representations characterising the ground and the excited states respectively and Γ_p is the representation characterising the interacting phonon modes.

Considering this matrix element alone, some comments can be made for particular combinations of active ion and host lattice. The lower energy optical transitions occur between orbital states A_2 and T_2 in the case of Ni^{2+} and V^{2+} in low-field systems while they occur between states T_1 and T_2 in the case of Co^{2+} (see Fig. 1.3). Thus group theory analysis of the above matrix element for ions in octahedral site symmetry shows that only T_{1g} promoting modes can be efficient in the case of Ni^{2+} , Cr^{3+} and V^{2+} ions while A_{2g} , E_g , T_{1g} and/or T_{2g} can act in the case of Co^{2+} . Knowing that coupling to T_{1g} modes, which correspond to a simple rotation of the immediate ligands, is usually very weak, we can conclude, in agreement with experimental observations, that the non-radiative processes are much more efficient in the case of Co^{2+} than in the case of the other ions. In other words, the fluorescence quenching occurs at lower temperatures (generally < 100 K), in the Co^{2+} -doped systems [53] than in the same hosts doped by Ni^{2+} , Cr^{3+} or V^{2+} ions. Similar

symmetry considerations can be used to understand the increased non-radiative processes in the systems with lower local site symmetry, thus systems in which a larger range of phonon mode types can be involved. This is illustrated by the fact that the quenching temperatures of the infrared fluorescence lifetimes for Ni^{2+} or V^{2+} in cubic systems such as MgO and KMgF_3 are higher than for other hosts (MgF_2) where there is a tetragonal local site distortion. Although one might infer that cubic systems with octahedral local site symmetry should be preferable for laser purposes, considerations such as the oscillator strength of the transitions, are generally more important in the case of low symmetry systems, so that accurate predictions of the importance of the non-radiative processes in the laser properties of these materials still remain rather uncertain. Also the absence of possible T_{1g} distortions in some Cr^{3+} doped perovskites has led⁴⁵ to the inclusion of other T_{1g} -type modes involving complex motions of the ligands which are effective in promoting radiationless transitions, so that the above selection-rule is not very strict either for cubic systems.

Multiphonon non-radiative transition rates can be explained quite well, for trivalent lanthanide ions, in terms of well-known semi-empirical models, which describe the process in terms of the energy gap between the initial and final states, and empirical (lattice-dependent) constants.⁴⁶⁻⁴⁸ For example, a great deal of attention has been given to the determination of the radiative and nonradiative branching ratios out of the various levels of the 5D manifold of Eu^{3+} in solids. As a result, much is known about both the nature of excited-state interactions in such systems and the physical factors that influence them. In contrast, our understanding of the radiative and non-radiative transitions occurring between excited states of transition metal ions is poor. This is due mainly to the fact that the stronger interaction of these ions with their environment greatly complicates the problem of describing electron-phonon coupling. Unlike the trivalent lanthanides, the degree of electron-phonon coupling may also vary significantly among the different electronic states of the ion, resulting in dramatic differences in the nature of the interactions (both radiative and non-radiative) between different pairs of electronic states. This makes it impossible to generalize the description of the behaviour of multiphonon transitions in these systems in terms of "lattice constants". Also, relatively little detailed experimental information about transitions between excited states of 3d ions is available. For example, although excited-state absorption (ESA) processes in solid-state laser materials are important, in that they may adversely affect laser output, it is only recently that careful ESA measurements have been performed on 3d ions other than Cr^{3+} . The ESA of Ni^{2+} in MgF_2 ¹⁸ and MgO ,^{18,49} and V^{2+} in MgF_2 ³⁹ and KMgF_3 ³⁹ have now also been reported. Information on transitions between excited states of Ti^{2+} in MgCl_2 was obtained using excited-state excitation (ESE) measurements.⁵⁰ Still, these studies provide information only on radiative transitions between these excited states. From a practical standpoint, accessing information about non-radiative transitions between excited

states requires that the ion under investigation exhibit luminescence from more than one excited state, and that these states be coupled by radiative and or nonradiative processes. The only 3d ion shown to exhibit two metastable emitting states in a variety of lattice (e.g. oxides, chlorides, and fluorides)^{17,25,51} is Ni²⁺.

The first quasi four-level vibronic laser was demonstrated with Ni²⁺-doped MgF₂³⁸ and, since then, the optical properties of the Ni²⁺ ion in various solid state hosts have received a great deal of attention in the literature.^{17-23,52} The search for new Ni²⁺ laser materials has centered on doping into fluoride and oxide lattices, with the more recent emphasis being placed on the oxides.²⁰ A great deal of effort has been applied to gaining understanding of the processes involved in the non-radiative deactivation of the dopant ion from an excited state to its ground state.⁵³ The problem has proven to be quite formidable, however, and all models currently in use treat the problem in either an empirical or semi-empirical manner. Parameter values resulting from the application of these models⁵⁴ are often difficult to interpret physically and many studies do not attempt to analyze these values in terms of actual physical process within these materials. The problem is complicated further by the fact that different approaches to choosing input parameters for the non-radiative decay models can significantly affect the outcome of such calculations. The wide range of behaviour exhibited by transition metal ions serves to emphasize how difficult it is to formulate any general rules which will provide reliable estimates of parameters such as the luminescence decay rate for a new host material. This uncertainty has resulted in a broad survey or "trawling" approach to the search for new laser media, which is also followed in this investigation.

CHAPTER 2

GLASSES AND GLASS-CERAMICS

2.1 Introduction.

Although most of this report describes results obtained with crystalline media, we also investigated various amorphous materials (glasses/ceramics) doped with Co, Ni, and Cr ions. Glasses and ceramics appeared to offer the possibility of tailoring the luminescent properties of the material by variation of the composition and by suitable heat treatment. While this approach had not been successful with Cr ions, the reason for this failure is now well understood and it seemed that the possibility of obtaining efficient luminescence from amorphous materials doped with Co and Ni should be explored.⁵⁵ Thus, in the early stages of the project we initiated the preparation of various Co- and Ni-doped glasses and glass-ceramic materials and surveyed a range of different glass types for useful emission properties. While these early glass preparation efforts were somewhat "hit-or-miss", we hoped that the results of our broad initial surveys in both the glassy and crystalline media would provide sufficient guidance to enable us to suggest glass composition and fabrication procedures (thermal treatment, etc.) which would be likely to yield useful emissions and high luminescence efficiency. At that point, we planned to prepare and evaluate new doped glasses to provide continuous feedback for further trials. Our experiences in this area are summarised in this chapter.

2.2 Initial approach

A selection of glasses and ceramics were ordered from another institution (University of Limerick, Ireland) with expertise in glass fabrication techniques. This institution is technology-oriented and had an ongoing research programme devoted to the fabrication and testing of oxy-nitride glass-ceramics for engineering applications. The first batch of glasses and ceramics were doped with Co^{2+} , Ni^{2+} , and Cr^{3+} ; undoped control samples were also provided. They were cut into suitable sizes for optical absorption and laser-excited photoluminescence experiments and their spectroscopic behaviour was investigated.

Our approach was based on the experiences of Corning Glass Works (U.S.A.), where Cr^{3+} -doped silicate glass ceramics had been fabricated as potential luminescent solar concentrators.⁵⁶ In these materials, micro-crystals of the spinel (ZnAl_2O_4) are precipitated out of the mainly silica "mother" glass to form a glass-ceramic of high optical quality. At about the same time, efficient luminescence had been obtained from Ni-doped crystalline

materials with the spinel structure.²⁰ Guided by these results, we ordered also a range of glasses with ~60% silica and the remainder an equimolar mixture of Al_2O_3 and ZnO with other minor constituents to aid the glass-forming process. Nickel and cobalt doped versions of the glasses were obtained by diluting the ZnO content with small additions of either NiO or CoO . If a glass mixture, providing efficient IR emission, could be reproducibly fabricated it should have been possible to prepare the material in fibre form and develop a tunable fibre laser based on gas laser pumping or, in the ideal case, pumping by a diode laser. The broad absorption bands of the Co^{2+} and Ni^{2+} ions would allow matching with one of the many diode laser wavelengths currently available.

At this time also, we requested funding from the University Development Fund to purchase a furnace and associated utensils (platinum crucibles, moulds, etc) to enable us to have more control over the development of new materials and to speed up the process of fabrication and characterisation. The principal investigator also spent a week in the University of Utrecht (Holland) in May 1989 with the aim of (i) acquiring some expertise in glass fabrication, and (ii) obtaining information and guidance on the best choice of furnace and utensils for the purposes of our studies. He also visited the University of Lyon (France), which has an ongoing research programme on luminescent material fabrication and characterisation. The possibility of growing some glasses, and ceramics for our studies and the feasibility of purchasing glass samples from this source, were explored while in Lyon. We also had useful discussions on the most promising crystalline materials for our studies.

1.3 Initial results

Within the first year, a range of silicate, phosphate, and borate glasses as well as oxy-nitride glasses and ceramics were acquired from various sources. Initially, the difficulty of obtaining such samples prompted us to consider setting up glass fabrication facilities within the department. During visits to the University of Utrecht and the Philips Laboratories in Holland, several glasses were prepared and the techniques for glass fabrication were studied. However, the results were generally disappointing and only very weak luminescence was detected from these materials and even then not in all the samples. A range of oxy-nitride glass/ceramics doped with Ni^{2+} , Co^{2+} , and Cr^{3+} were obtained from the University of Limerick (Ireland). These materials were made from one of the following mixtures,⁵⁷

- (a) Y_2O_3 , Al_2O_3 , Si_3N_4 , AlN , SiO_2 , YN .
- (b) MgO , Al_2O_3 , Si_3N_4 , AlN , SiO_2 , Mg_3N_2

Depending on the composition and heat treatment, various crystalline phases may be

precipitated in the ceramic. In type (a) YAG is a common crystalline constituent while in type (b) the main crystallisation products are forsterite, MgSiO_3 , and MgAl_2O_4 (spinel). Four different samples were obtained for each dopant ion. Here the results were more encouraging as almost all the samples showed some luminescence in the $0.8 \rightarrow 1.8 \mu\text{m}$ spectral region. Some representative spectra are shown in Fig 2.1. A particularly strong band, centred at $\approx 1.55 \mu\text{m}$, was observed in all the materials - even in the nominally undoped samples of each batch. It does not occur in samples deliberately doped with Nd. At this point, plans to fabricate glasses in-house were postponed and it was decided to concentrate on glass-ceramics for the future as these seem to offer more likely hosts. We ordered a further set of such materials from the facility in the University of Limerick. These were based on silicate glass ceramics (from a melt containing Al_2O_3 , SiO_2 , and ZnO) in which the crystalline phase, doped with cobalt or nickel, was expected to have the gahnite spinel structure. This was suggested by the success achieved by GTE Labs⁵⁶ in obtaining high-quality Cr-doped ceramics for luminescent applications based on this mixture.

Although we have examined more than 30 different glass compositions, we have not observed any strong luminescence features in these materials that we could definitely ascribe to emission to the dopant TM ions. The strong emission band observed in many of the oxy-nitride glasses at $1.5 \mu\text{m}$ is not associated with the TMI dopant and may be due to contamination of the starting materials by rare earth elements.

Some fluoride glasses doped with Ni and Co ions were obtained from La Verre Fluore in Rennes (France) and these samples provided the best luminescence signals obtained to date from glasses. We are hoping to pursue this avenue and obtain long fluoride glass fibres doped with these ions and explore the possibility of obtaining amplification over the long path lengths involved. We suggest that any future investigations on glassy host materials should be confined to fluoride glasses.

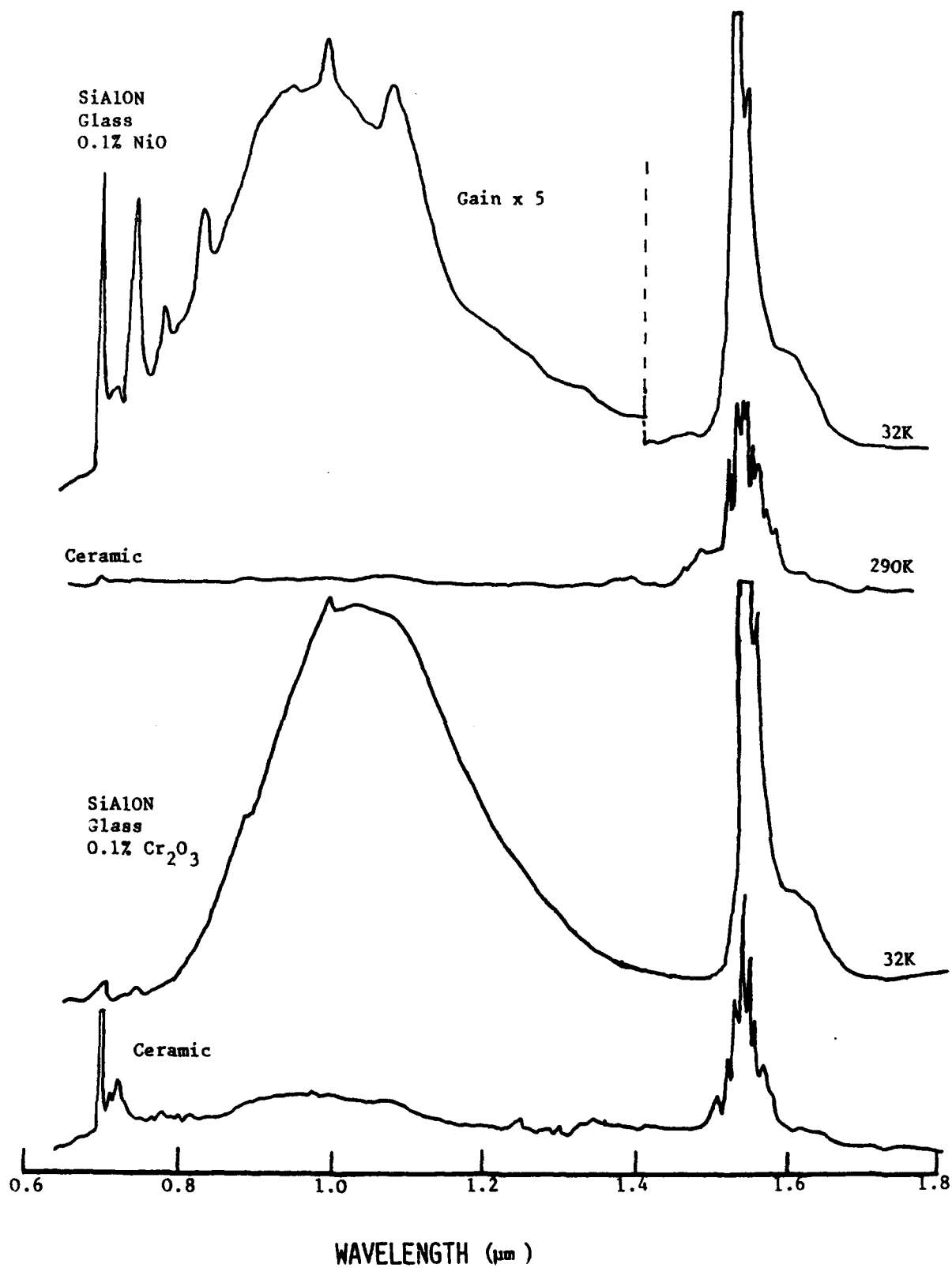


Fig. 2.1 Selected luminescence spectra of oxynitride glasses and ceramics.

CHAPTER 3

Co-DOPED MEDIA

3.1 Introduction

The stimulus for this project was the encouraging preliminary results^{52,58} obtained with LiGa_5O_8 doped with Ni^{2+} and Co^{2+} . Encouraged by the AFOSR support, we continued our investigation of the basic spectroscopy of these materials. Since our earlier studies, we acquired a sensitive Ge detector which allowed us to look at all the Co^{2+} emission bands with the same detector. (In our previous experiments, three different detector systems were used to record the various emission bands). The complete room temperature spectrum recorded with the Ge detector is shown in Fig 3.1. Although the emission is dominated by the highest energy band, this system is important and interesting in that it provides several broad transitions in the near IR which could be used to obtain tunable laser action in this region. Pumping with an argon ion laser in a configuration similar to that used for Ti:sapphire may be feasible. However, the quality of our materials, flux grown samples from the Bell Labs (1965), was poor - showing non-uniform blue coloration. Very beautiful samples obtained from Stanford University were found to be colored only on the surface. In the meantime, we investigated our own samples in more detail via FLN studies of the sharp zero-phonon line at 650 nm at low temperature. An unusually large ground state splitting of $\sim 30 \text{ cm}^{-1}$ was observed which we ascribed to the low symmetry at the Co^{2+} site and the small ${}^4\text{A}_2 - {}^4\text{T}_2$ separation, as well as significant inhomogeneous broadening which masked the splitting in the non-narrowed emission spectrum. The latter is probably due to lattice strain and charge compensation effects. This work was reported at the Dynamical Processes in Solids Conference (Atlanta, GA) and was published in *J. Luminescence*. (Appendix 1). A more detailed analysis of the spectroscopy of this material, including ODMR-MCD studies by co-workers in the University of Lehigh, was subsequently carried out in order to fully characterise this interesting material. A complete report, including a detailed theoretical analysis of the crystal field levels of the Co^{2+} ion in this material and identification of the nature of the impurity environment, was published recently in *Physical Review* (Appendix 2). Meanwhile, we searched for new Co-doped materials and our results are gathered in the following sections.

3.2 Optical spectroscopy of $\text{MgNb}_2\text{O}_6:\text{Co}^{2+}$

3.2.1 Crystal Structure of the Host Material : Magnesium Niobate has the same structure as the mineral columbite ($\text{Nb}_2(\text{Fe},\text{Mn})\text{O}_6$)⁵⁹. Columbite has a tetra-molecular orthorhombic cell of the dimensions $a_0=14.238\text{A}$, $b_0=5.730\text{A}$ and $c_0=5.082\text{A}$. It's space group is

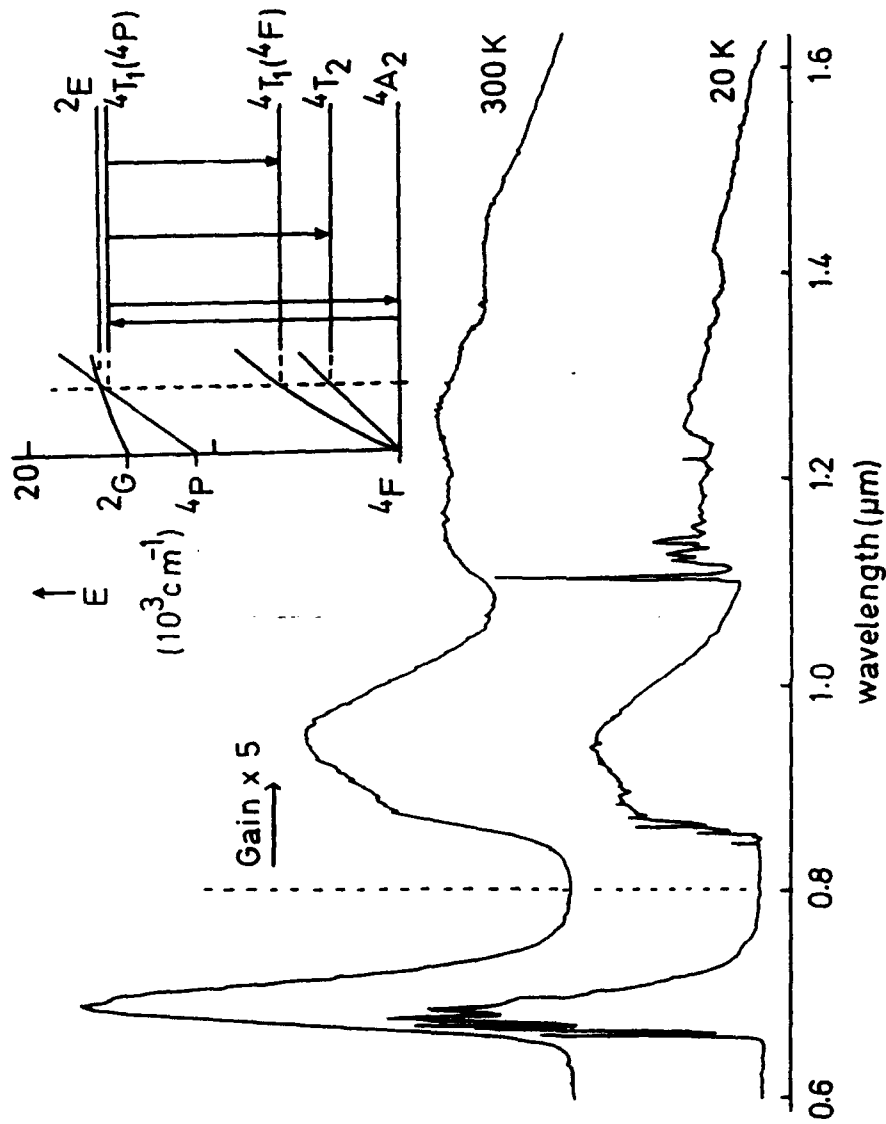


Fig. 3.1 The luminescence spectrum of $\text{LiGa}_3\text{O}_8:\text{Co}^{2+}$ recorded at 24 K and 290 K. The energy level structure for the Co^{2+} ion in an tetrahedral site in this material is also shown.

D_{2h}^{14} (Pbcn) with iron and manganese atoms occupying the positions ;

$$\pm(0, u, \frac{1}{4}) \quad \pm(\frac{1}{2}, u + \frac{1}{2}, \frac{1}{4}) \quad \text{where } u = 0.350.$$

All other atoms are in the general positions ;

$$\pm(x, y, z; x, y, z + \frac{1}{2}; \frac{1}{2} - x, \frac{1}{2} - y, z + \frac{1}{2}; \frac{1}{2} - x, y + \frac{1}{2}, z)$$

where the parameters x, y and z for these atoms are shown in table 3.1 below.

Table 3.1

Atom	x	y	z
Nb	0.163	0.175	0.750
O(1)	0.090	0.095	0.083
O(2)	0.410	0.100	0.083
O(3)	0.750	0.080	0.070

In this structure each metal atom is surrounded by a nearly regular octahedron of oxygen atoms which are approximately hexagonally closed-packed. The (Fe,Mn)-O octahedra are arranged in chains ranged along the a_0 axis and held together by sharing edges. In $MgNb_2O_6$, the Mg ions occupy the equivalent positions of the Fe and Mn ions in $Nb_2(Fe,Mn)O_6$. As the Mg^{2+} ions in $MgNb_2O_6$ have the same valency as Co^{2+} and remembering that niobium has a valency of +5, we can assume that the nickel substitutes as Ni^{2+} for Mg^{2+} in $MgNb_2O_6$. The colour of the $MgNb_2O_6:Co^{2+}$ crystals, pale blue, is unusual if the cobalt is substituted as Co^{2+} in octahedral as expected in this material. Normally, Co^{2+} ions in oxide hosts give rise to a red colour when octahedrally coordinated and a blue colour when tetrahedrally coordinated⁶⁰. The crystal structure in this case, however, only allows an octahedral site for the substitutional Co^{2+} ion. Note that although the Co^{2+} immediate environment is approximately an oxygen octahedron, the actual site symmetry is much lower - C_2 . The samples used in this study were of good optical quality but were not optically oriented.

3.2.2 Luminescence and Absorption Data

The only emission from $MgNb_2O_6:Co$ observed in this study was a broad band centered at about 950 nm. The low temperature (21 K) spectrum (uncorrected for the system response) excited by an Argon ion laser is shown in Fig. 3.2. It consists of a weak zero phonon line at 821.2 nm and a very strong sideband extending to $\sim 1.2 \mu m$. Apart from the zero phonon line, some structure is evident on the high energy side of the emission band. The luminescence spectra are shown at intermediate temperatures between 21 K and room temperature are also shown in Fig. 3.2. At 21 K the peak of the sideband occurs at 925 nm and at room temperature the peak has shifted to 975 nm. The sideband broadens

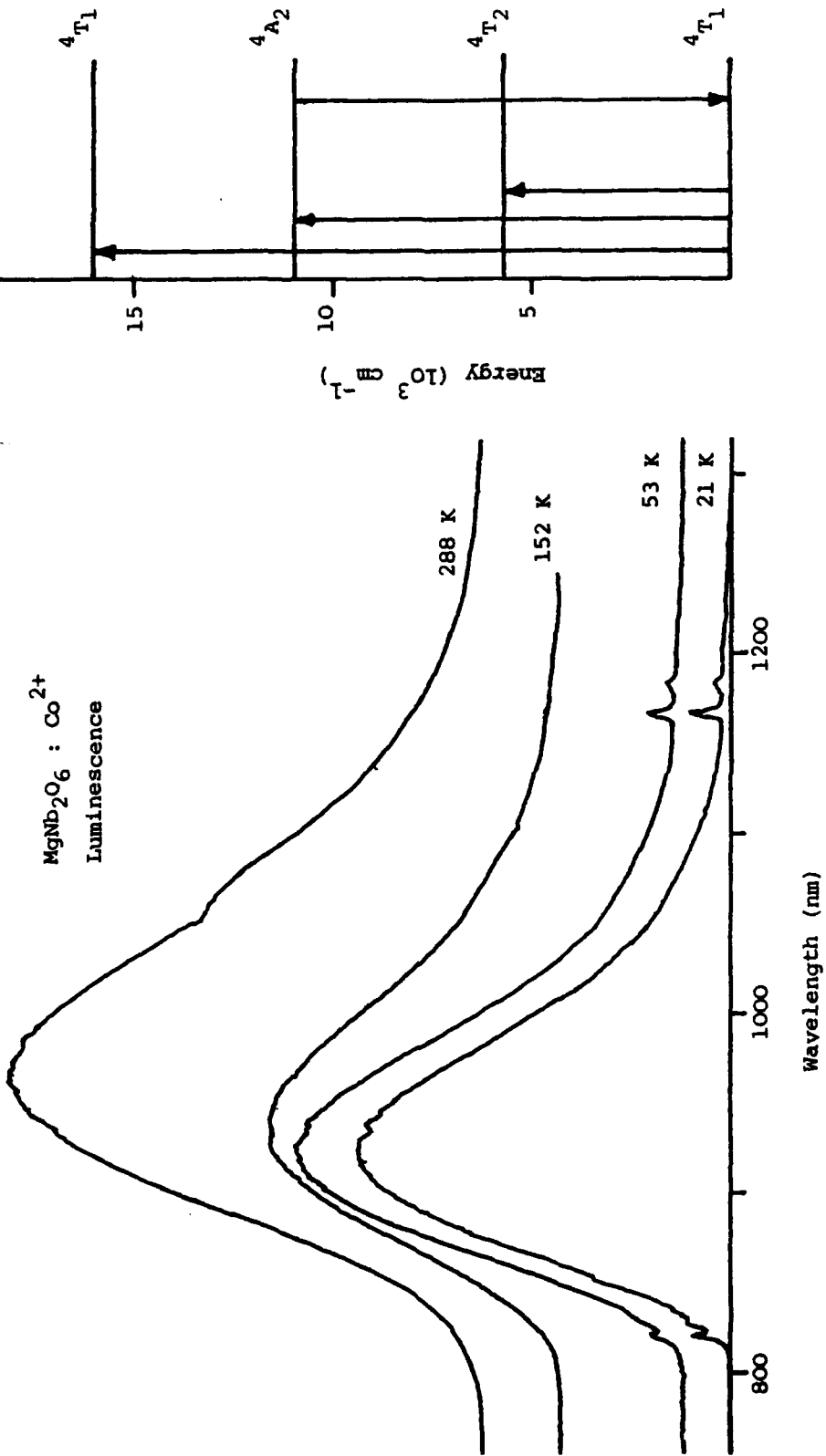


Fig. 3.2 Luminescence spectra of MgNb₂O₆:Co²⁺ recorded at various temperatures. The energy level diagram on the right was derived from absorption and luminescence data.

considerably and extends beyond $1.3 \mu\text{m}$ at room temperature. The integrated intensity of the emission as a function of temperature is shown in Fig. 3.3. As can be seen from the figure, the intensity remains relatively constant up to 160 K and then falls off rapidly. This fall off in intensity is attributed to an increase in the non-radiative decay rate at higher temperatures.

The absorption spectrum for $\text{MgNb}_2\text{O}_6:\text{Co}$ at 85 K is shown in Fig. 3.4. The spectrum is very similar to that observed for Co^{2+} in octahedral sites in other oxide hosts^{35,60} and based on the assignments in these references, we assign the 6500 cm^{-1} and 13500 cm^{-1} absorption bands of $\text{MgNb}_2\text{O}_6:\text{Co}$ to the ${}^4\text{T}_1(4\text{F}) \rightarrow {}^4\text{T}_2(4\text{F})$ and ${}^4\text{T}_1(4\text{F}) \rightarrow {}^4\text{T}_2(4\text{F})$ transitions, respectively, of octahedrally coordinated Co^{2+} . We attribute the 18000 cm^{-1} absorption to the ${}^4\text{T}_1(4\text{F}) \rightarrow {}^4\text{T}_1(4\text{P})$ transition. By solving the secular determinants for the lowest crystal field levels of this system, we obtain expressions⁴⁸ for these level energies in terms of the crystal field parameter Dq and Racah parameter B . A best fit to these energies is obtained for the following values : $Dq = 727 \text{ cm}^{-1}$ and $B = 800 \text{ cm}^{-1}$; $Dq/B = 0.9$ (see Fig. 2.3)

In most Co^{2+} doped materials luminescence occurs from the first excited state ${}^4\text{T}_2(4\text{F})$ to the ${}^4\text{A}_2(4\text{F})$ ground state only^{33-37,60}. Thus in $\text{MgNb}_2\text{O}_6:\text{Co}^{2+}$ we would expect the ${}^4\text{T}_2(4\text{F}) \rightarrow {}^4\text{T}_1(4\text{F})$ emission to occur around $1.8 \mu\text{m}$ (6500 cm^{-1}). We were unable to investigate this region of the spectrum with the detectors available. We assign the observed emission at $\sim 1 \mu\text{m}$ to the ${}^4\text{A}_2(4\text{F}) \rightarrow {}^4\text{T}_1(4\text{F})$ transition. The resulting energy level scheme showing both absorption and luminescence transitions is shown as an inset in Fig. 3.2.

3.2.3 Lifetime Measurements and Discussion.

The decay time of the observed infra-red luminescence band was measured as a function of temperature between 30 K and 320 K. At low temperature (31 K) the decay time was found to be $4.48 \mu\text{s}$. This very short decay time is consistent with our assignment of the luminescence to the spin-allowed ${}^4\text{A}_2 \rightarrow {}^4\text{T}_1$ transition. As the Co^{2+} ion site lacks inversion symmetry, the transition is also parity-allowed. Fig. 3.3 shows how the observed decay time varies as the temperature is increased. The decay time remains almost constant up to 200 K, and then decreases rapidly. Since the temperature dependencies of the integrated intensity and of the decay time are very similar, we attribute the fall off in the observed decay time with increasing temperature to the growth of non-radiative decay processes. The observed decay rate W is given by $W = W_r + W_{nr}$, where W_r is the radiative decay rate and W_{nr} the non-radiative decay rate. We assume that the contribution from vibronic processes to the emission is negligible so that W_r is independent of temperature. For the analysis which follows we also assume the energy level positions do not vary with temperature.

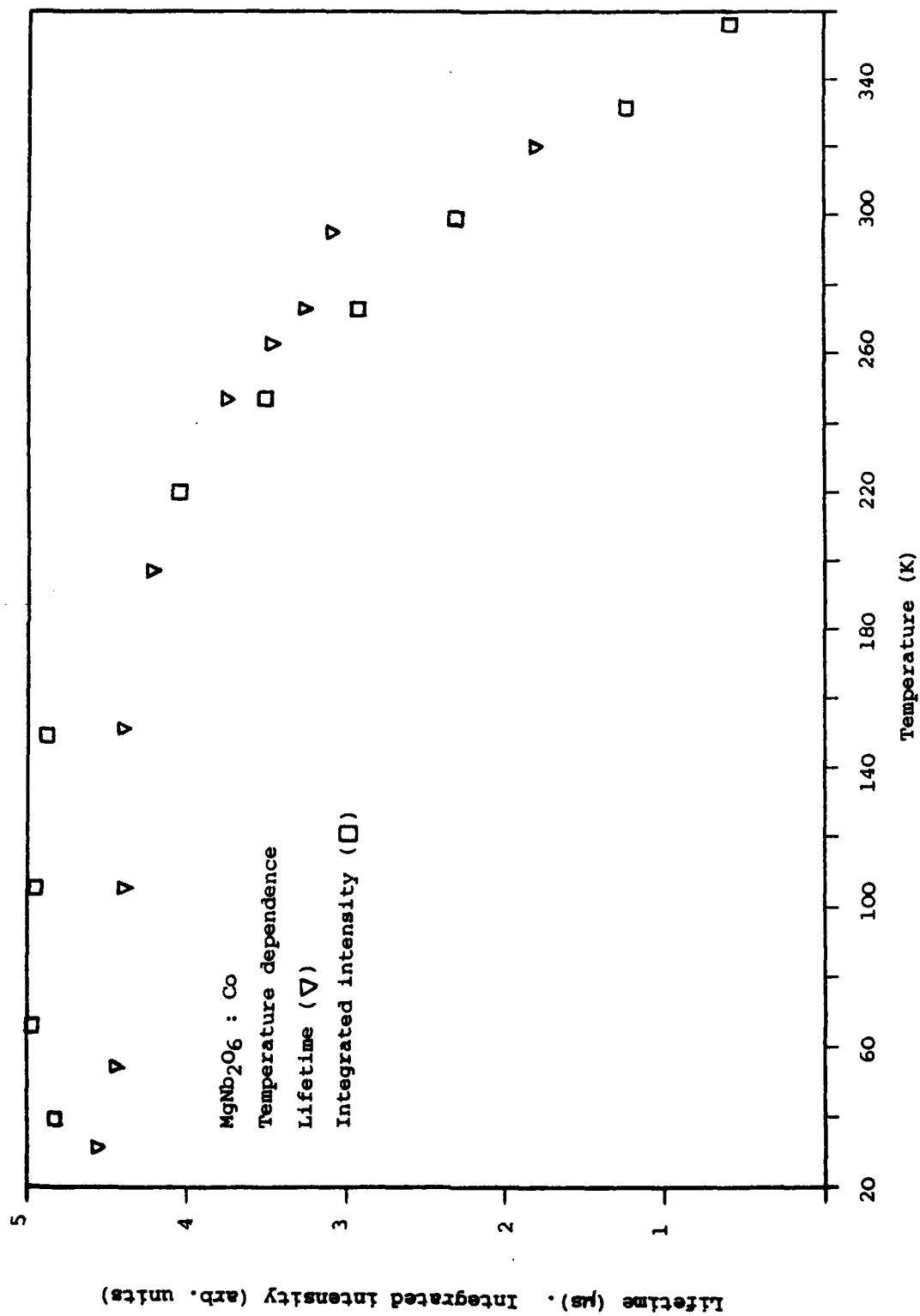


Fig. 3.3 Temperature dependence of the lifetime and total intensity of the emission from $\text{MgNb}_2\text{O}_6:\text{Co}^{2+}$.

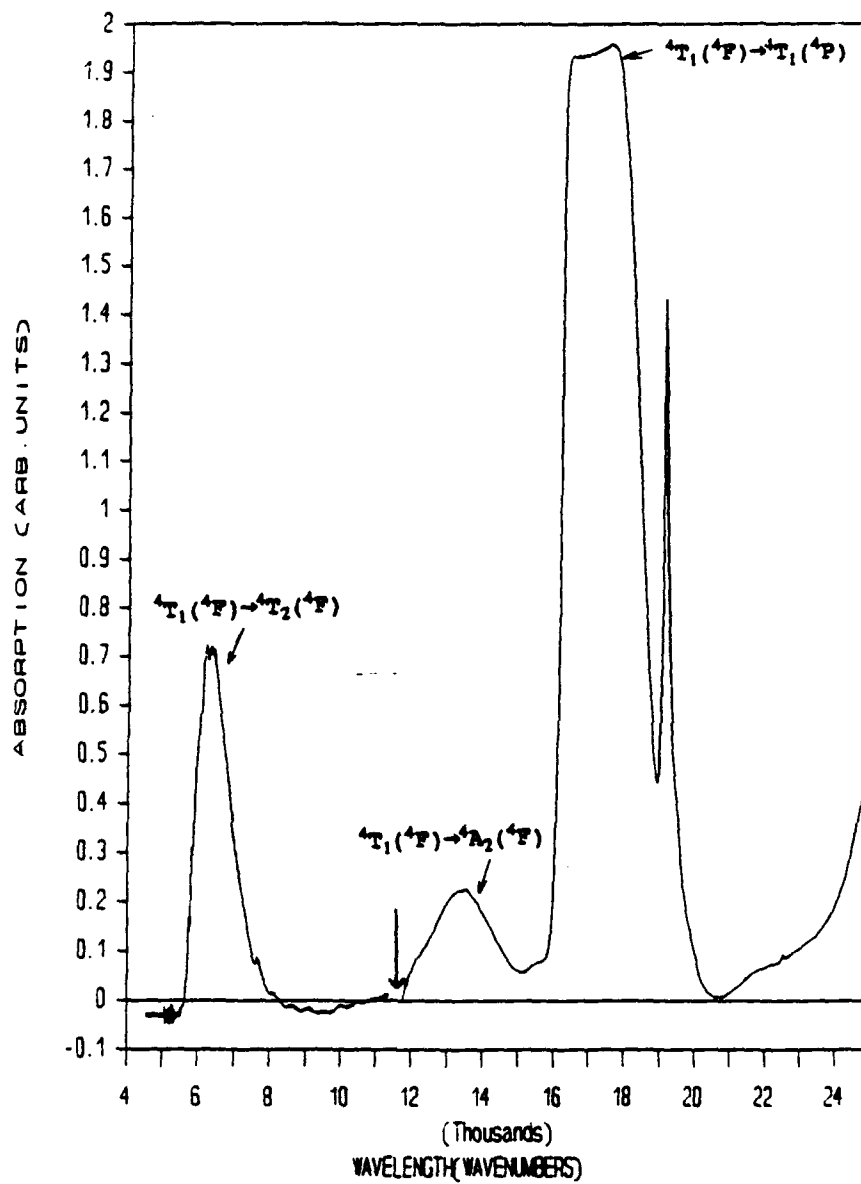


Fig. 3.4 The absorption spectrum for MgNb₂O₆:Co at 85K. The arrow indicates a discontinuity which results from a change of detector.

From a quantum mechanical analysis, the non-radiative decay rate W_{nr} is given by⁴⁸

$$W_{nr} = \frac{1}{T_{nr}} = \frac{R^2 \exp(-S(1+2m)) S^P}{P!} \sum_{l=0}^{\infty} \frac{P!}{l!(l+P)!} (1+m)^{l+P} (mS^2)^l \quad (3.1)$$

where R is an electronic matrix element, $P = \Delta E/\hbar\omega$ where ΔE is the energy gap between the two levels, and $\hbar\omega$ is the effective phonon energy. S is the Huang-Rhys factor and m the mean thermal occupancy in the vibrational mode where;

$$m = \frac{1}{\exp(\hbar\omega/kT) - 1} \quad (3.2)$$

The non-radiative decay rate W_{nr} as a function of temperature, normalised to its value at 320K, is shown in Fig. 3.5. Theoretical plots of equation 3.1 for $S = 3$ and different sets of P and $\hbar\omega$ where $P\hbar\omega = \Delta E = 7183 \text{ cm}^{-1}$ are also shown (full lines). Best fit occurs for $P = 21$ and $\hbar\omega = 340 \text{ cm}^{-1}$, which suggests that the dominant phonon energy is 340 cm^{-1} . It is found that the expression for the non-radiative rate (eqn. 3.1) is not as sensitive to variations in S as to variations in P and $\hbar\omega$. Although we cannot deduce an accurate value for S from the lifetime data, we can estimate this parameter from the absorption and luminescence data. For the ${}^4A_2 \rightarrow {}^4T_1$ emission, the energy difference between the zero-phonon line and the peak of the sideband is given by,⁴⁸

$$(S - 1/2) \hbar\omega = 1366 \text{ cm}^{-1} \quad (3.3)$$

For different values of S and $\hbar\omega$ which satisfy the above equation, theoretical models⁴⁸ of the emission were constructed and compared with the actual emission. The dependence of the emission band intensity on the number of phonons m (energy $\hbar\omega$) is given by

$$I(E) = I_0 \frac{S \exp(-S) S^m}{m!} \delta(E_0 + m\hbar\omega - E) \quad (3.4)$$

where E_0 is the energy of the electronic origin. Best fit (Fig. 3.6) occurred for $S = 4.5$ and $\hbar\omega = 342 \text{ cm}^{-1}$. Therefore $S = 4.5$ was taken as the Huang-Rhys factor for the ${}^4A_2 \rightarrow {}^4T_1$ transition and $\hbar\omega = 342 \text{ cm}^{-1}$ as the effective phonon energy involved in the nonradiative process.

It is interesting that, in this material, the rapid nonradiative relaxation from 4A_2 to 4T_2 , which normally occurs in other Co^{2+} -doped materials, is not as efficient. Additional luminescence from this system in the transition ${}^4A_2 \rightarrow {}^4T_2$ (as well as the usual laser transition ${}^4T_2 \rightarrow {}^4T_1$) is expected beyond the range of our present detector but we hope to explore this region with new detection facilities in the near future.

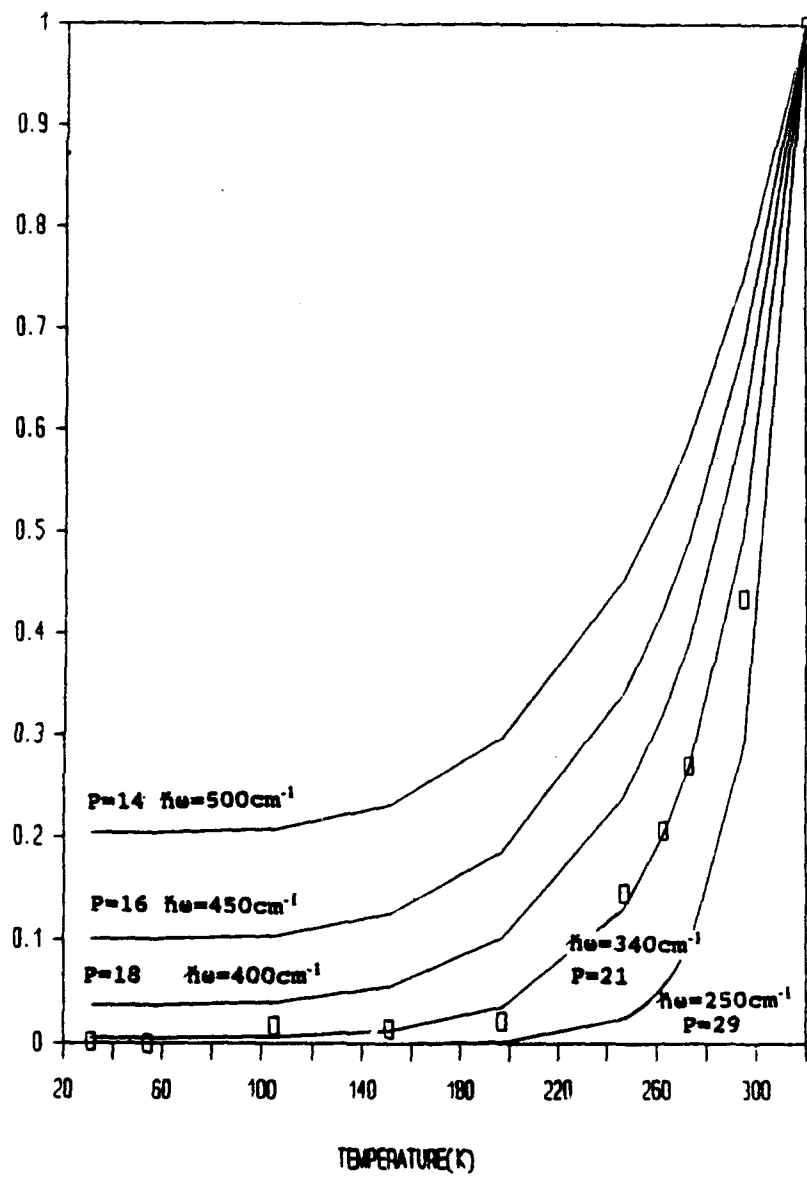


Fig. 3.5. The non-radiative rate (normalised at 320 K) as a function of temperature for $\text{MgNb}_2\text{O}_6:\text{Co}^{2+}$. The full lines are the theoretical plots of eqn. 3.1, for $S = 3$ and for different values of P and $\hbar\omega$

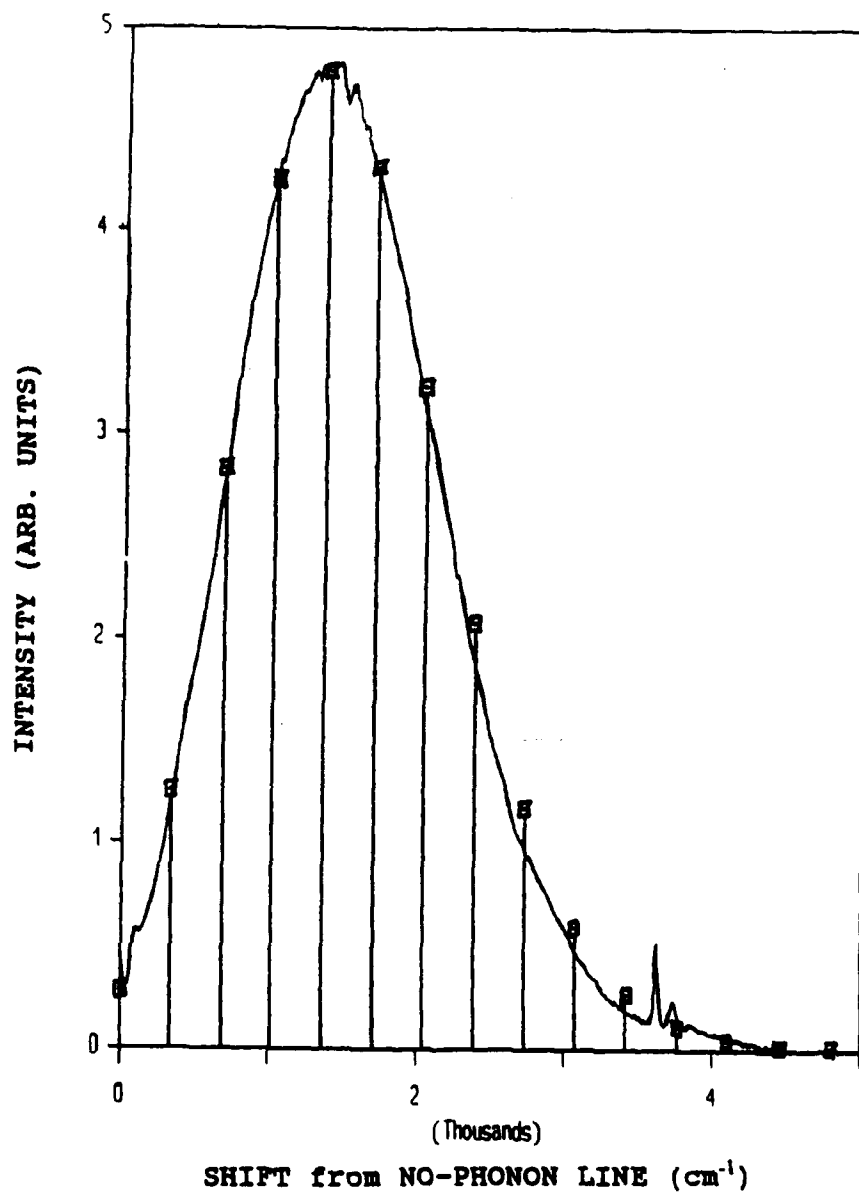


Fig. 3.6. Best fit between the observed emission and eqtn. 3.4 occurred for $\hbar\omega = 342 \text{ cm}^{-1}$ and $S = 4.5$. Individual points indicate a plot of eqtn. 3.4 for discrete values of m .

3.3 Luminescence from tetrahedral Co^{2+} ion in MgAl_2O_4

Our previous studies of the luminescence properties of tetrahedrally coordinated $\text{Co}^{2+}(\text{d}^7)$ ion in LiGa_5O_8 was one of the reasons for embarking on this project and we searched for other materials in which the Co^{2+} ion occupied a tetrahedral site. A similar luminescence pattern was found in $\text{MgAl}_2\text{O}_4:\text{Co}^{2+}$. Absorption bands in this material at 7200, 17000 and 21000 cm^{-1} are assigned to transitions from the ${}^4\text{A}_2$ (${}^4\text{F}$) ground state to the ${}^4\text{T}_1$ (${}^4\text{F}$), ${}^4\text{T}_1$ (${}^4\text{P}$) and ${}^2\text{T}_1$ (${}^2\text{P}$) excited states of tetrahedrally coordinated Co^{2+} , respectively. The crystal field parameters $\text{Dq}=400 \text{ cm}^{-1}$, $\text{B}=730 \text{ cm}^{-1}$ and $\text{C}=3500 \text{ cm}^{-1}$ are estimated for a Co^{2+} ion a site of pure T_d symmetry. Saturation of Co^{2+} absorption at 540 nm was measured and the peak absorption cross section for the ${}^4\text{A}_2$ (${}^4\text{F}$) \rightarrow ${}^4\text{T}_1$ (${}^4\text{P}$) transition was estimated to be $4 \times 10^{-19} \text{ cm}^2$. The broad luminescence bands observed in the visible at 660 nm and in the near infrared at 880 nm and 1290 nm are assigned to transitions from the ${}^4\text{T}_1$ (${}^4\text{P}$) excited level to the lower lying ${}^4\text{A}_2$ (${}^4\text{F}$), ${}^4\text{T}_2$ (${}^4\text{F}$) and ${}^4\text{T}_1$ (${}^4\text{F}$) levels, respectively. The low-temperature spectrum is shown in Fig. 3.7. In contrast to LiGa_5O_8 , however, the luminescence intensity falls rapidly with increasing temperature and, at room temperature, the luminescence quantum yield was estimated to be less than 1%. The luminescence decay was shown to be non-exponential and dependent on the temperature and the concentration of Co^{2+} ions, providing evidence that luminescence quenching is due to both intra-ionic nonradiative decay processes and energy transfer. No spectroscopic evidence for octahedrally coordinated Co^{2+} has been observed. This work will be reported at the International Conference on Luminescence (Storrs, Ct., USA) 1993.

3.4 $\text{LiGaO}_2:\text{Co}^{2+}$

LiGaO_2 can crystallise in two stable phases. In the α -phase, the Co^{2+} ions, substituting for Ga^{3+} ions, are octahedrally coordinated; in the β -phase, the Co coordination is tetrahedral. High quality samples of this material were obtained from the University of Georgia. It is not possible to distinguish the crystal phase on the basis of the optical absorption spectrum, shown in Fig. 3.8, although it is very similar to that observed in LiGa_5O_8 , in which the Co^{2+} site is tetrahedral. However, the luminescence does not fit in with this assignment. It is possible that some cobalt enters as Co^{3+} or that some small regions of α -phase are present, which would allow octahedrally-coordinated Co^{2+} . Very weak emission is observed at low temperature (Fig. 3.8) but we hope to explore beyond 1.8 μm in this material also. With the new detection facilities, we plan to re-examine other Co^{2+} -doped materials which we studied in our preliminary survey in year 1.

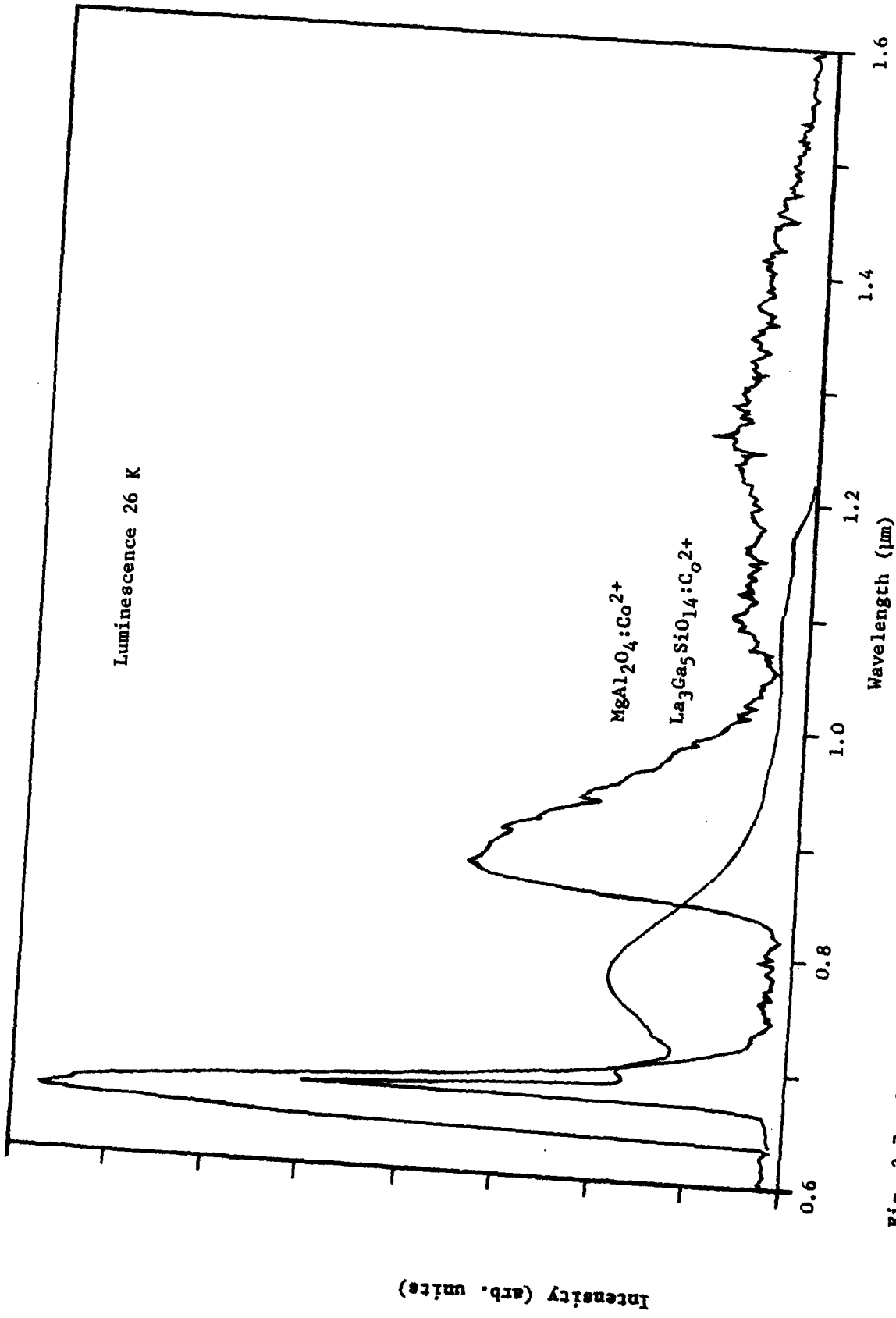


Fig. 3.7. Low temperature luminescence spectra excited by an Argon Laser.

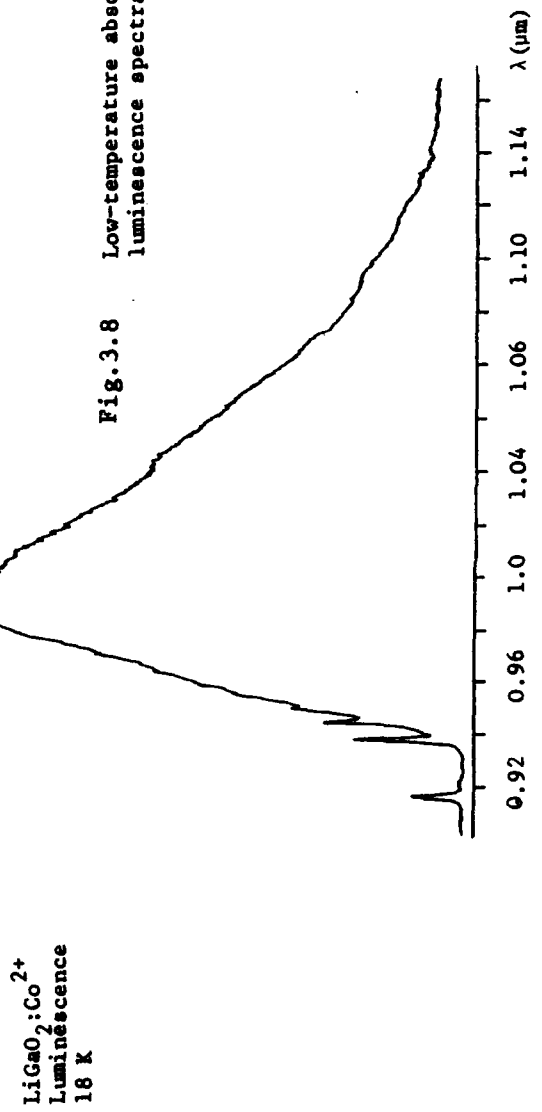
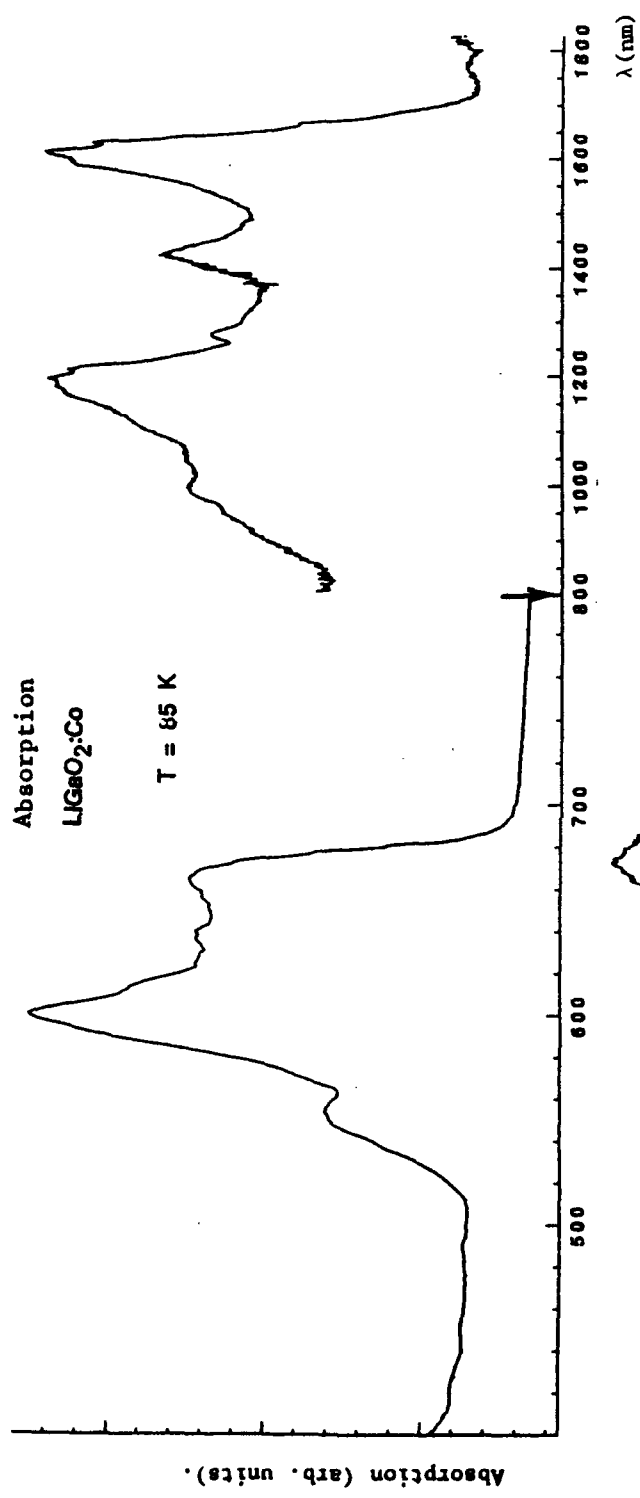


Fig.3.8 Low-temperature absorption and luminescence spectra of LiGaO₂:Co²⁺

3.5 Luminescence spectra of $\text{La}_3\text{Ga}_5\text{SiO}_{14}:\text{Co}^{2+}$

These samples, yellow in colour, were obtained from A. Kaminskii (Academy of Sciences, Moscow). Laser action has been obtained in a broad band around $1\ \mu\text{m}$ in the Cr^{3+} version of this material. The low-temperature luminescence spectrum of the Co^{2+} -doped system is shown in Fig. 3.7. It consists of at least two bands which resemble the higher energy bands in LiGa_5O_8 and MgAl_2O_4 (Figs. 3.1, 3.7). The lifetime of this luminescence is $\sim 2.1\ \mu\text{s}$, which suggests that the Co^{2+} occupies a tetrahedral site.

3.6. Conclusion.

Although the $\text{MgF}_2:\text{Co}^{2+}$ laser is the only commercial laser system based on Co or Ni ions, attempts to repeat this success in other media have not been successful. As in the case of Ni_2 doping, excited state absorption processes and nonradiative relaxation mechanisms are the main obstacles to laser action at room temperature. Operation at longer wavelengths, however, may be possible if efficient luminescence from the excited state occurs (as in MgNb_2O_6) or if luminescence from the ${}^4\text{T}_1({}^4\text{P})$ state can be obtained without thermal quenching (as in LiGa_5O_8). The importance of ESA in these materials at room temperature has yet to be carefully evaluated.

CHAPTER 4

Ni-DOPED MEDIA

4.1 Introduction

The spectroscopy of the Ni ion incorporated as an impurity in various host materials has been well studied.^{16-19,51} Investigations of Ni^{2+} in MgO , MgF_2 , KMgF_3 ,⁵¹ and in fluoro-zirconate glass⁵⁵ show that luminescence in the visible (green and red) and infrared is observed from the Ni^{2+} ions in these materials. Referring to the schematic energy-level diagram shown in Fig. 4.1, which is typical of the Ni^{2+} ion in oxide and fluoride crystals, the strongest absorption transitions in the Ni ion are ${}^3A_2 \rightarrow {}^3T_1({}^3P)$ (blue), ${}^3A_2 \rightarrow {}^3T_1({}^3F)$ (red) and ${}^3A_2 \rightarrow {}^3T_2$ in the near infrared. The visible emission originates in transitions from 1T_2 to two lower levels (3T_2 , 3A_2) and the infrared emission is from the lowest excited state (3T_2) to the ground state 3A_2 . In all these materials the fluorescence lifetime and quantum efficiency fall off rapidly with increasing temperature due an increase in the non-radiative multi-phonon relaxation rate, which competes with the radiative decay process.

In more recent work on various chloride hosts²⁹, additional transitions from 1T_2 to the lower levels 1E and 3T_1 have been reported. It is possible that these transitions also take place in many oxides but have not been reported because, in the oxides, they can occur in about the same wavelength regions as the main transitions mentioned above. The relative weakness of the ${}^1E_g \leftarrow {}^1T_{2g}$ transition compared to the ${}^3T_{2g} \leftarrow {}^1T_{2g}$ and ${}^3T_{1g} \leftarrow {}^1T_{2g}$ transitions is quite puzzling, since it seems to defy the spin selection rule. In absorption, the three "spin-forbidden" transitions, ${}^3A_{2g}$, ${}^3T_{2g}$, ${}^3T_{2g}$, are of approximately equal dipole strengths, while the "spin-allowed" ${}^1E_g \leftarrow {}^1T_{2g}$ transition is considerably weaker. The same basic analysis applies for the $\text{Ni}^{2+}:\text{CsMgCl}_3$ emission spectrum (although here the ${}^1E_g \leftarrow {}^1T_{2g}$ transition is somewhat stronger than in $\text{Ni}^{2+}:\text{CsCdCl}_3$), and, in the emission spectra of $\text{Ni}^{2+}:\text{CdCl}_2$ and $\text{Ni}^{2+}:\text{MgCl}_2$, and ${}^1E_g \leftarrow {}^1T_{2g}$ emission cannot be distinguished at all.²⁹ Although it is almost certain that both the ${}^1T_{2g}$ and the 1E_g states have considerable mixed spin character (both are close to triplet states) it is difficult to rationalize the apparent reversal of spin selection rules solely on this basis. Absorption transitions in this system, for example, adhere quite well to the spin selection rule, with spin-forbidden transitions being approximately an order of magnitude weaker than those which are spin-allowed. In this chapter, we present results on two Ni-doped oxides in which the crystal field is closer to that which occurs in fluorides and chlorides and in which additional transitions from 1T_2 are also observed.

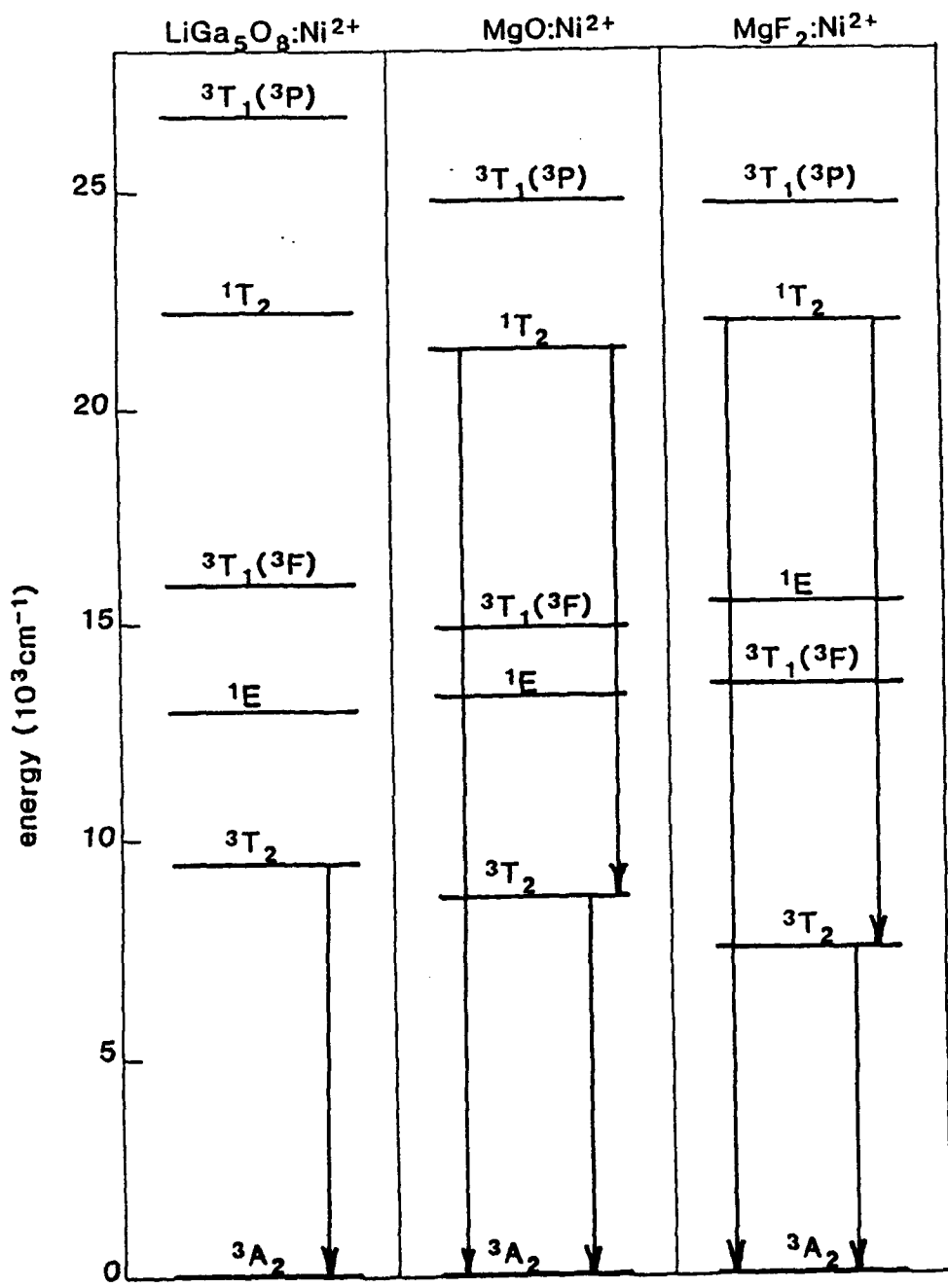


Fig. 4.1. Energy-level diagrams for Ni^{2+} in (a) LiGa_5O_8 , (b) MgO , and (c) MgF_2 . The luminescence transitions are shown by vertical lines.

In contrast to this trend, there is only one luminescence transition in Ni^{2+} -doped LiGa_5O_8 , a spinel-type crystal in which Ni^{2+} replaces Ga^{3+} on octahedral sites.⁵² This is the ${}^3\text{T}_2 \rightarrow {}^3\text{A}_2$ transition indicated in Fig. 4.1, which consists of a broad band centered at $1.3 \mu\text{m}$. Furthermore, the lifetime of the Ni^{2+} luminescence remains effectively constant from 15 K to above room temperature, with a decay time of $650 \mu\text{s}$. As the temperature is raised above about 350 K, we observe a decrease in the intensity and a corresponding decrease in lifetime. The theoretical formula for the non-radiative decay rate, based on the single configurational coordinate model, provides a quantitatively correct explanation for the temperature variation of the lifetime⁵² and is strong evidence for a high luminescence quantum efficiency. This material is interesting in that (i) all the emission occurs in the near infrared, and (ii) the emission has a high quantum efficiency at room temperature. Our samples were flux-grown, showed non-uniform green coloration, and were of poor optical quality. With good quality samples, we felt that tunable laser operation in the region of $1.3 \mu\text{m}$ should be possible. Using the laser-heated-pedestal growth technique, better quality samples of this material have been grown and unsuccessful attempts were made to obtain laser action in this system, using a diode laser operating at 904 nm. We subsequently requested better quality flux-grown samples of this material, but it is quite difficult to grow. However, the material LiAl_5O_8 doped with Ni^{2+} is much easier to grow. Samples of this material have been obtained recently and preliminary measurements show that it also has only one luminescence band. Similar behaviour was found in $\text{ZnAl}_2\text{O}_4:\text{Ni}^{2+}$. These results will be presented in later sections of this chapter.

4. 2 The Optical Spectroscopy of $\text{MgNb}_2\text{O}_6:\text{Ni}$.

The crystals of $\text{MgNb}_2\text{O}_6:\text{Ni}$ obtained for the present study were grown by the flame fusion (Verneuil) method. They were straw coloured and of poor optical quality. The particular sample used for most measurements had one polished front surface and was not oriented. An additional face, through which the excitation beam entered, was cut and polished perpendicular to the existing polished surface. The sample measured approximately $1.5\text{mm} \times 1.5\text{mm} \times 0.5\text{mm}$. The crystal structure has been described in chapter 3.

The infra red luminescence spectrum for $\text{MgNb}_2\text{O}_6:\text{Ni}$ at 22K is shown in Fig.4.2. This spectrum is corrected for the response of the Ge detector and spectrometer. It consists of three main bands at 900 nm, $1.2 \mu\text{m}$ and $1.7 \mu\text{m}$. Fig.4.3 shows all three bands in more detail. The 900 nm band in this figure was taken using an S-1 photomultiplier. It consists of a zero-phonon line at 7704 Å (12981 cm^{-1}) with a sideband extending to $1.1 \mu\text{m}$. The higher energy side of the sideband shows some structure. The $1.2\mu\text{m}$ band consists of a no-phonon line at 11688 Å (8556 cm^{-1}) with a well structured sideband extending to $1.27\mu\text{m}$. The $1.7\mu\text{m}$ emission is the most intense of the infra red bands. The zero-phonon line is at

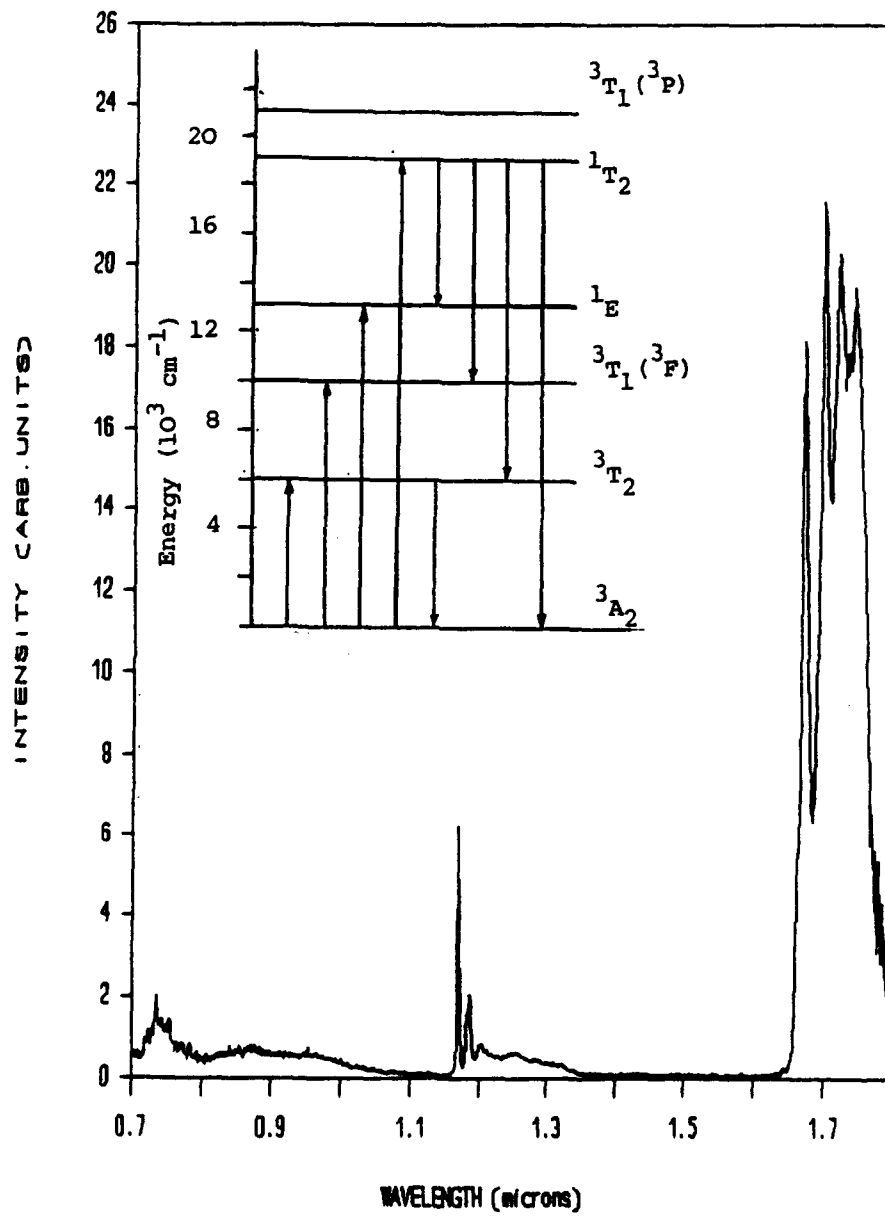


Fig. 4.2. The infrared luminescence bands of $\text{MgNb}_2\text{O}_6:\text{Ni}^{2+}$. The energy level diagram shown in the inset was derived from the absorption and luminescence data.

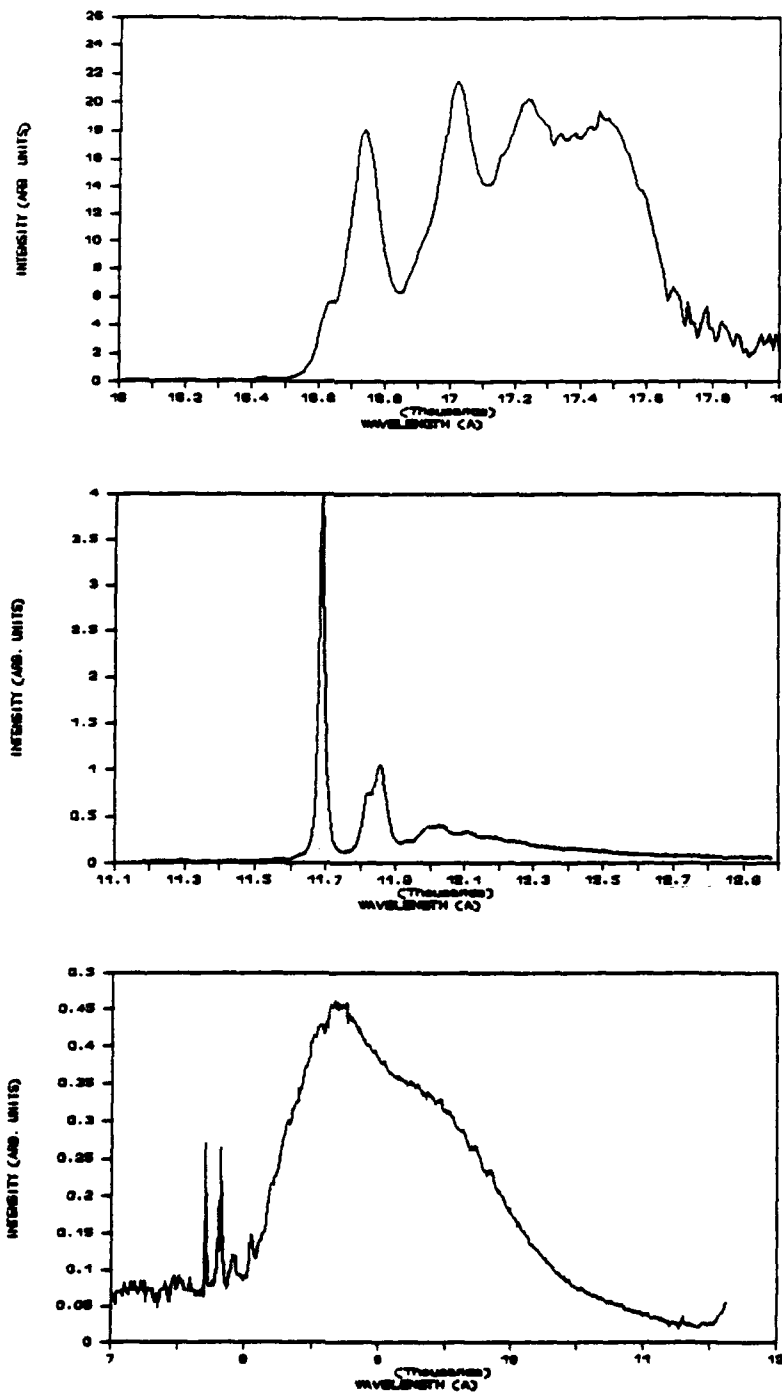


Fig. 4.3. The near infra-red emission bands of MgNb₂O₇:Ni at 22K in more detail.

16617A (6018 cm^{-1}) and the sideband extending beyond the long wavelength limit of the detector response ($\sim 1.78 \mu\text{m}$) shows considerable structure. Note that because the response of the spectrometer and Ge detector is falling off rapidly beyond $1.75 \mu\text{m}$, the exact shape of the high wavelength side of this band is uncertain.

Figure 4.4 shows the temperature dependence of the infra-red emission up to room temperature, taken using the Ge detector. These spectra are also corrected for the response of the Ge detector and the 0.5m SPEX spectrometer. Note the appearance of an extra line on the low energy side of the $1.2 \mu\text{m}$ band at 54 K. This extra line is most pronounced between 105 K and 153 K and is presumably due to the population of a higher excited state in the upper level of this transition. As the temperature is increased from 21 K to room temperature, all the bands broaden considerably. At room temperature the 900 nm and $1.2 \mu\text{m}$ emissions form one continuous band. Also at room temperature the higher energy side of the $1.7 \mu\text{m}$ emission extends to $1.45 \mu\text{m}$. The intensity in the lowest energy band decreases by a factor of ~ 10 between 26 K and room temperature.

The visible luminescence at 26 K and room temperature is shown in Fig. 4.5. The low temperature spectrum consists of a no-phonon line at 5272 Å (18968 cm^{-1}) and a very strong sideband extending to 6000 Å, displaying structure on the high energy side. At room temperature the overall visible emission becomes much broader and the appearance of an anti-Stokes band on the high energy side is evident.

4.2.1 Absorption Measurements on $\text{MgNb}_2\text{O}_6:\text{Ni}$.

The absorption spectrum taken using a cold finger cryostat (85K) is shown in Fig. 4.6. In MgO^{51} , Ni substitutes for Mg^{2+} ions in sites having octahedral symmetry only. The similarity between the absorption spectra of $\text{MgO}:\text{Ni}^{2+}$ and $\text{MgNb}_2\text{O}_6:\text{Ni}$ provides further evidence that Ni in MgNb_2O_6 is present in octahedral sites as Ni^{2+} . By comparison then, the strong energy peak at 460 nm can be attributed to the ${}^3\text{A}_2({}^3\text{F}) \rightarrow {}^3\text{T}_1({}^3\text{P})$ transition of Ni^{2+} in a octahedral site, while the band peaking at 840 nm is attributed to the ${}^3\text{A}_2({}^3\text{F}) \rightarrow {}^3\text{T}_1({}^3\text{F})$ transition. The weak shoulder band located around 510 nm is characteristic of the spin forbidden ${}^3\text{A}_2({}^3\text{F}) \rightarrow {}^1\text{T}_2({}^1\text{D})$ transition. While a similar feature does not occur in the $\text{MgO}:\text{Ni}^{2+}$ absorption, we believe that the sharp peak at 720 nm is due to the ${}^3\text{A}_2({}^3\text{F}) \rightarrow {}^1\text{E}({}^1\text{D})$ transition. We attribute the green emission, the 900 nm emission and the $1.2 \mu\text{m}$ emission to the ${}^1\text{T}_2 \rightarrow {}^3\text{A}_2$, ${}^1\text{T}_2 \rightarrow {}^3\text{T}_2$ and ${}^1\text{T}_2 \rightarrow {}^3\text{T}_1$ transitions respectively. The resulting energy level scheme showing both absorption and luminescence transitions is shown in the inset in Fig. 4.2. The energy of the $1.7 \mu\text{m}$ band is consistent with its assignment to either a ${}^1\text{T}_2 \rightarrow {}^1\text{E}$ or ${}^3\text{T}_2 \rightarrow {}^3\text{A}_2$ transition.

The parameters Dq, B and C can be found by solving the secular equations obtained from the Sugano-Tanabe matrices for the different levels and fitting the resulting expressions (involving Dq, B, C) to the measured transition energies in absorption. Best net agreement

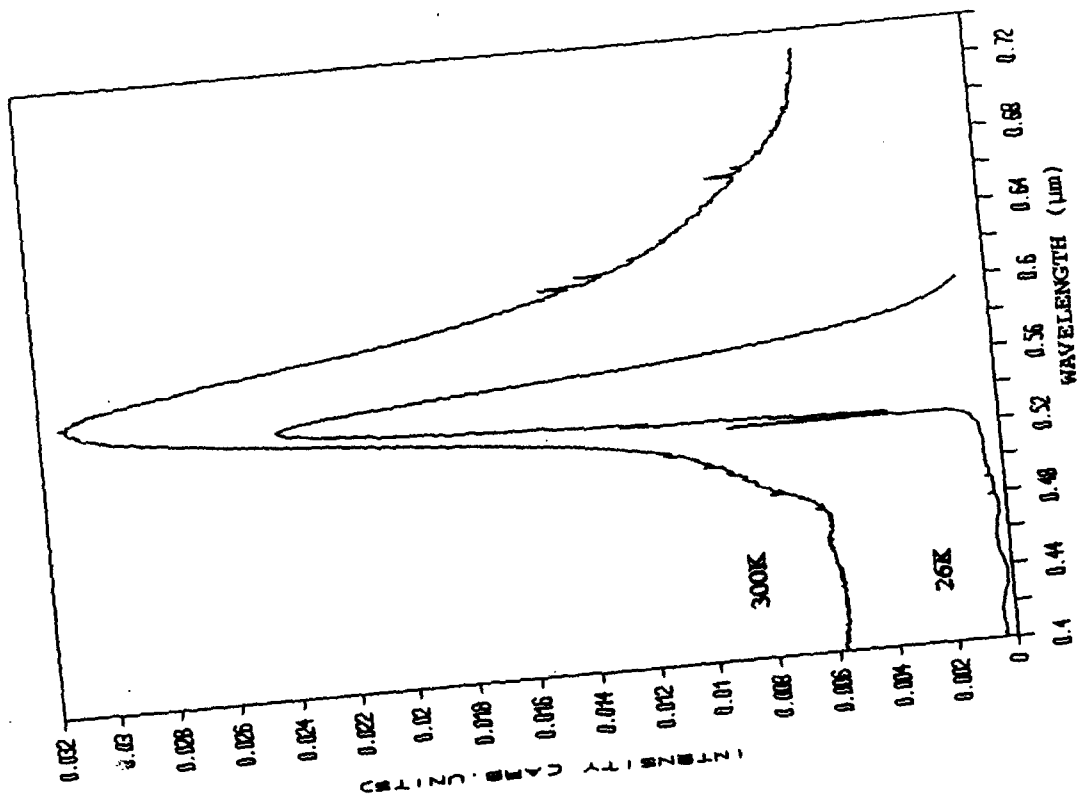


Fig. 4.5. Visible emission at 26K and room temperature from MgNb₂O₆:Ni.

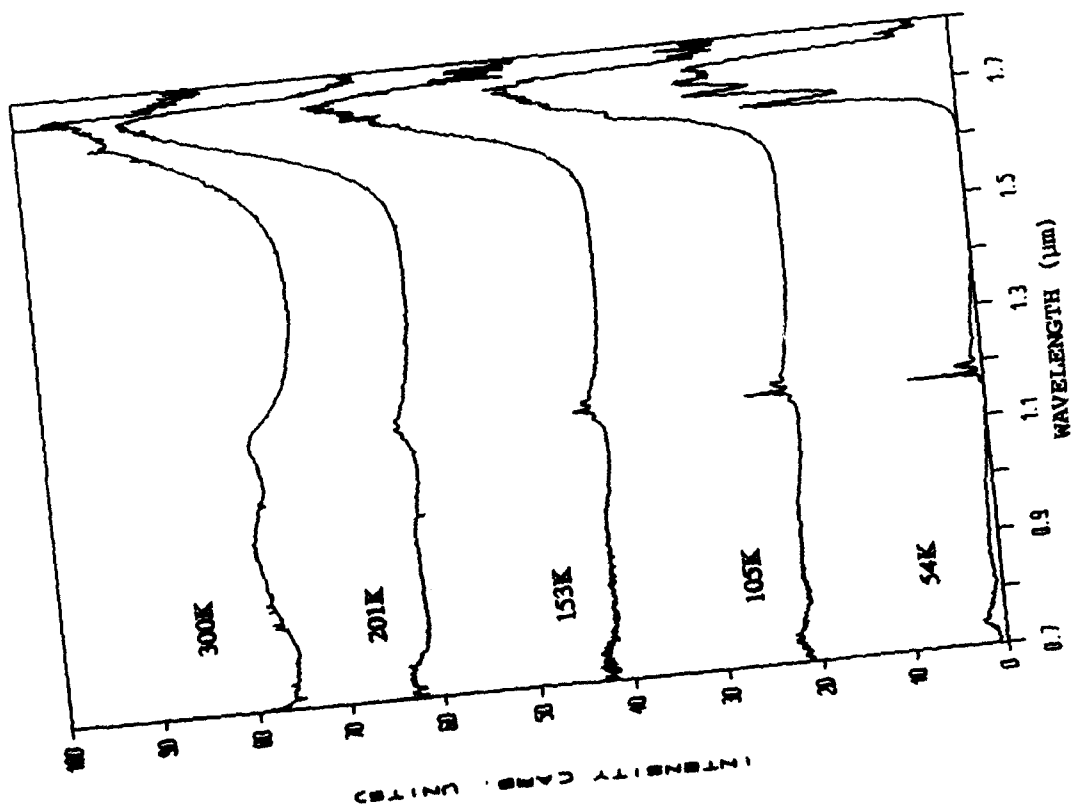


Fig. 4.4. The temperature dependence of the infra-red emission of MgNb₂O₆:Ni up to room temperature.

seems to occur for $Dq = 721 \text{ cm}^{-1}$, $B = 823 \text{ cm}^{-1}$ and $C = 3704 \text{ cm}^{-1}$. Therefore, $C/B = 4.50$ and $Dq/B=0.88$. The Sugano-Tanabe diagram for the case of $\text{Ni}^{2+}(d^8)$ with $C/B = 4.50$ is shown in Fig. 4.7. The vertical line at $Dq/B=0.88$ indicates values for the energy levels calculated for $\text{MgNb}_2\text{O}_6:\text{Ni}^{2+}$.

4.2.2 Lifetime Studies.

Attempts were made to measure the luminescence decay times for the green, 900 nm, and 1.2 μm emissions at low temperatures, initially using the EG&G multichannel scaler which had a minimum bin width of 2 μs . It was not possible to measure the decay time of 1.7 μm band as it occurred outside the wavelength regime of the S-1 or S-20 photomultiplier tubes. The large instrument time constant ($\sim 1.2 \text{ ms}$) of the Ge detector made it unsuitable for measuring lifetimes. Initial lifetime measurement efforts indicated that the low temperature lifetimes of all three measurable bands were $< 6 \mu\text{s}$. Using an acousto-optic modulator to chop the exciting beam, the lifetime of the green emission was found to be $< 60 \text{ ns}$ at 18K. As we were approaching the limit of our apparatus, only an approximate value could be determined. The measured value is very short compared to the estimated lifetimes of the green emissions in $\text{MgO}:\text{Ni}^{2+}$, KZnF_3 and MgF_2 of 48 μs , 580 μs and 400 μs , respectively. Although the Ni^{2+} site lacks inversion symmetry so that transitions are parity allowed, the transitions are spin forbidden, which makes the estimated low temperature lifetime for the green emission even more puzzling. The room temperature lifetime was too short to be measured. The fact that the three emissions have lifetimes $\ll 6 \mu\text{s}$, and seem to have the same lifetime, is consistent with our energy level assignments that all three transitions originate from the 1T_2 level.

4.2.3. Phase Sensitive Detection and Selective Excitation using a Ti-Sapphire Laser.

Phase sensitive detection techniques can be used to separate out overlapping luminescence components which have different decay times. It was found that by chopping the Ar^+ laser excitation beam at 1kHz and by nulling out the 900 nm and 1.2 μm emissions, the 1.7 μm band still remained but was reduced in intensity (see Fig. 4.8). This suggests that the 1.7 μm band has a different lifetime time, and because the chopping frequency was 1 kHz, has a lifetime of the order of 1 ms. This also suggests that the assignment of the 1.7 μm emission to the ${}^3T_2 \rightarrow {}^3A_2$ transition is correct.

It was found also that, by exciting the sample at 800 nm (12500 cm^{-1}) (ie. below the 1T_2 level) using a Ti-Sapphire laser, the 1.7 μm band was almost identical to that obtained using argon laser excitation. The ratio of the two largest peaks (I_A/I_B), is reduced for Ti-sapphire

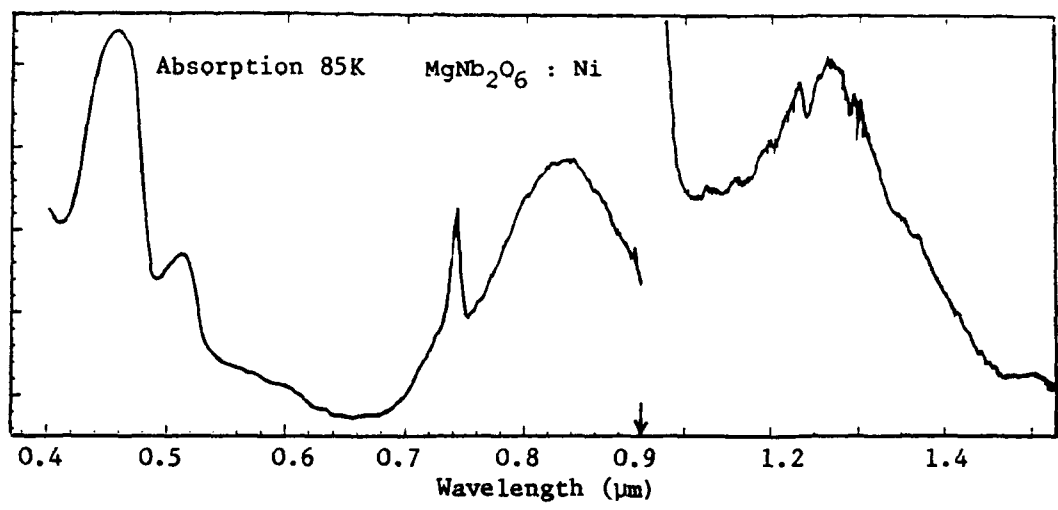


Fig.4.6. Low temperature absorption spectrum of $\text{MgNb}_2\text{O}_6:\text{Ni}$
 Note change of wavelength scale at arrow.

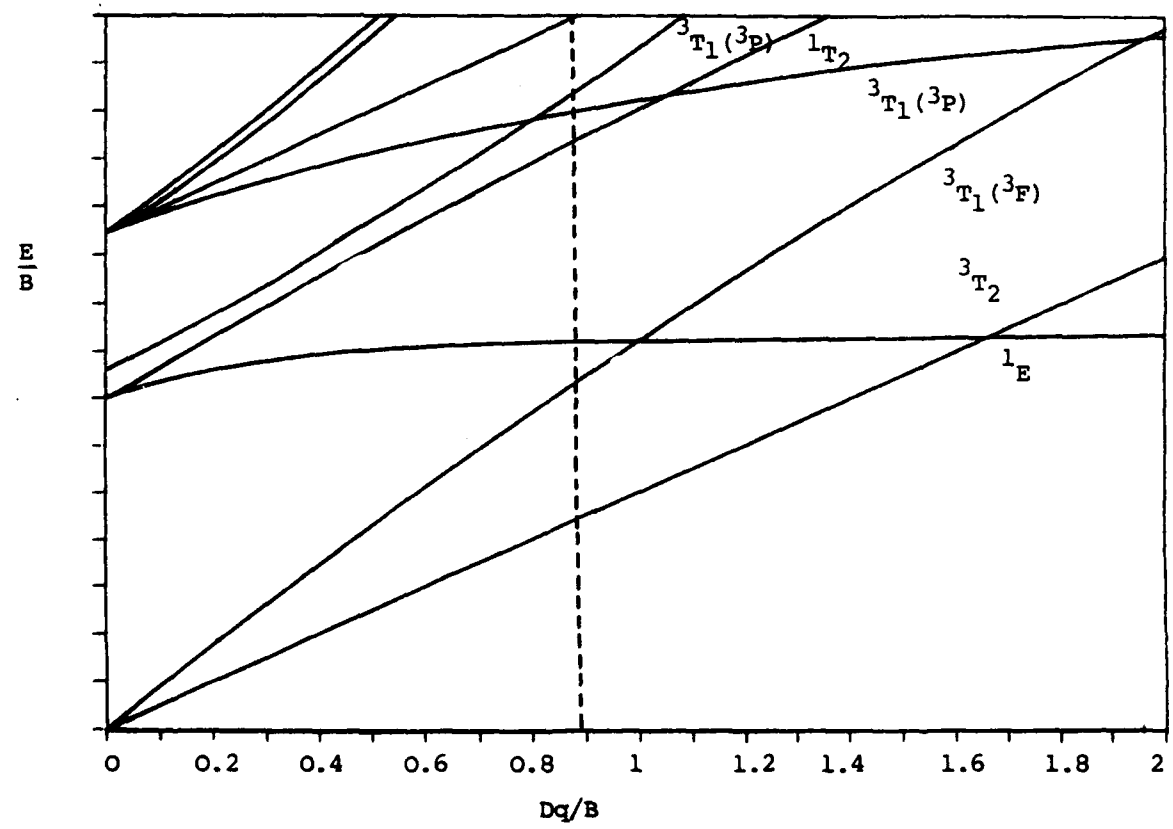


Fig. 4.7. The Sugano-Tanabe diagram for $\text{MgNb}_2\text{O}_6:\text{Ni}^{2+}$ with $C/B = 4.50$.

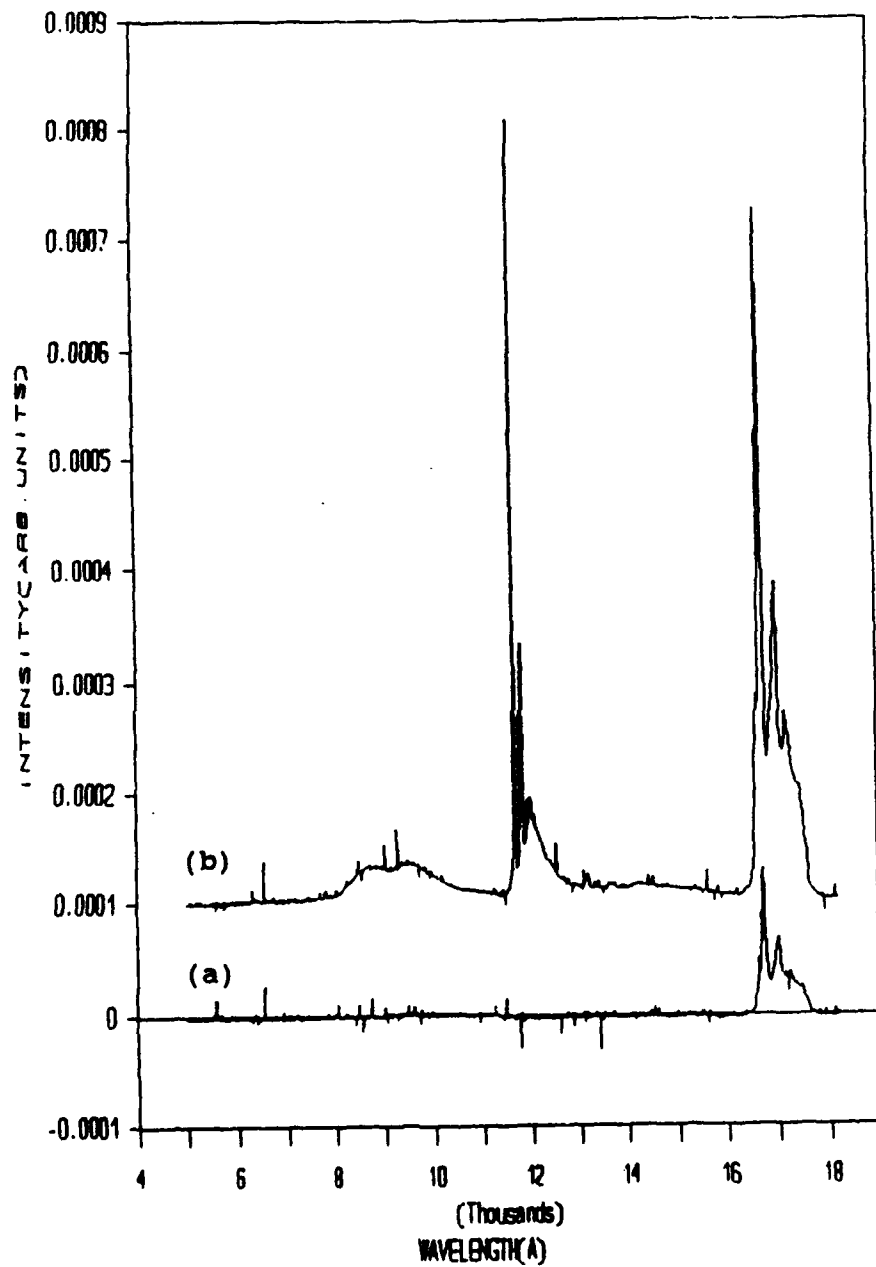


Fig. 4.8 Phase sensitive detection spectra for the near IR emission of $\text{MgNb}_2\text{O}_6:\text{Ni}^{2+}$ at 22 K. Spectrum (a) is nulled at 11694 Å and spectrum (b) is its quadrature.

laser excitation. Again this supports the assignment of the 1.7 μm band to the ${}^3\text{T}_2 \rightarrow {}^3\text{A}_2$ transition rather than the ${}^1\text{T}_2 \rightarrow {}^1\text{E}$ transition. Using Ti-Sapphire excitation, the ratio of the largest peak intensity to the second largest peak intensity of the 1.7 μm emission was less than for the case of Ar^+ excitation. A possible explanation for this is that when excited into the ${}^1\text{T}_2$ level using Ar^+ excitation an additional luminescence component occurs in the 1.7 μm band with a strong zero phonon line occurring at the same position as the zero-phonon line of the ${}^3\text{T}_2 \rightarrow {}^3\text{A}_2$ emission and a very weak sideband, and this additional luminescence component could be due to the ${}^1\text{T}_2 \rightarrow {}^1\text{E}$ transition.

As in the case of the Co^{2+} doped material, values for the Huang-Rhys parameters S and configurational coordinate offsets ΔQ can be evaluated from the shapes of the various bands in absorption and luminescence. The resulting single configurational co-ordinate diagram is shown in Fig. 4.9.

4.3 Luminescence of Ni^{2+} centers in forsterite (Mg_2SiO_4).

Stimulated by the discovery of tunable infra-red laser emission from Cr-doped forsterite and subsequent extensive studies of this material⁶¹, we have studied other 3d-ion centers in forsterite, such as Fe and Ni⁶², which also emit IR luminescence. Here we present emission and excitation spectra and lifetime measurements of Ni-doped (2% Ni) Mg_2SiO_4 at various temperatures down to 15 K.

In common with Ni^{2+} centers in some other oxide host crystals, we observe at least three separate emission bands; two of these (Fig. 4.10) are in the infra-red and what appears to be a composite band is observed in the visible (green). Below about 150 K, the dominant emission is a band peaking at about 1.5 μm ($6,700 \text{ cm}^{-1}$) with (at 15 K) a strong zero-phonon line at 1.37 μm (7280 cm^{-1}) and a lifetime of 1.2 ms. The phonon sideband shows some structure and the Huang-Rhys factor is in the range 1.5 - 2.0. Excitation spectra of this band (Fig. 4.11(a)), assigned to the ${}^3\text{T}_2 \rightarrow {}^3\text{A}_2$ transition of Ni^{2+} , show considerable splitting of the ${}^3\text{T}_2$ level due to distortions from octahedral symmetry and indicate that the emission is from the lowest split component. This emitting level is further split into three components by spin-orbit interaction as shown by three zero-phonon features. Due to Boltzmann factors, the two spin-orbit components at higher energy are only seen at low intensity in emission at temperatures around 100 K. The emission is thermally quenched at about 150 K, as shown in Fig. 4.11(b), which is a plot of the decay time of the emission against temperature. On the same plot is shown the variation of the emission intensity over the same temperature range, which confirms the lifetime data. The other infra-red band at around 1000 nm, assigned to the transition ${}^1\text{T}_2 \rightarrow {}^3\text{T}_2$, is broad and featureless (even at low temperature), is

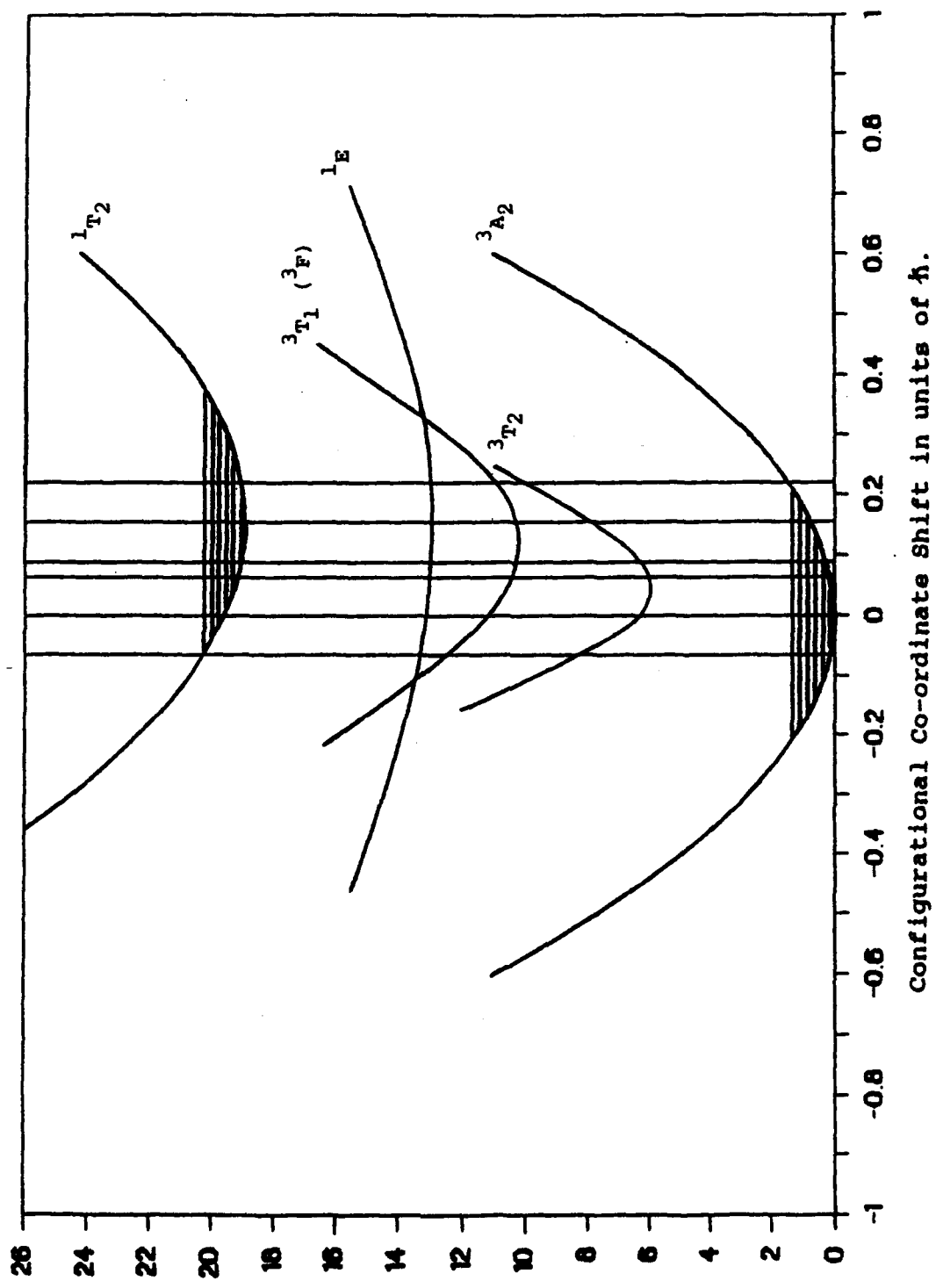


Fig. 4.9. Configurational coordinate diagram for the Ni^{2+} ion in $MgNb_2O_6$.

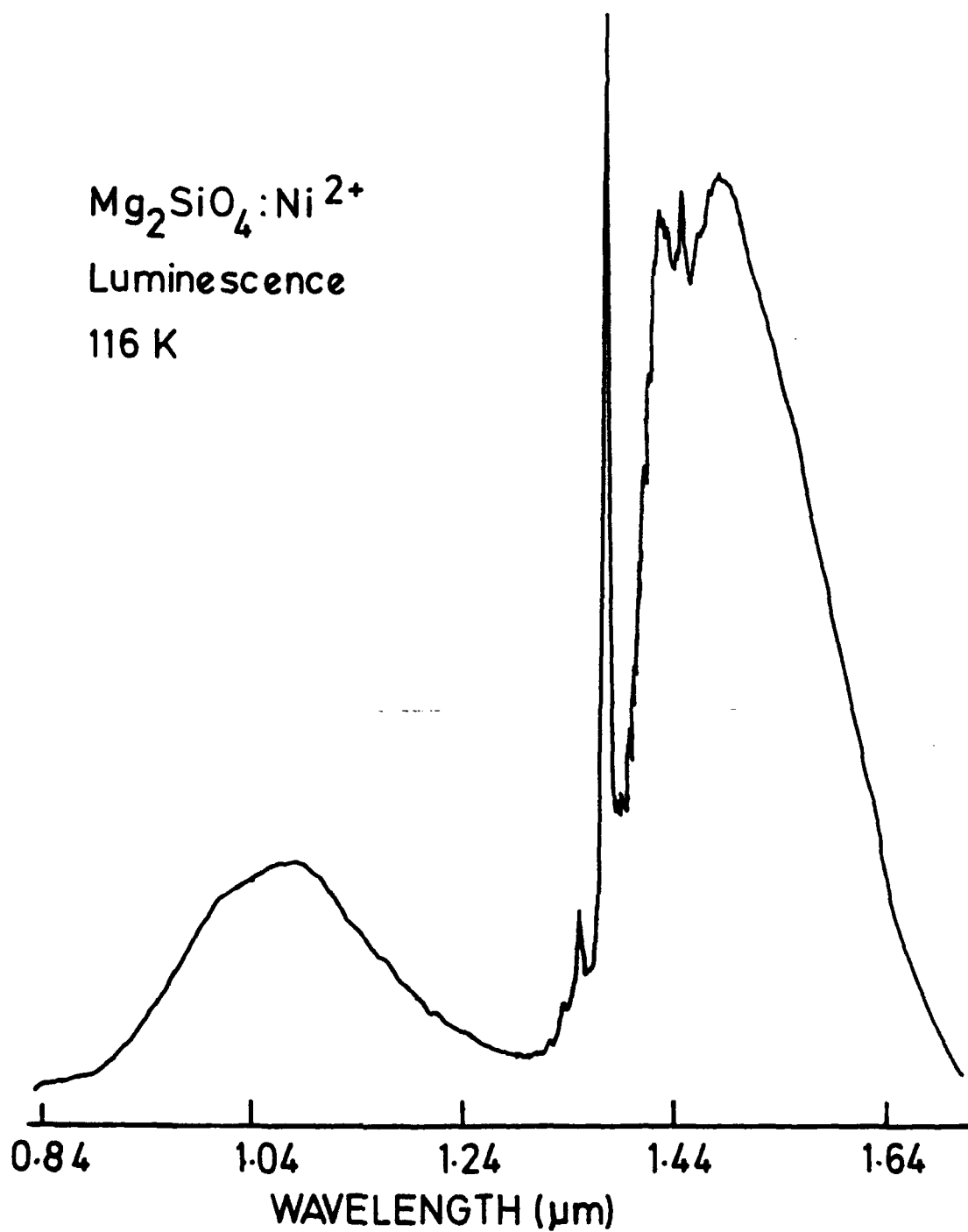


Fig. 4.10 Luminescence spectrum (at 116 K) of $\text{Mg}_2\text{SiO}_4:\text{Ni}$ excited by an argon ion laser. Correction for the spectral response of the detector has not been included.

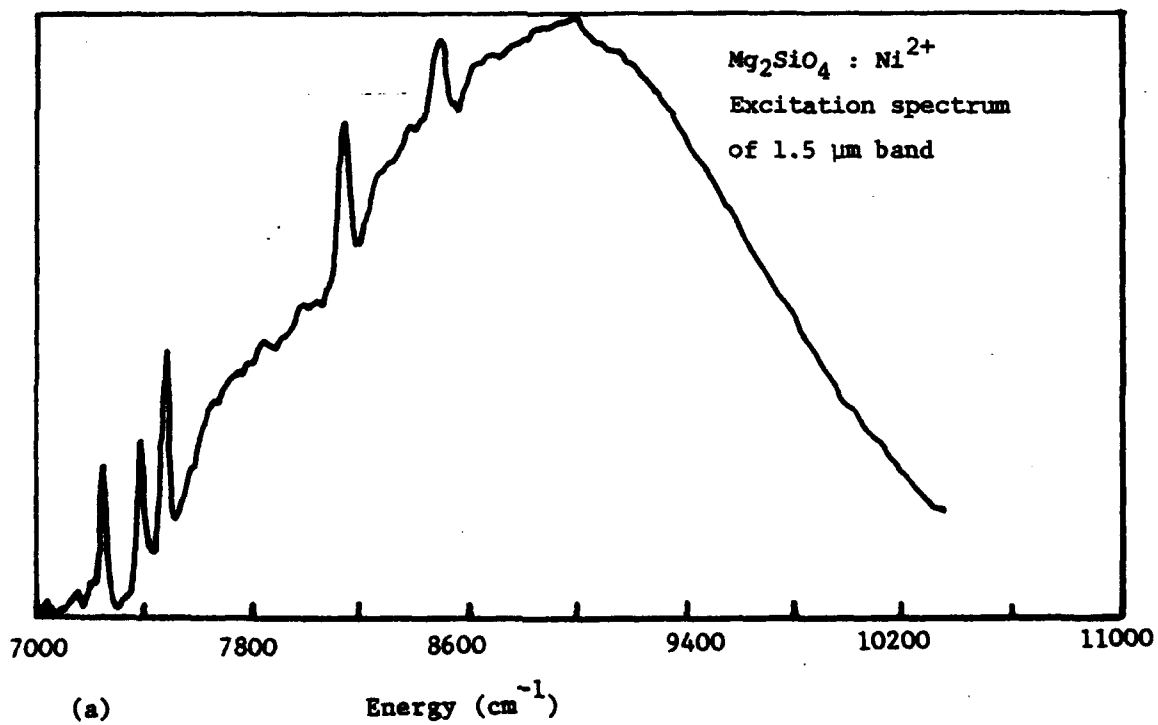
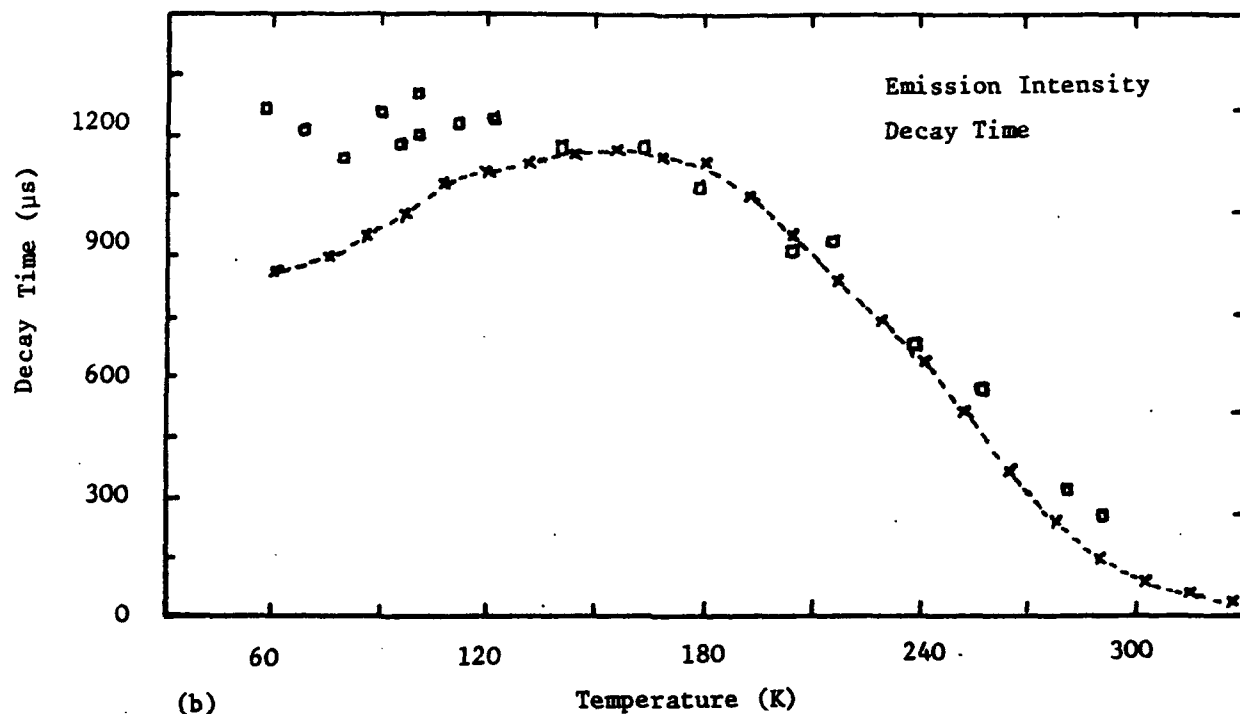


Fig. 4.11 (a) Excitation spectrum of the long-wavelength band shown in Fig. 4.10. (b) Plot of the decay time (), and emission intensity (), versus temperature of the same band.

not temperature quenched to the same extent as the 1.4 μm band, and is in fact the dominant band at room temperature. We are continuing our studies of this material. We have requested samples of Co-doped forsterite for our survey but have not yet received delivery of same. The visible emission, though comparatively weak, consists of two broad components at low temperatures which may indicate that two emitting states are involved. Although there are two possible metal cation sites which the Ni^{2+} ions can occupy (both of which are distorted octahedral sites), the data suggests that the Ni^{2+} ions populate only one of these sites and this is most probably the smaller (M1) site, in agreement with electron spin resonance studies.⁶³

4.4 Optical spectroscopy of $\text{ZnNb}_2\text{O}_6:\text{Ni}^{2+}$

The spectroscopic behaviour of this material is very similar to that observed for MgNb_2O_6 except for slight shifts in the positions of the various absorption and luminescence bands. The lifetime of the $^1\text{T}_2$ state is again very short (~ 100 ns), and the temperature dependence of all the bands take the same form as in the MgNb_2O_6 samples. Some representative spectra are shown in Fig. 4.12.

These materials are very interesting as they are the only oxides in which the crystal field at the Ni^{2+} site is sufficiently small that the various transitions are clearly resolved. In this respect, their spectra are similar to those reported for several Ni^{2+} -doped chlorides reported recently, except that the $^1\text{T}_2$ lifetime is mysteriously very short. The short lifetime does explain, however, why the green emission band is still unquenched at room temperature as the radiative rate is clearly comparable to, or faster than, the nonradiative rate in these materials at room temperature. Unfortunately, the lowest-energy IR band, the main candidate for laser action, is strongly temperature-quenched in these materials.

4.5 Luminescence of $\text{ZnAl}_2\text{O}_4:\text{Ni}^{2+}$ and $\text{LiAl}_5\text{O}_8:\text{Ni}^{2+}$

Our results on these materials will be presented together because of their similar behaviour. Both samples crystallize in the spinel structure and the Ni^{2+} ion occupies an approximately octahedral site in each case. The actual site symmetry is trigonal in the zinc aluminate; in the lithium spinel the Ni^{2+} the deviation from octahedral symmetry is more severe due to rhombic component in the local field. The ZnAl_2O_4 crystals were flux grown, pale green in colour, and of good optical quality. The LiAl_5O_8 crystals were grown by the laser heated pedestal technique at the University of Georgia (Athens, GA). Absorption and luminescence spectra for these materials are shown in Figs. 4.13. These materials have similar optical properties to LiGa_5O_8 , in that the luminescence consists of only one band ($^3\text{T}_2 \rightarrow ^3\text{A}_2$) and the lifetime of this emission changes very little from 20 K (340 μs for LiAl_5O_8) to 300 K (270 μs for LiAl_5O_8). This suggests that the quantum efficiency of this systems is quite high, although we are not able to estimate this quantity directly. In contrast to

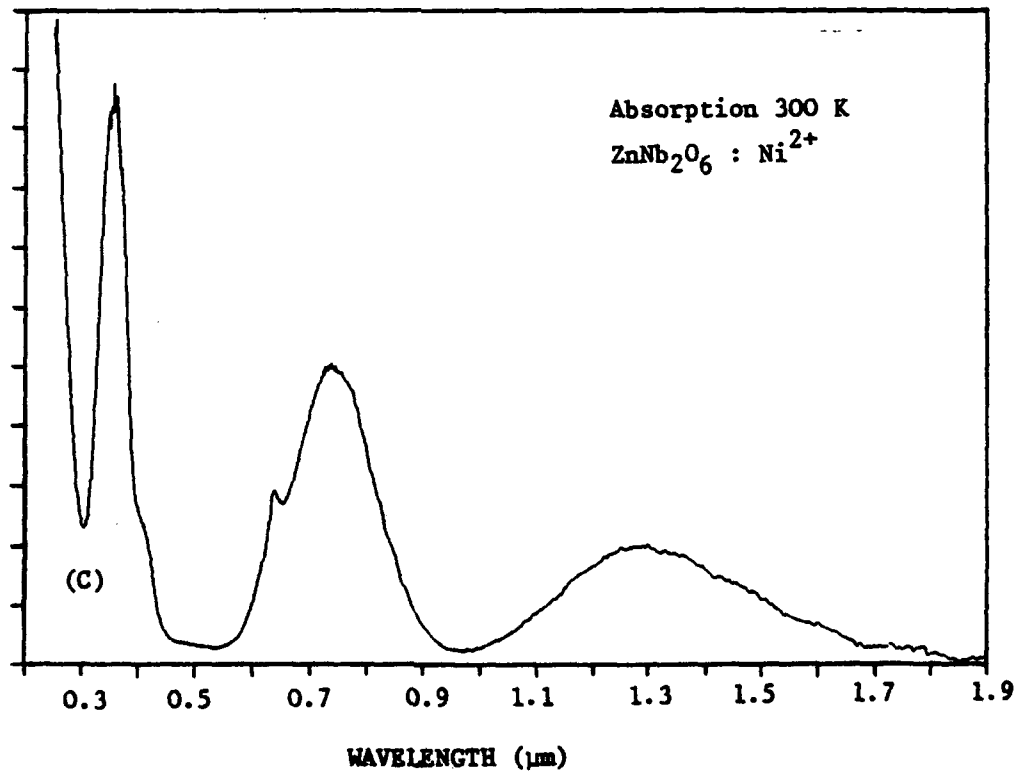
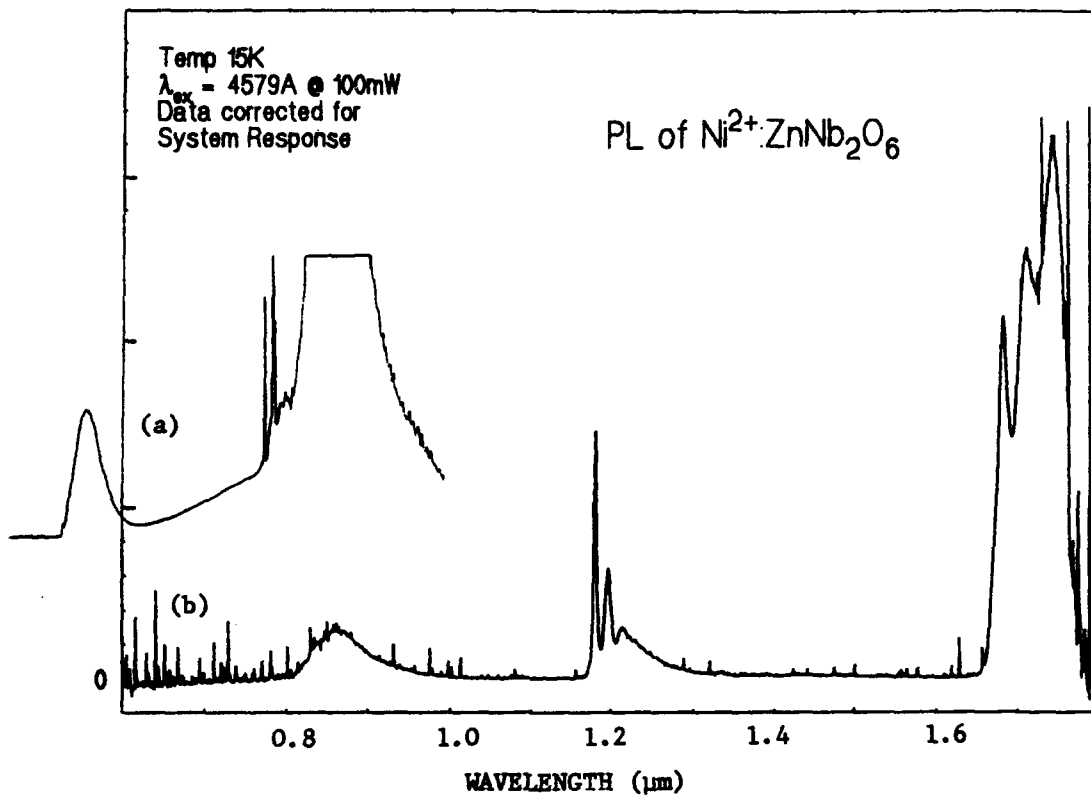


Fig. 4.12 Emission spectra of $\text{ZnNb}_2\text{O}_6:\text{Ni}$ recorded at 15 K using (a) S-20 photomultiplier, and (b) Ge detector. (c) Absorption spectrum at room temperature.

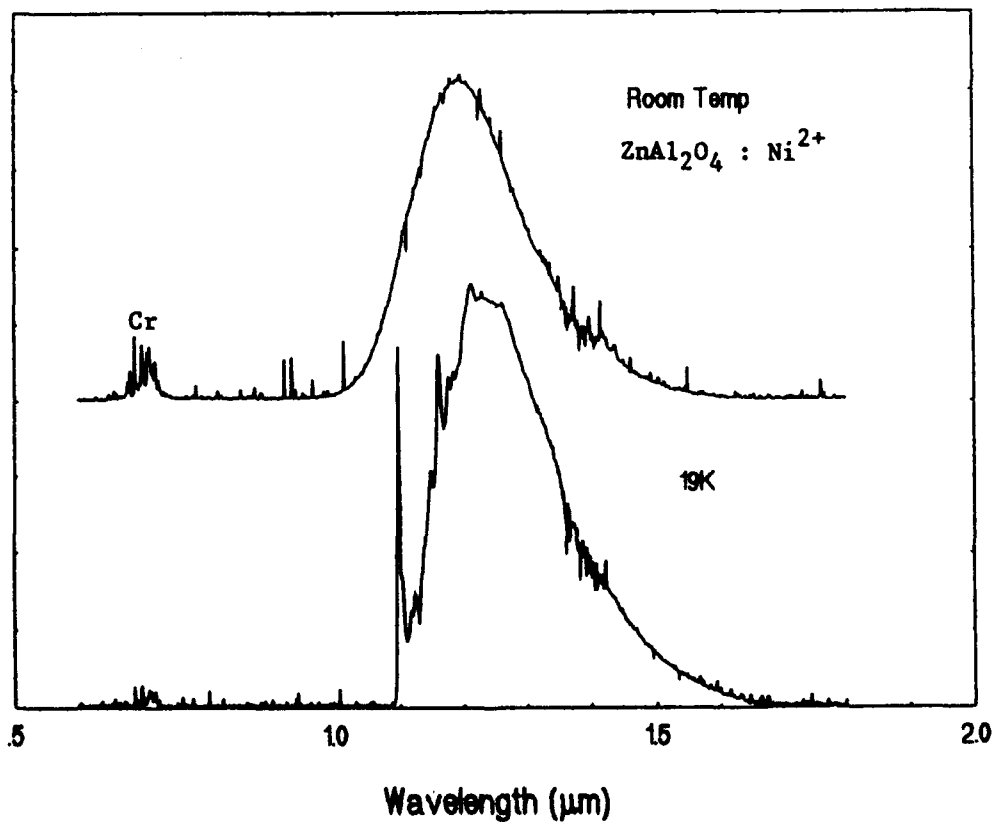
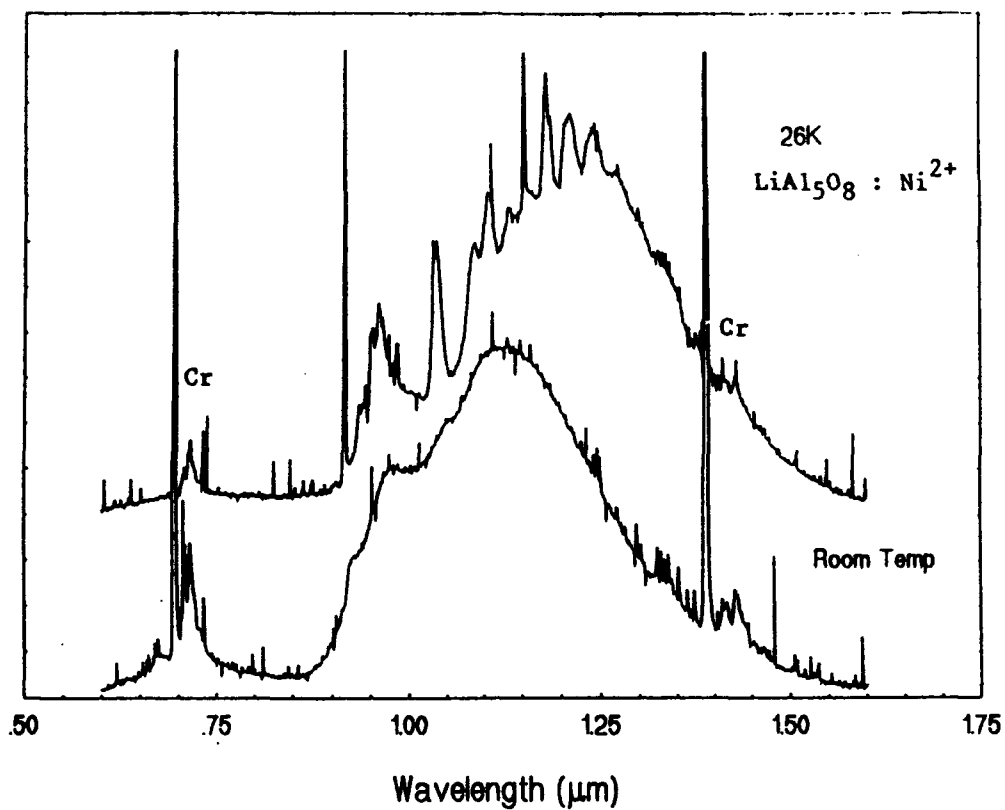


Fig. 4.13. The ${}^3T_2 \rightarrow {}^3A_2$ band in emission recorded at low temperature and at room temperature for (a) LiAl₅O₈:Ni²⁺ and (b) ZnAl₂O₄:Ni²⁺

LiGa_5O_8 , both materials show a sharp zero-phonon line and significant structure in the broad accompanying sideband. (In both materials, there are some additional sharp features which can be definitely assigned to luminescence from trace amounts of Cr^{3+} impurities). The crucial question, the answer to which will decide the usefulness of these materials as laser media, is whether excited state absorption is a limiting factor. Although we are not equipped to answer this question, we are attempting (in collaboration colleagues in the University of Georgia and in the Bell labs) to obtain samples of such quality that such measurements can be made. Our initial interest was in LiGa_5O_8 , but it is difficult to grow good quality samples of this material because of the volatility of the gallium oxide. The aluminate was much easier to grow and the sample whose spectra are presented here was a product of our program to obtain better samples. There is a general trend, however, that ESA is less likely to be a problem the greater the crystal field at the Ni^{2+} site. If this is so, then LiAl_5O_8 shows definite promise as a potential tunable laser medium in the future. We propose to carry out a more detailed analysis of this material to assess the likelihood of ESA before embarking on a major growth program.

4.6. Conclusion

The data presented in this chapter emphasises that our understanding of the spectroscopy of the Ni^{2+} ion in solid hosts is still incomplete. There are wide variations in the characteristics (lifetime, relaxation mechanisms, etc.) of the luminescence, even among materials with very similar structures. It is clearly worthwhile to study these materials in greater depth in order to deepen our understanding of the interaction of transition metal ions with crystalline host materials. While some of the materials described in this chapter show promise as tunable solid-state media, excited state absorption measurements must be carried out to characterise these materials more completely.

CHAPTER 5

Cr-DOPED MEDIA.

5.1 Introduction.

The development of the alexandrite laser system⁶⁴, based on the spin allowed ${}^4T_2 - {}^4A_2$ transition on the Cr^{3+} ion in $BeAlO_4$, has led to a search for analogous Cr-doped crystalline materials in which the 2E and 4T_2 levels are sufficiently close to allow significant population of the latter at room temperature. These studies have led to other laser materials such as $GSGG:Cr^{3+}$ and $ZnWO_4:Cr^{3+}$, which are pumped (using either flashlamps or other lasers) in the strong absorption bands of the Cr^{3+} ion. In this chapter, we present optical measurements of the crystalline material $BiGaO_3:Cr^{3+}$ and $LaSr_2Ga_{11}O_{20}:Cr^{3+}$ which show many of the properties required for a laser medium. In the former, the existence of energy transfer from the Bi^{3+} ions to the Cr^{3+} ions allows the possibility of more efficient excitation by broadband sources. A large amount of research has also been devoted recently to the study of Cr^{4+} systems, since the assignment of the laser transition of Cr-doped forsterite to the lowest energy transition (${}^3T_2 \rightarrow {}^3A_2$) of the Cr^{4+} ion in a tetrahedral site. In this chapter, we describe also the results of our measurements on several materials in which Cr (as Cr^{4+}) is substituted on tetrahedral sites.

5.2 Optical Spectroscopy of $BiGaO_3$

The samples of $BiGaO_3$ used in this study were flux-grown in the Bell Labs. The undoped samples were pale yellow; the Cr-doped samples were a light green colour. When examined in a polarising microscope, the samples were found to be uniaxial and to have a multidomain structure. Many oxide materials with the general formula ABO_3 adopt the perovskite structure (Fig. 5.1), or some distortion of this structure. For example, $BiFeO_3$ has been reported to have a structure derived from perovskite by a rhombohedral distortion.⁶⁵ Because of the similarity in the ionic radii of Fe^{3+} and Ga^{3+} we expect the structure of this material to be a good guide to the likely structure of $BiGaO_3$.

Raman scattering experiments were carried out on $BiGaO_3$ in an attempt to determine the space group for this structure. At 80 K, 23 Raman modes were observed; at room temperature only 16 definite modes were identified. Due to the multidomain nature of the samples, it was not possible to determine the symmetry of the observed Raman modes. From the Raman data, $BiGaO_3$ cannot have a structure like that of the low temperature form of $SrTiO_3$ (D_{4h}^{18}) since this would result in 5 Raman modes. The structure of $PrAlO_3$ (R3C) has only 8 Raman modes. The space group (R3C) for $BiFeO_3$ results in 13 Raman-allowed modes. As these 13 Raman modes are also IR active, each mode will be split into a doubly-

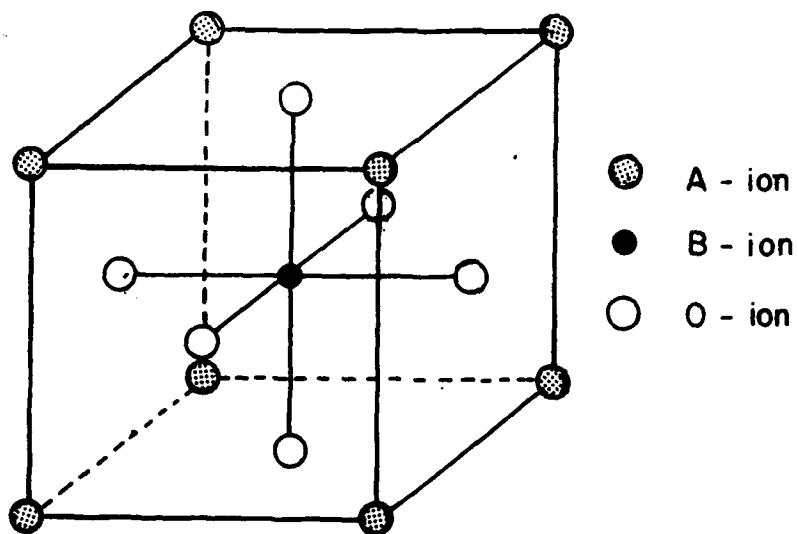


Fig. 5.1(a). Cubic ABO_3 perovskite structure

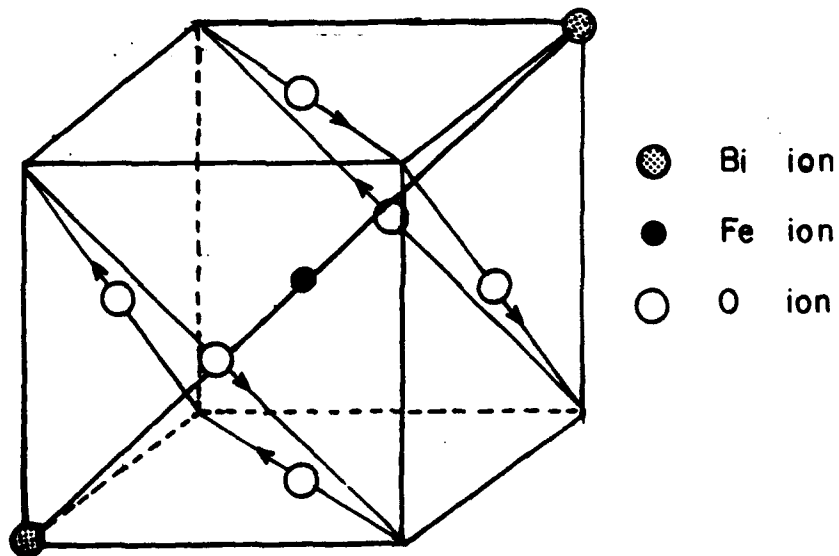


Fig. 5.1(a). Distorted perovskite structure of $BiFeO_3$.

degenerate transverse optic (TO) mode and a non-degenerate longitudinal optic (LO) mode, i.e. 26 Raman-allowed modes altogether. The observation of 23 Raman modes in BiGaO₃ is consistent with a space group assignment of R3C for this structure.

In the rhombohedrally-distorted perovskite structure of BiFeO₃, the Fe³⁺ ions are displaced from the centre of the FeO₆ octahedra and the oxygen octahedra are rotated about their three-fold axes (Fig. 5.1 (b)). This material is both piezoelectric and ferroelectric. Its space group is the same as that of LiNbO₃, whose useful nonlinear properties have led to its optical properties being studied in some detail.⁶⁶ Above a certain temperature the B ions (in this case Nb) return to the centre of the oxygen octahedral which, however, are still rotated slightly about their threefold axes. Thus above 1490 K the LiNbO₃ crystal is again centrosymmetric.

5.2.1 Luminescence

The luminescence from Cr³⁺ impurities in BiGaO₃ was observed over the temperature range 10 - 550 K and spectra recorded at 10 K, 80 K and room temperature are presented here in Fig. 5.2. At 10 K the luminescence consists of a single sharp line at 14124 cm⁻¹ and a weak relatively featureless sideband extending to ~13500 cm⁻¹. The intensity of this sharp line relative to that at the peak of the sideband is ~ 8.5. This line at 14124 cm⁻¹ has a half width of ~ 12 cm⁻¹ at 10 K and there is a marked asymmetry in the shape on the low energy side. At 80 K this sharp line has shifted to 14119 cm⁻¹, its half-width is ~ 15 cm⁻¹ and the asymmetry in the line shape is still in evidence. A second sharp line has begun to appear at 14286 cm⁻¹ and the sideband structure shows very little difference from that observed at 10 K. The spectrum changes considerably between 80 K and room temperature, the feature B at 14286 cm⁻¹ growing in intensity relative to the line A at 14119 cm⁻¹. Both lines broaden considerably and shift to lower energy with increasing temperature. In the room temperature spectrum the two lines, A and B, and the sideband are all sitting on a broad band extending from ~ 14800 cm⁻¹ to ~ 11800 cm⁻¹ with a peak at ~ 13400 cm⁻¹. From the temperature dependence of the intensity ratio I_B/I_A, it was clear that A and B are the R-lines, corresponding to the ²E → ⁴A₂ transition. The large R-line splitting indicates that the luminescence originates on Cr³⁺ ions in sites with a large low-symmetry crystal field.

When compared with other systems containing Cr³⁺ ions in distorted octahedral sites, the half-width of the R₁ line at low temperatures is very large. (cf. the half width of the R₁ line in Al₂O₃ : Cr³⁺ at low temperatures ~ 0.5 cm⁻¹ with ~ 12 cm⁻¹ in BiGaO₃ : Cr³⁺.) The large half-width may be related to the asymmetry in the R₁ line-shape. It was noted also that the position of the R-line shifted by ~ 55 cm⁻¹ between 10 - 300 K. Such line shifts in the luminescence from impurity ions in crystals can usually be explained by taking into account the coupling of the ions to the lattice vibrations.

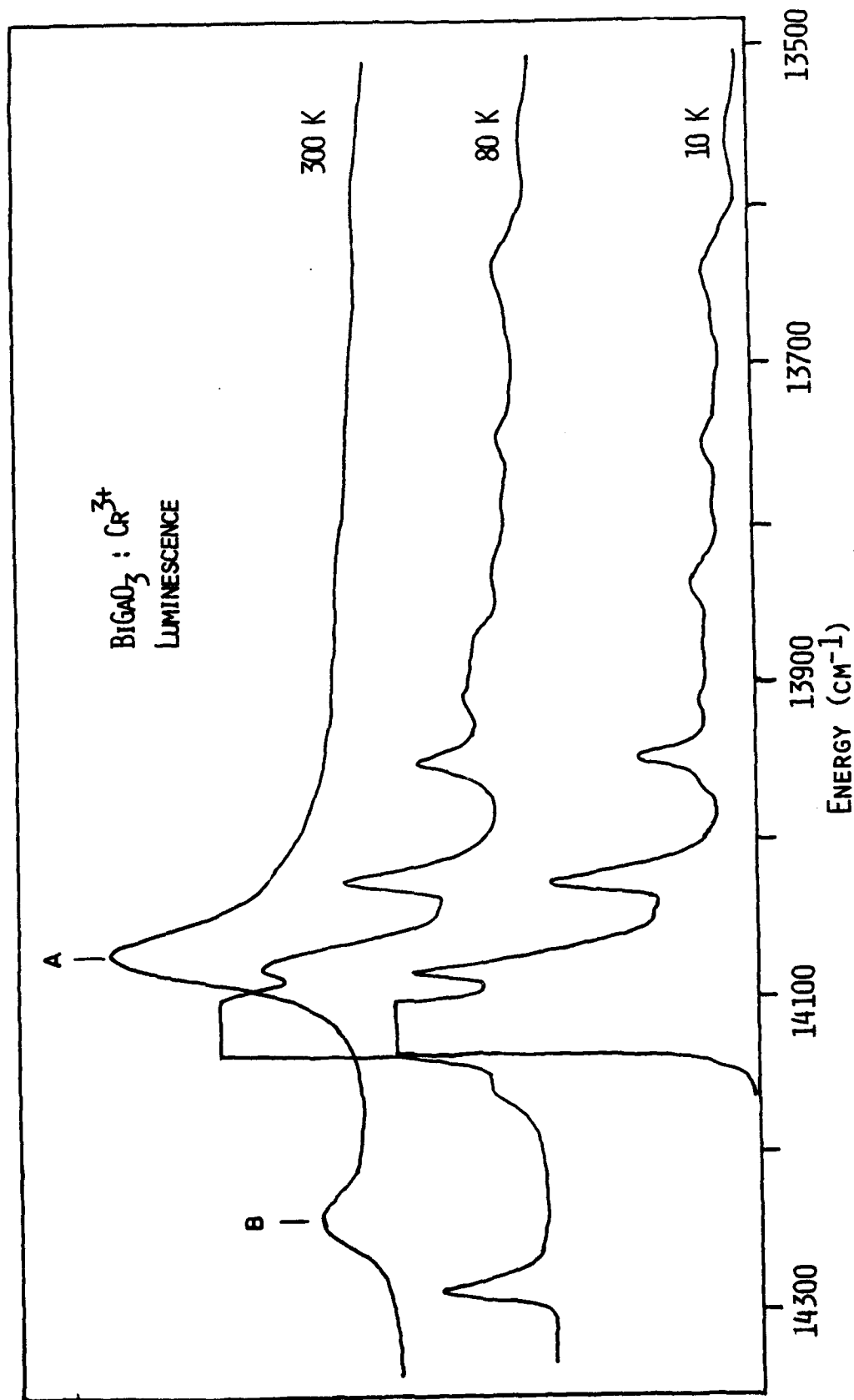


FIG. 5.2. LUMINESCENCE SPECTRUM OF $\text{BiGaO}_3:\text{Cr}^{3+}$ AT 10 K, 80 K AND ROOM TEMPERATURE.

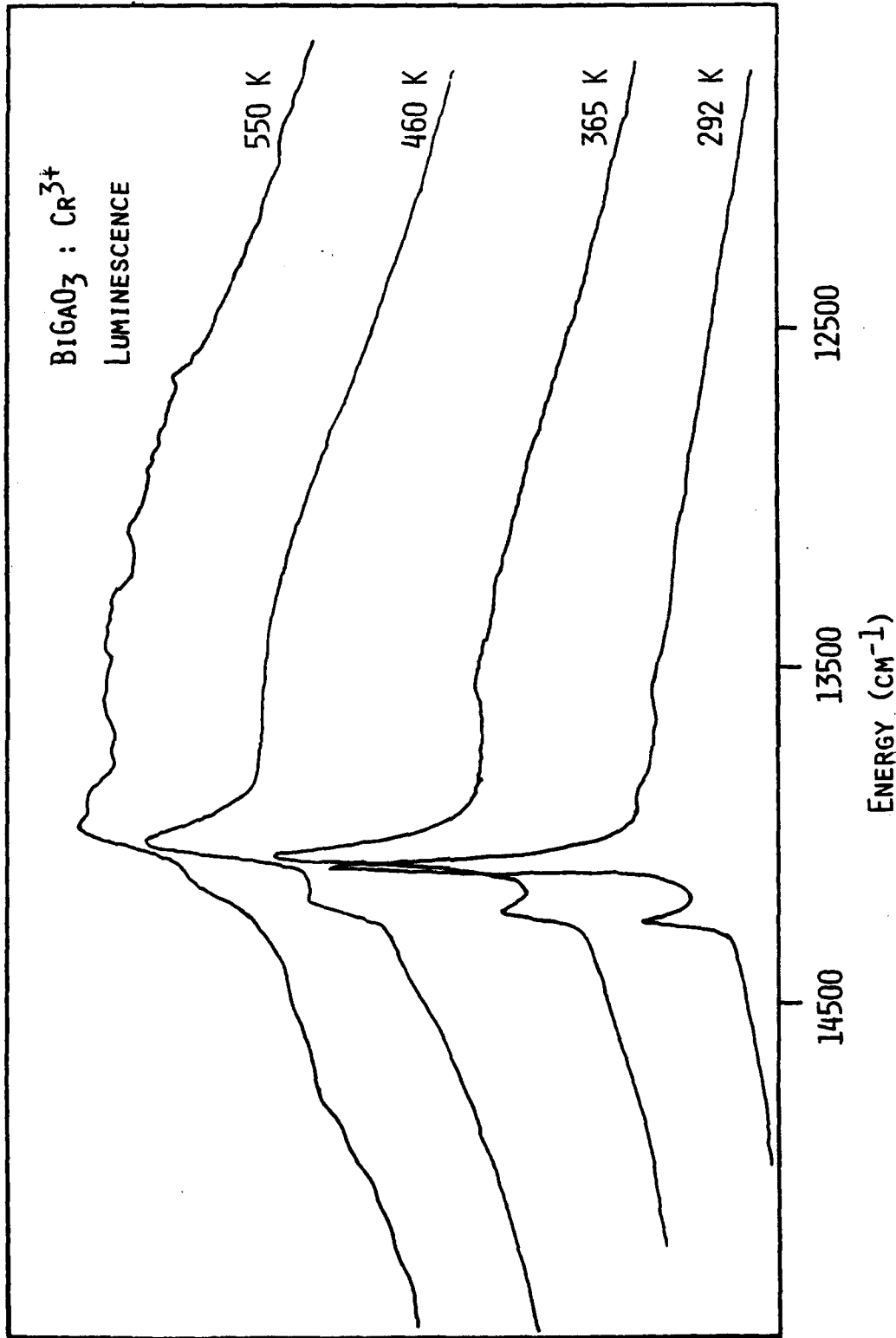


FIG. 5.3. LUMINESCENCE SPECTRUM OF $\text{BiGaO}_3 : \text{Cr}^{3+}$ RECORDED AT VARIOUS TEMPERATURES 292 - 550 K.

Above room temperature, the broad band grows in intensity relative to the R-lines (Fig. 5.3) until, at 550 K, these lines have almost disappeared. The appearance of such broad luminescence bands with increasing temperature in many of d^3 systems is attributed to ${}^4T_2 \rightarrow {}^4A_2$ luminescence. Only a very small population is necessary in the 4T_2 level for the ${}^4T_2 \rightarrow {}^4A_2$ transition to be observed in luminescence. The ratio of the populations of the 4T_2 and 2E states in such a system is $3 \exp(-\Delta/kT)$ where Δ is the energy difference between the zero vibrational levels. Thus, the observed luminescence from $\text{BiGaO}_3:\text{Cr}^{3+}$ is due to the small value of Δ since the broadband emission dominates the spectrum at temperatures < 500 K.

The radiative lifetime on the R_1 line at 10 K was measured to be $\sim 200 \mu\text{s}$. (Similar short lifetimes are observed in GSGG, due to mixing of the 2E and 4T_2 levels⁶⁷). At room temperature the lifetime was too short to be measured by the multichannel analyser. The decay rate observed at low temperatures indicates an electric dipole process. If the ${}^2E \rightarrow {}^4A_2$ transition is occurring via an electric dipole process then the environment of the chromium ion in the crystal must lack inversion symmetry. This conclusion is in agreement with the suggested space group $R3C$ for the structure since the gallium ions would be shifted off centre with respect to the surrounding oxygen octahedral in this space group. The very short lifetime observed at room temperature can be explained by the presence of the spin-allowed 4T_2 broad luminescence band at this temperature.

The excitation spectrum of chromium in BiGaO_3 was recorded at 77 K and was used to obtain the energies of the absorption bands in this material. Using the Sugano-Tanabe energy matrices for a d^3 system, values were estimated for the parameters, B , C and Dq which would fit the theoretically predicted energy levels to the excitation spectrum. The best fit was obtained for $Dq = 1570 \text{ cm}^{-1}$, $B = 660 \text{ cm}^{-1}$ and $C = 3100 \text{ cm}^{-1}$. The value of Dq obtained for $\text{BiGaO}_3:\text{Cr}^{3+}$ is considerably smaller than the values reported for MgAl_2O_4 and Al_2O_3 . However, it is larger than that reported for LiNbO_3 . This is consistent with the suggested interpretation of the observed luminescence; in LiNbO_3 , the smaller value of Dq results in the 4T_2 being the lowest excited state and the observed luminescence consists of a broad band.⁶⁸

Since the zero-phonon line of the 4T_2 band was not observed in excitation, no accurate estimate of Δ , the energy difference between the ground vibrational levels of the 4T_2 and 2E states, could be made. However, from the excitation spectrum, we estimate that it should be $\sim 350 \text{ cm}^{-1}$ at 77 K. This 4T_2 level is expected to shift downward with increasing temperature. In ruby the shift has been estimated to be $\sim 1.4 \text{ kT}$. If we assume that the magnitude of the shift will be similar in this case then the variation of the ${}^4T_2 - {}^2E$ energy difference as a function of temperature may be expressed as

$$\Delta(T) = \Delta(0) - 1.4 \text{ kT}$$

and, on this basis, we would expect the 4T_2 level to begin to overlap the 2E level at a temperature of $\sim 380\text{K}$. However, the 2E level is also moving to lower energy⁶⁹ and has

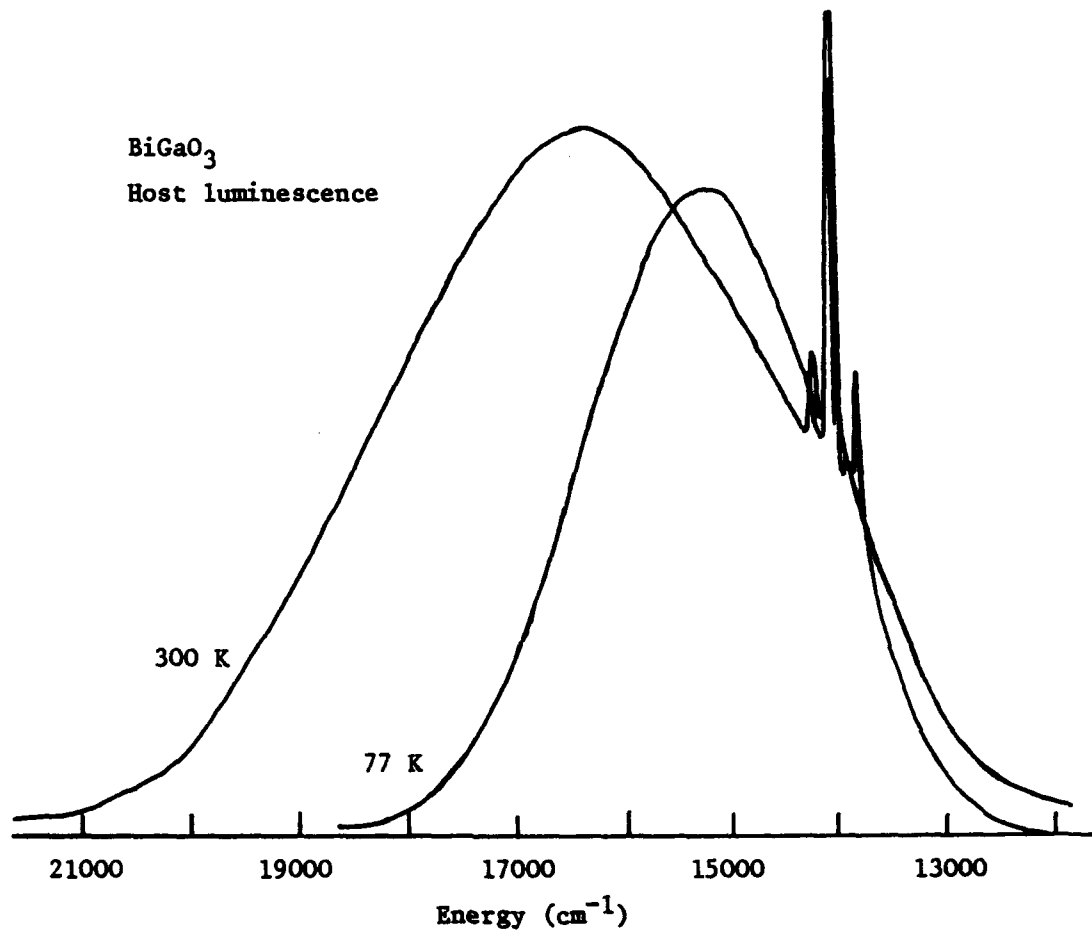


Fig. 5.4. Broadband luminescence, excited by an argon laser, of the BiGaO₃ crystal.

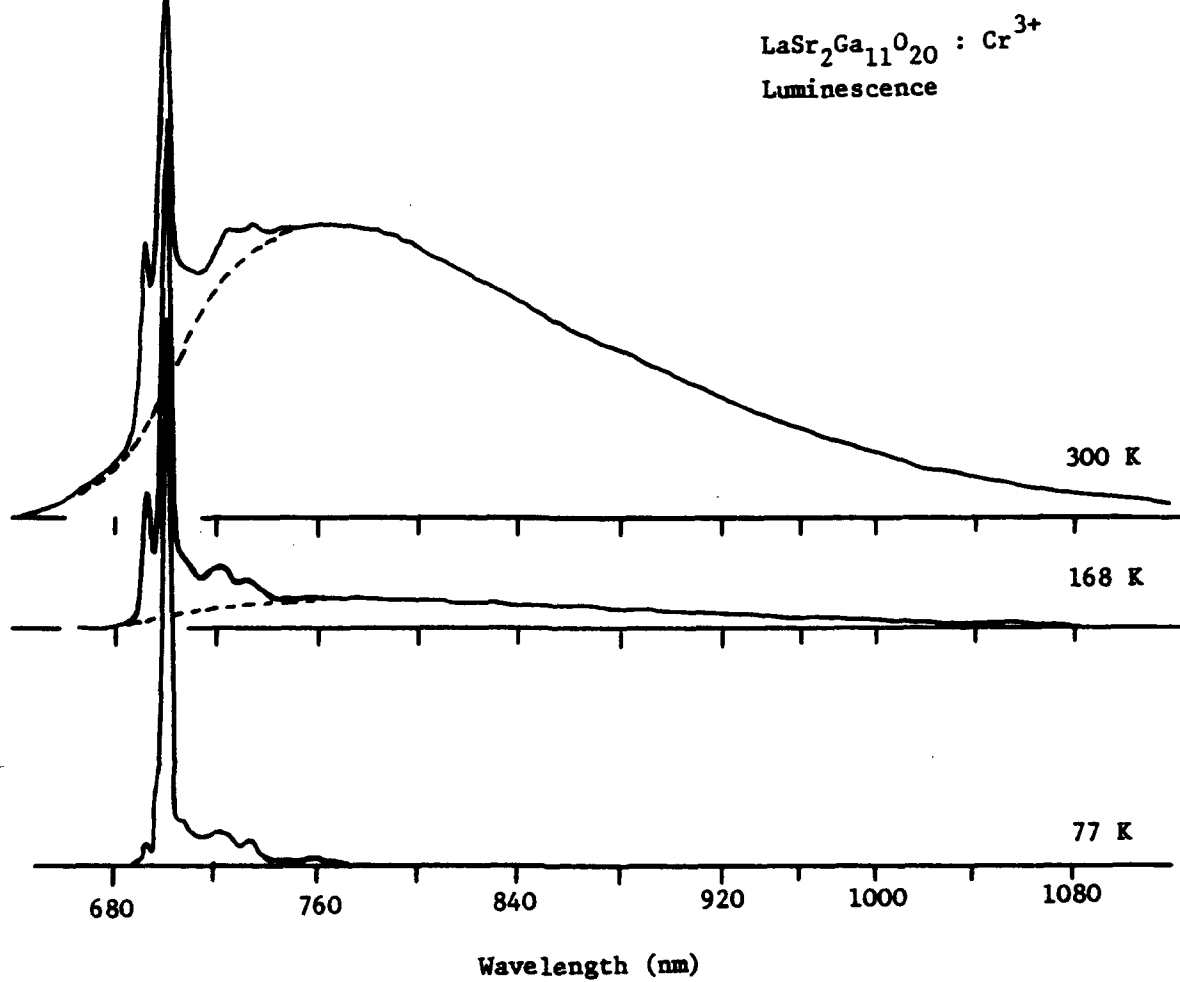


Fig. 5.5. Luminescence spectra of $\text{LaSr}_2\text{Ga}_{11}\text{O}_{20} : \text{Cr}^{3+}$ at different temperatures.

overlapping R-lines. Phase resolved luminescence spectra have been used to resolve partially the emission from the two sites. The decrease in the lifetime with increasing temperature is probably due to changes in the 2E , 4T_2 mixing rather than a reduction in fluorescence efficiency.

5.4 $Mg_2SiO_4:Cr$

Forsterite (Mg_2SiO_4), like alexandrite, is a member of the olivine family, with an orthorhombic crystal structure. When doped with Cr ions, it can support laser action over a limited spectral range around 1.2 μm .^{71,72} However, there was some controversy concerning both the Cr valence state, the sites occupied by the Cr ion in this material, and the possibility of laser pumping by transfer from Cr^{3+} to Cr^{4+} ions. For this reason, we investigated the spectroscopy of this material doped with various levels of chromium. The complete luminescence spectrum, which is quite sensitive to the wavelength and the polarisation of the excitation⁷¹ is shown in Fig. 5.6. At low temperatures, it consists of several sharp features at around 700 nm, some broad bands at about 800 nm and 1000 nm, and further sharp features at 1100 nm. The latter broaden with increasing temperature (see Fig. 5.7) and develop into the lasing band at room temperature. The sharp line emission in the 700 nm region corresponds to the $^2E \rightarrow ^4A_2$ transition on Cr^{3+} ions which replace Mg^{2+} ions in distinct octahedral sites, one with inversion symmetry (M1) and one with mirror symmetry (M2), as well as a perturbed M1 site, possibly arising from charge compensation. Cr^{3+} ions in such sites have distinct ground splittings, measured using E.P.R.,⁷³ which are resolved in the R_1 emission at low temperature and which clearly identify the Cr^{3+} site. The energy-level structure for the Cr^{3+} ions is similar to that in alexandrite [1] and with increasing temperature the higher-lying 4T_2 level becomes populated so that emission from this level dominates the spectrum at room temperature (Fig. 5.7). The lifetime varies from 8.9 ns at low temperature to 340 μs at room temperature and can be fitted to a purely radiative model for the emission. The variation of the lifetime can be fitted to the expression

$$\frac{1}{\tau} = \frac{f_E + 3 f_T \exp(-\Delta/kT)}{1 + 3 \exp(-\Delta/kT)}$$

with values of $114 s^{-1}$ and $10^4 s^{-1}$ for the radiative rates f_E , f_T from the 2E and 4T_2 levels, respectively, and $450 cm^{-1}$ for the energy separation Δ between 2E and 4T_2 . We find no evidence for any energy transfer from Cr^{3+} ions to the IR lasing centre, which was suggested by other workers,⁷¹ or for any nonradiative component in the emission from these ions up to room temperature. The spectroscopy of the Cr^{3+} emission is described in more detail in two publications in Appendices 3,4. In an attempt to understand the host material more fully, we investigated Fe-doped forsterite also. Details of our results are contained in a

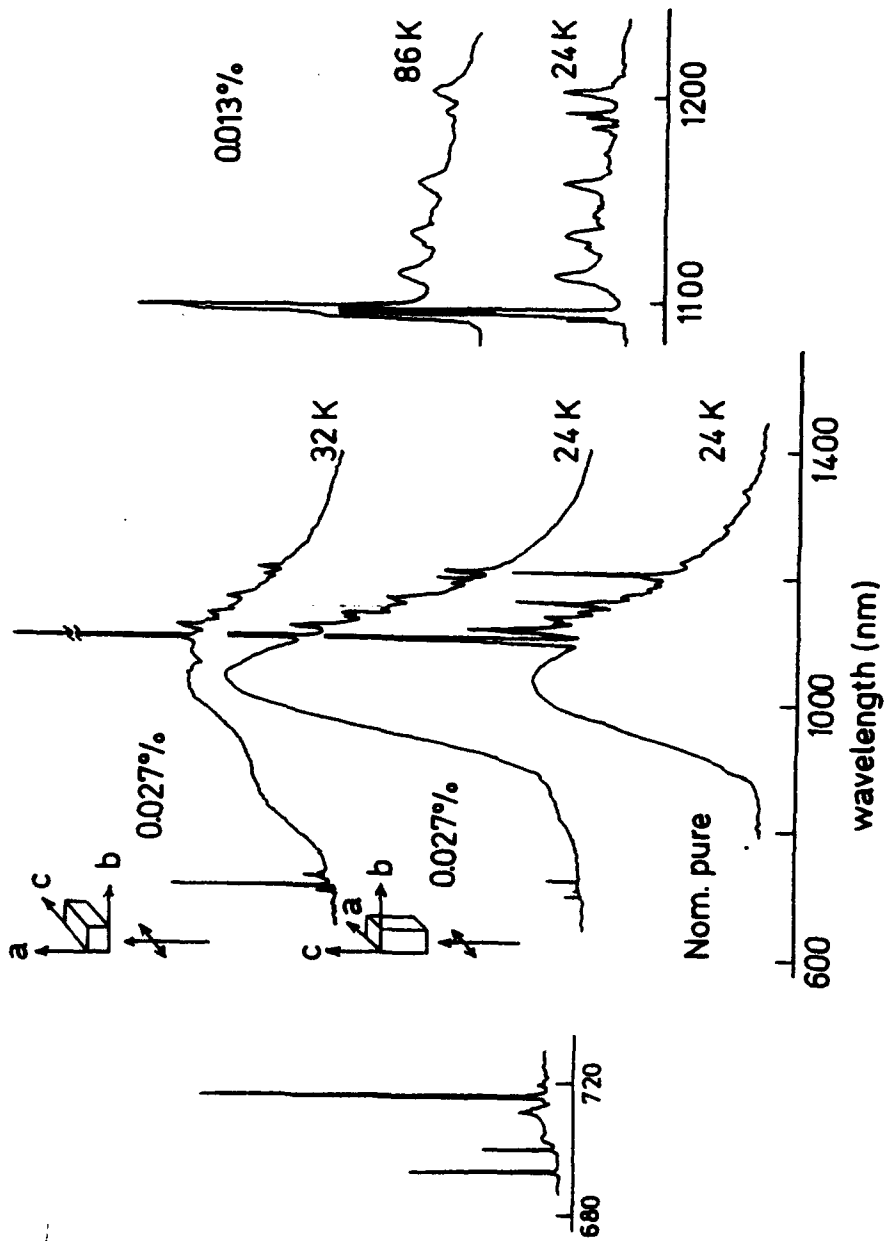


Figure 5.6. The low-temperature emission from Mg₂SiO₄ (forsterite) doped with chromium excited by an argon-ion laser (all lines). The sharp features at 700 nm and 1100nm are shown at higher resolution.

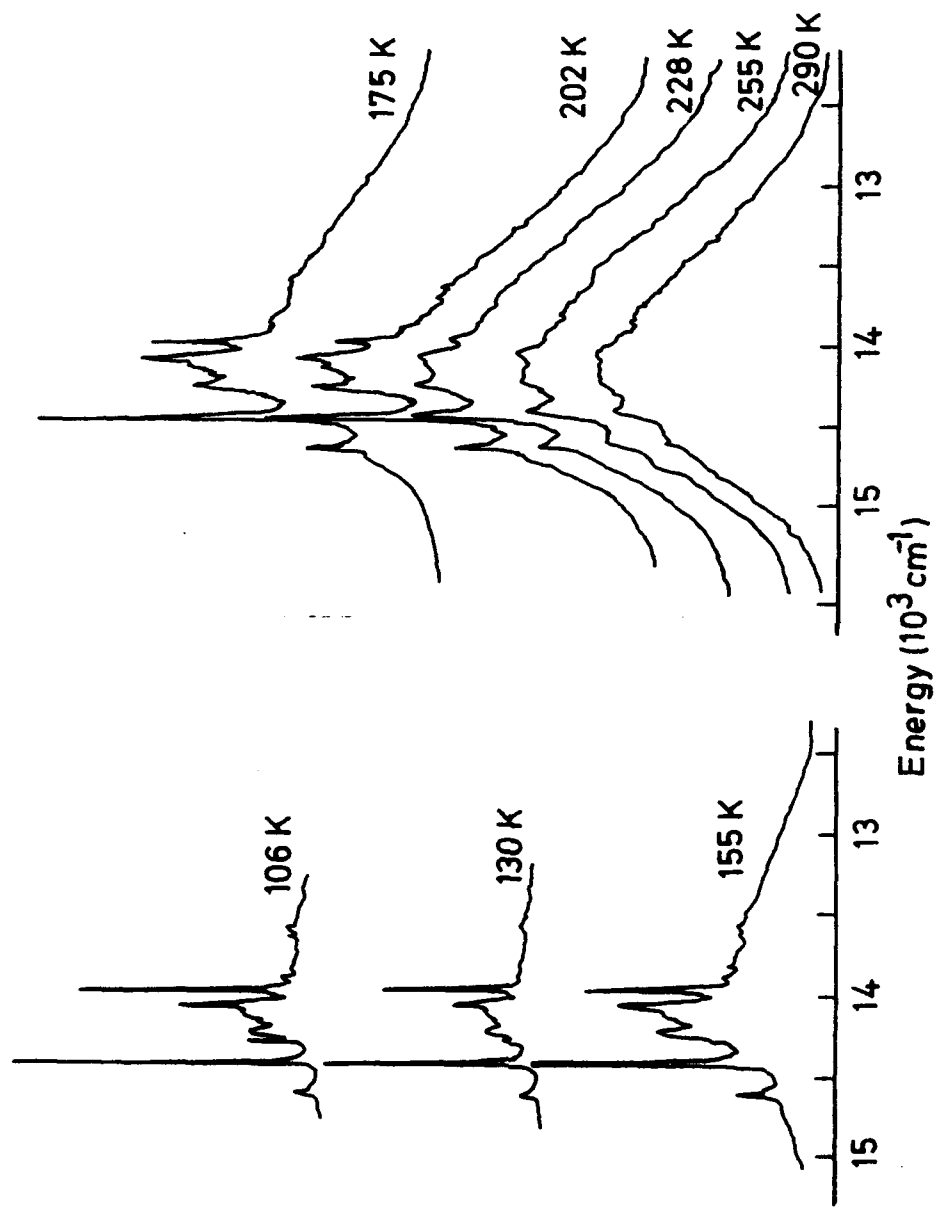


Figure 5.7. The luminescence from Cr³⁺ centres in forsterite at various temperatures. The chromium doping level was 0.027%.

publication in Appendix 5.

Despite its high efficiency, this system is prevented from lasing due to absorption by another center (now generally accepted to be Cr^{4+} in tetrahedral Si sites^{71,72} which is the basis for the demonstrated laser action in this material in a band centred at $1.2 \mu\text{m}$. (The latter may be pumped almost anywhere in the visible and even at $1.06 \mu\text{m}$). The energy level diagram for Cr^{4+} in a tetrahedral site is similar to that for Ni^{2+} in an octahedral site (see Fig. 1.3) and the lasing emission has been tentatively assigned to a transition from the lowest crystal-field split component of the ${}^3\text{T}_2$ state to the ${}^3\text{A}_2$ ground state in this system.⁷² The structured low-temperature spectrum shown in Fig. 5.6 becomes a broad band at room temperature and it peaks at different wavelengths around $1.1 \mu\text{m}$ depending on the excitation wavelength and on the Cr concentration (Fig. 5.8). Emission in this wavelength region, and the measured lifetime of $2.5 \mu\text{s}$ at room temperature, is difficult to reconcile with the known spectroscopic properties of Cr^{3+} ions in oxide crystals. The identification of the lasing centre in this material remains an interesting problem for further study. We note that similar laser action, with a tuning range of more than 300 nm and extending to beyond $1.2 \mu\text{m}$ in some cases, has recently been reported by Kaminski⁷⁴ in a range of Cr-doped oxide crystals. If indeed these results are due to Cr^{4+} then this ion may prove to be a worthwhile laser centre in its own right which can extend the range beyond that of Cr^{3+} in the infrared and new crystal hosts were sought which can stabilise this oxidation state. Some of the results are described in the next section.

5.5 Spectroscopic measurements of Cr^{4+} -doped media.

Although laser action in Cr-doped forsterite and YAG crystals is attributed to Cr^{4+} in a distorted tetrahedral site, a number of other materials with Cr^{4+} in tetrahedral sites have not exhibited stimulated emission at room temperature.⁷⁵ This may be due to low quantum efficiency in these media resulting from intraionic nonradiative decay processes and energy transfer to traps. To address this problem (in collaboration with the University of Belarus, Minsk) we have investigated the spectroscopic properties of different hosts containing Cr^{4+} ions in tetrahedral sites, namely Y_2SiO_5 (YSO), Gd_2SiO_5 (GSO), and $\text{Ca}_3(\text{VO}_4)_2$ (CVO). As shown in Fig. 5.9, the broadband luminescence from these materials at low temperatures was in the 1.1 - $1.7 \mu\text{m}$ region with peaks at about 1.25 , 1.32 , and $1.17 \mu\text{m}$ in YSO, GSO, and CVO, respectively, and was assigned to ${}^3\text{T}_2 \rightarrow {}^3\text{A}_2$ transitions on Cr^{4+} ions in tetrahedral sites (see Fig. 1.3). At least two types of the near infrared emitting centers were observed in YSO. The dominant strong absorption bands with peaks at about 16700 and 14000 cm^{-1} , weak absorption at about 1000 cm^{-1} and broad emission band with peak at 1250 nm are assigned to transitions on Cr^{4+} ions, substituting for the Si in distorted tetrahedral sites. The temperature dependence of two zero-phonon lines observed at 1148.7 nm and 1144.3 nm

$\text{Mg}_2\text{SiO}_4:\text{Cr}$

290 K

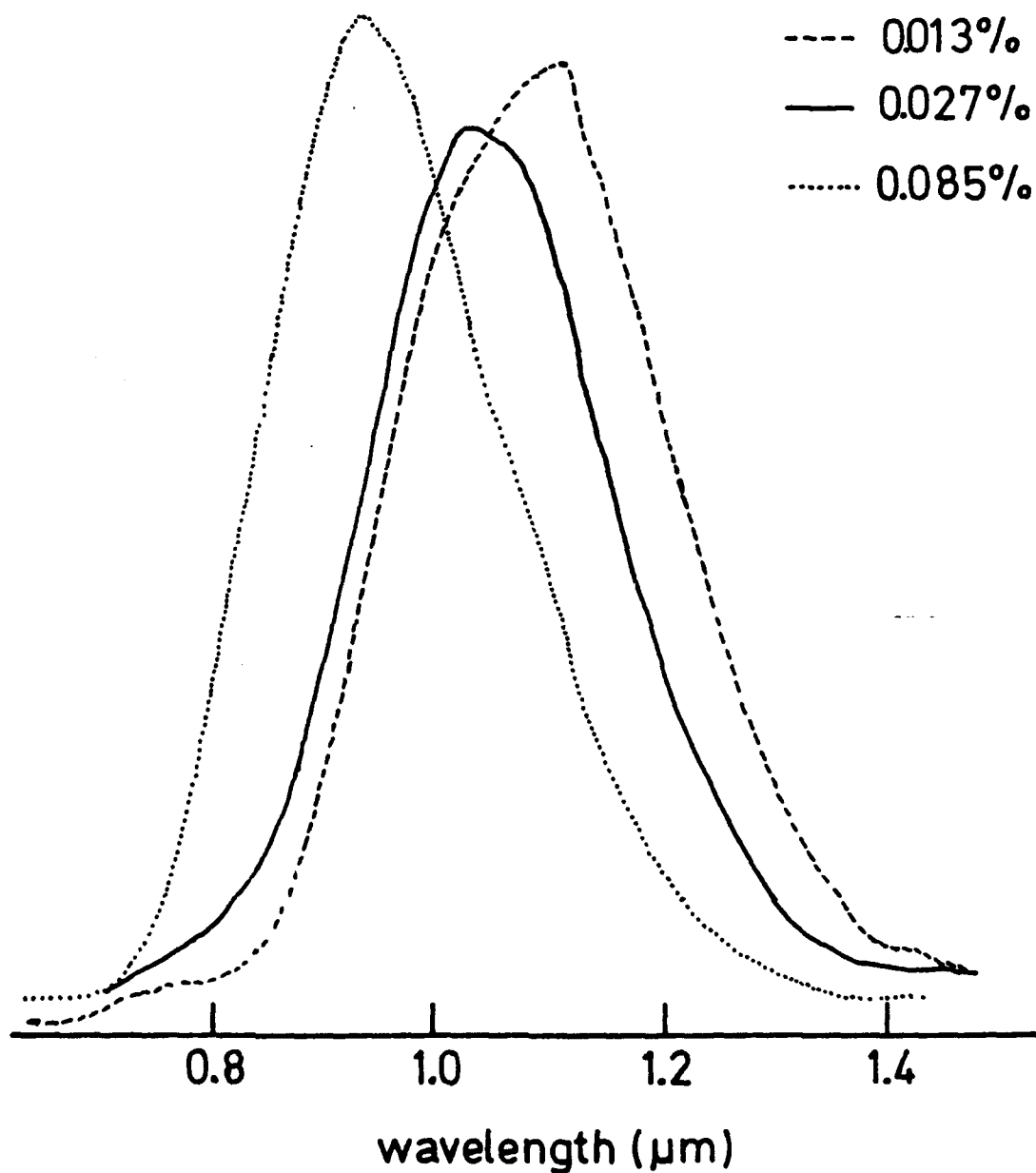


Figure 5.8. The near-infrared emission band in chromium-doped forsterite for different concentrations of chromium excited by an argon-ion laser at 290 K (all lines). Tunable laser operation has been obtained over about 75 nm centred on 1.2 μm (12).

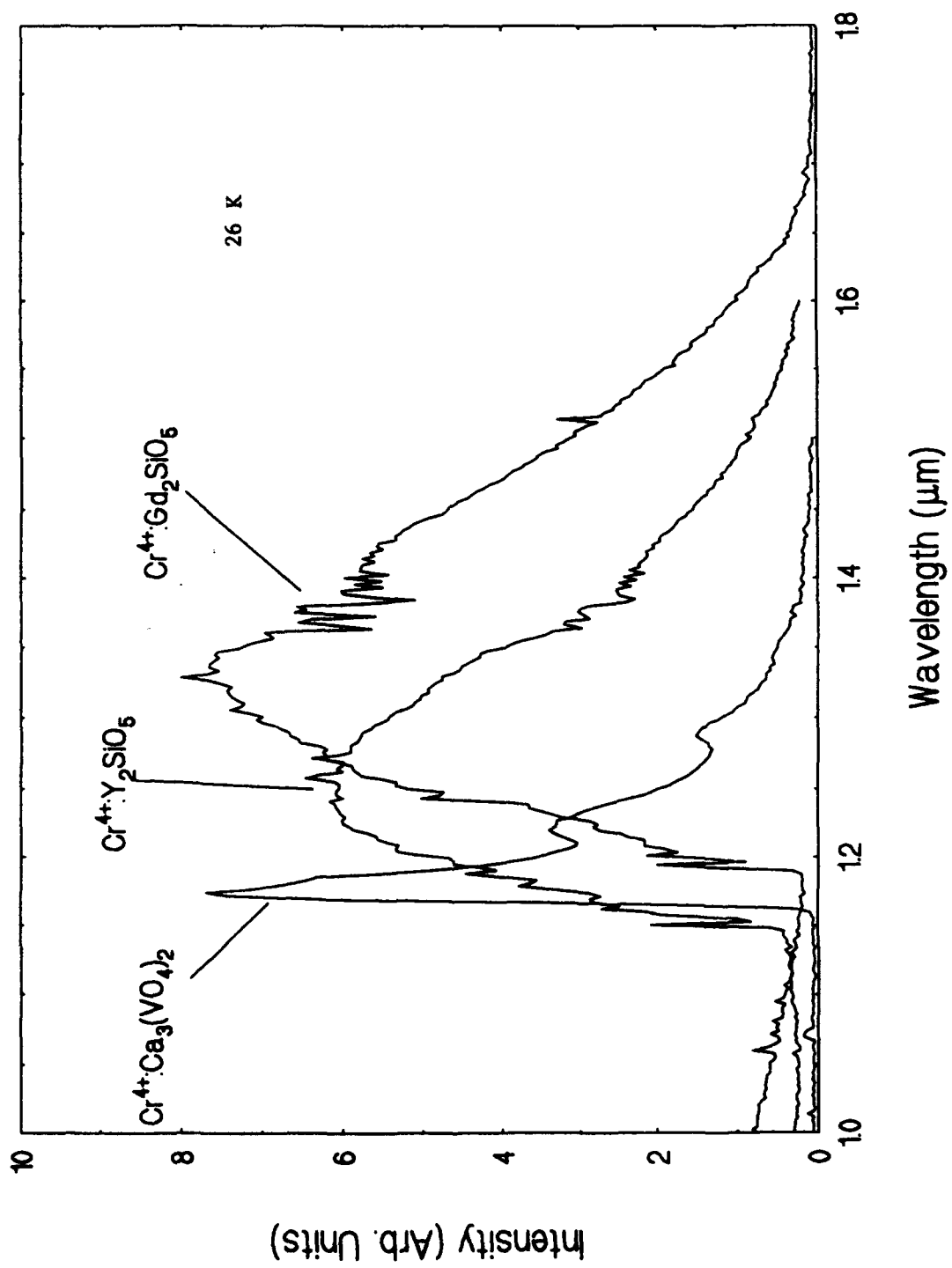


Figure 5.9. Broadband luminescence spectra of various Cr^{4+} -doped hosts at 26 K.

indicated the 33.5 cm^{-1} splitting in excited state of these centers. Fluorescence decay time excited by 578 nm pumping varied from $11.5 \mu\text{s}$ at 77 K to $0.9 \mu\text{s}$ at 300 K. A decreasing of emission intensity was observed with increasing temperature, providing evidence for strong non-radiative processes. Another type of emitting center in YSO had weak absorption bands at about 20500 and 13000 cm^{-1} and fluorescence band with peak at about $1.2 \mu\text{m}$. The emission lifetime at 77 K was found to be $5.2 \mu\text{s}$ and extremely strong temperature quenching of the fluorescence was observed for this center.

A broad near infrared emission band peaking at $1.32 \mu\text{m}$ was observed in GSO with a lifetime of $1.7 \mu\text{s}$ at 77 K. At room temperature the fluorescence intensity and lifetime was two orders of magnitude smaller than that at 77 K. The emission lifetime at low temperatures was shorter than that observed in forsterite and varied from $11.5 \mu\text{s}$ in YSO to $1.8 \mu\text{s}$ in GSO. The temperature dependence of the emission lifetime and of the integrated intensity (Fig. 5.10) were measured for these materials over a range of Cr^{4+} doping levels. The results indicated that intraionic nonradiative relaxation processes are strongly affecting the emission from the ${}^3\text{T}_2$ excited state of tetrahedral Cr^{4+} at room temperature.

In all of these materials, the integrated intensity in the emission band decreased by a factor of 15-20 on warming up to room temperature. The spectroscopy of Cr^{4+} -doped materials is still very poorly understood and much work remains to be done if this potential laser center is to be fully exploited.

5.6 Conclusion

Since interest was renewed in Cr-doped media by the achievement of laser action in alexandrite, and subsequently forsterite, many new Cr-doped media have been reported (see Table 1.1) and Cr^{4+} has been recognised as a new lasing ion. The results of our measurements on materials doped with either Cr^{3+} and Cr^{4+} ions (or both) have been reported in this chapter. Although many materials, containing Cr^{4+} ions in tetrahedral sites, have recently been explored, none have been found which a quantum efficiency at room temperature comparable to that obtained in forsterite. Interest in Cr^{3+} -doped materials has decreased since the commercialisation of the Ti:sapphire laser system.

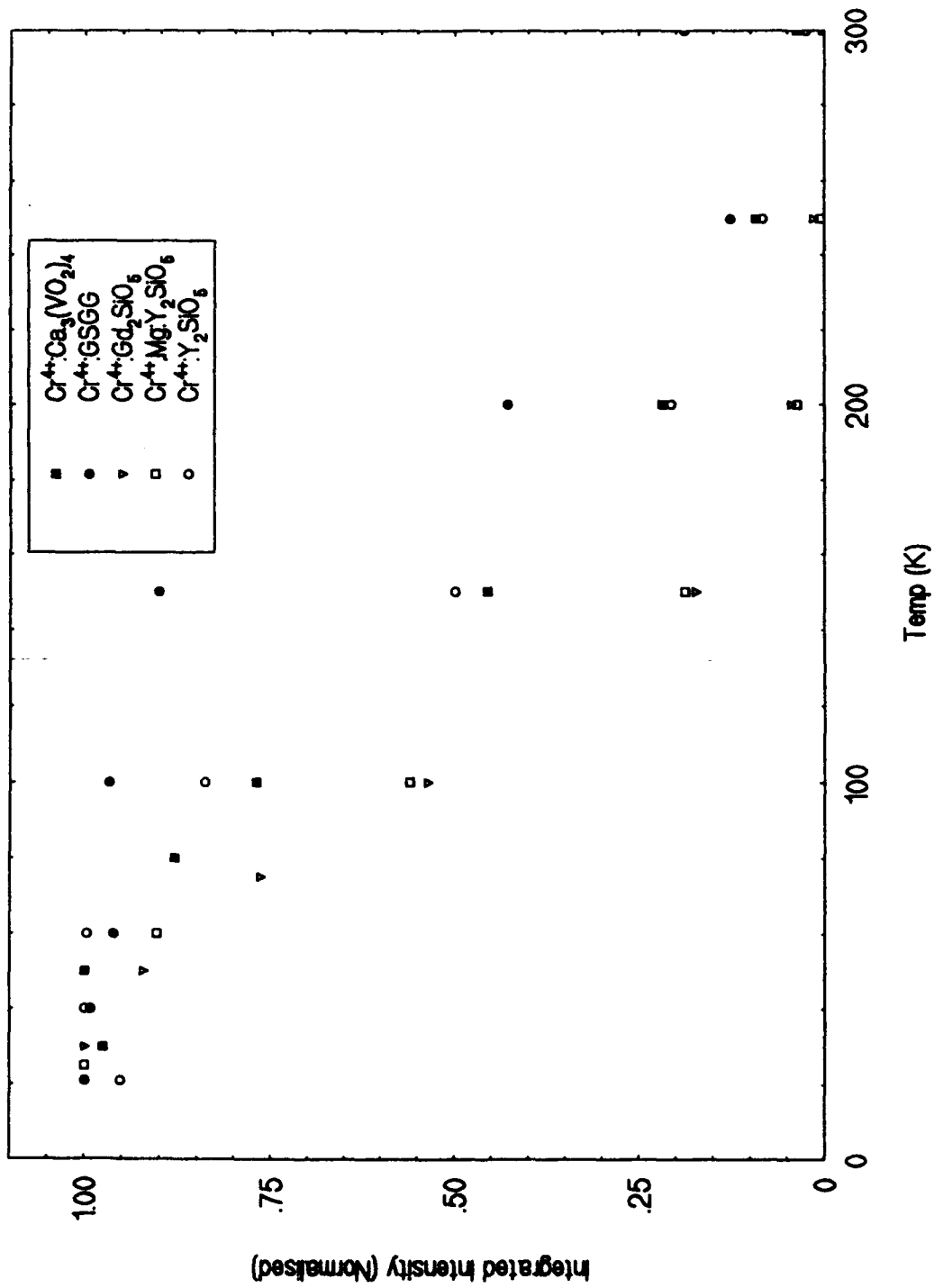


Figure 5.10. Temperature dependence of Cr^{4+} luminescence in various hosts.

CONCLUSION.

Although there are very few commercial laser systems based on TMI-doped materials, the data presented in this report suggests that many possible dopant-host combinations remain to be explored. Some novel behaviour for TMI in various host materials has been discovered in this study, e.g. emission from higher excited state in $\text{MgNb}_2\text{O}_6:\text{Co}^{2+}$, energy transfer from host material in $\text{BiGaO}_3:\text{Cr}^{3+}$, and anomalous lifetime of the ${}^1\text{T}_2$ state in $\text{MgNb}_2\text{O}_6:\text{Ni}^{2+}$ and $\text{ZnNb}_2\text{O}_6:\text{Ni}^{2+}$. The luminescence behaviour of the latter systems is very similar to that of several Ni-doped chlorides reported recently. In $\text{CsCdCl}_3:\text{Ni}^{2+}$, evidence is presented for a nonradiative pathway from the ${}^1\text{T}_2$ state direct to the ground state. Such processes are difficult to detect since they can only be observed easily when two emitting levels are connected by radiative and/or nonradiative transitions, a situation which rarely occurs for TMI centers. Thus very little is known about the nonradiative branching ratios involved in multiphonon relaxation from higher excited states. It is possible that multiphonon relaxation pathways which do not follow a "cascade" route of successive steps between adjacent levels are much more common in TMI systems, although very difficult to detect. $\text{MgNb}_2\text{O}_6:\text{Ni}^{2+}$ is an important material since it allows more detailed investigation of the excited state dynamics of such systems. This material also shows an unusually strong and sharp absorption from the ground state into the ${}^1\text{E}$ level. The reason for this effect may shed some light on the nature of the singlet-triplet mixing in Ni-doped materials. Both LiAl_5O_8 and ZnAl_2O_4 doped with Ni^{2+} show potential as tunable laser media, although ESA studies have yet to confirm this possibility.

This study has not uncovered an alternative to $\text{MgF}_2:\text{Co}^{2+}$, the only Co-doped commercial laser system, although some new possibilities based mainly on tetrahedrally-coordinated Co^{2+} ions and emission from higher excited states of octahedrally-coordinated systems have been explored. ESA and nonradiative relaxation effects are major potential drawbacks in all Co-doped materials but careful trawling of new materials may be a source of new laser media.

The growth of Cr-doped crystals has taken a new direction in recent years with the realisation that Cr^{4+} is also a lasing ion and with the identification and growth of crystalline hosts which can accept this ion in tetrahedral sites. The search continues also for new Cr^{3+} -doped media with high quantum efficiency in the ${}^4\text{T}_2 \rightarrow {}^4\text{A}_2$ transition at room temperature. Much work remains to be done to understand (i) why forsterite is the only host in which Cr^{4+} emits with significant quantum efficiency at room temperature, (ii) the unusual temperature dependence of the emission lifetime in this material, (iii) why Cr enters this host as Cr^{4+} in tetrahedral sites. Our studies of other Cr-doped silicates may provide answers to some of these questions.

The possibility of obtaining laser action in glasses doped with TMI was explored briefly, without success, early in the project. The most encouraging results were obtained with fluoride glasses doped with Co and Ni. Given the preference for randomly connected tetrahedral complexes in silicate glasses, and the ease with which Cr has been incorporated in tetrahedral sites in various crystalline silicates, it may yet be possible to fabricate glasses doped with Cr^{4+} ions which would have suitable properties for IR lasers. The potential of constructing fibre amplifiers in the 1.3- 1.5 μm region is an attractive possibility.

REFERENCES

1. B. Struve, G. Huber, I.A. Scherbakov, E.V. Zharikov, Appl. Phys. B 30, 117 (1983).
2. J. Drube, B. Struve, G. Huber, Opt. Comm. 50, 45 (1984).
3. S.T. Lai, M.L. Shand. J.A.P. 54, 5642 (1983)
4. J. Buchert, A. Katz, R.R. Alfano. IEEE J.O.E. 19, 1477 (1983)
5. V. Petricevic, S.K. Gayen, R.R. Alfano, K. Yamagishi, H. Anzai, Y. Yamaguchi. Appl. Phys. Lett 52, 1040 (1988).
6. K. Peterman, G. Huber, J. Lumin. 31/32, 71 (1984)
7. B. Viana, A.M. Lejus, B. Vivien, V. Poncon, G. Boulon. J. Sol. State Chem. 71, 77 (1987).
8. C. Marco de Lucas, F. Rodriguez, J.M. dance, M. Moreno, and A. Tressaud, J. Lumin. 48/49, 553 (1991)
9. S.T. Lai, B.H.T. Chai, M. Long, M.D. Shinn. IEEE J.O.E. 24, 1922 (1988).
10. U. Brauch, U. Durr, Opt. Lett. 9, 441 (1984)
11. S.A. Payne, L.L. Chase, H.W. Newkirk, L.K. Smith, W.F. Krupke. IEEE J.O.E. 24 (11), 2243 (1988).
12. L.J. Andrews, A. Lempicki, B.C. McCollum, J.C. Giunta, R.H. Bartram, J.F. Dolan. Phys. Rev. B34, 2735 (1986).
13. R. Knockenmuss, Ch. Rever, M.V. Rajasekharn, H.U. Gudel. J. Chem. Phys. 85, 4280 (1986).
14. S.A. Payne, L.L. Chase, W.F. Krupke. J. Chem. Phys. 86 3455 (1987)
15. P.F. Moulton, A. Mooradian. Appl. Phys. Lett. 35, 838 (1979)
16. L.F. Johnson, H.J. Guggenheim, B. Bahnck, A.M. Johnson. Opt. Lett. 8, 371 (1983)
17. M.V. Iverson, W.A. Sibley, J. Lumin. 20, 311 (1979).
18. R. Moncorge, T. Benyattou. Phys. Rev. B37, 9186 (1988) and refs. therein.
19. P.F. Moulton. IEEE J.O.E. 18, 1185 (1982)
20. T. Benyattou, R. Moncorge, J.M. Breteau, F. Auzel. Cryst. Latt. Def. and Amorph. Lat. 15, 157 (1987).
21. R. Moncorge, T. Benyattou, D. Vivien, A.M. Lejus. J. Lumin. 35, 199 (1986)
22. R. Moncorge, J. Thery, D. Vivien, J. Lumin. 43, 167 (1989)
23. U. Oetliker, M.J. Riley, P.S. May and H.U. Gudel. Coord. Chem. Rev. 111, 125 (1991).
24. H. Manaa, R. Moncorge, Opt. Quant. Elect. 22, S219 (1990).
25. P.S. May and H.U. Gudel, Chem. Phys. Lett. 164, 612 (1989).
26. R. Alcala, J. Gonzalez, B. Villacampa, P.J. Alonso, J. Lumin. 48/49, 569 (1991)
27. P.S. May and H.U. Gudel, J. Lumin. 46, 277 (1990).

28. J. Koetke, G. Huber, and K. Petermann, J. Lumin., 48/49, 564 (1991).
29. P.S. May and H.U. Gudel, J. Chem. Phys. 95, 6343 (1991).
30. P.F. Moulton, J. Opt. Soc. Am. B3(1), 125 (1986)
31. A. Sanchez, A.J. Strauss, R.L. Aggarwal, R.E. Fahey, IEEE J.O.E. 24, 995 (1988) and refs therein.
32. R. Moncorge, G. Boulon, D. Vivien, A.M. Lejus, R. Collongues, V. and K. Djevahirdjian, R. Cagnard, IEEE J.O.E. 24, 1049 (1988)
33. U. Brauch, U.Durr, W. Knierim, and C. Shiller. TSSL conference La Jolla Ca (USA) June 1984. Springer-Verlag 47, 20 (1985).
34. D. Welford and P.F. Moulton, Opt. Lett. 13, 975 (1988)
35. W.Künzel, W.Knierim, and U. Dürr, Opt. Comm., 36, 383 (1981).
36. M.D. Sturge, Phys. Rev. B8, 6 (1973)
37. P.F. Moulton, IEEE J. Quant. Elec. QE-21, 1582 (1986).
38. L.F. Johnson, H.J. Guggenheim, J.A.P. 38, 4837 (1967).
39. R. Moncorge, T. Benyattou. Phys. Rev. B37, 9177 (1988).
40. U. Brauch, U.Durr, Opt. Comm. 55, 35 (1985).
41. W. Knierim, A. Honold, U. Brauch, U.Durr, J. Opt. Soc. Am. B3, 119 (1986).
42. P.F. Moulton, Laser Focus. Aug. 1987, p.56.
43. Y. Tanabe, S. Sugano, H.Kamimura in Multiplets of transition Metal Ions in Crystals. ed. Acad. Press N.Y. (1970).
44. F. Auzel, Luminescence of Inorganic Solids, ed. B. Di Bartolo (Plenum Press, new York) 1978.
45. R.M. Bartram, J.C. Charpie, L.J. Andrews, A. Lempicki. Phys. Rev. B34, 2741 (1986) and refs therein.
46. R. Reisfeld and C.K. Jorgensen, in Handbook on the Physics and Chemistry of Rare Earths, edited by K.A. Gschneider and L. Eyring (Elsevier, New York, 1987) 9, p.1.
47. J.M.F. van Dijk and M.F.H. Schuurmans, J.Chem.Phys. 78, 5317 (1983).
48. B. Henderson and G.F. Imbusch, Optical Spectroscopy of Inorganic Solids, (Clarendon Press, Oxford, 1989).
49. S.A. Payne, Phy. Rev. B41, 6109 (1990).
50. S.M. Jacobsen and H.U. Gudel, J. Lumin. 43, 125 (1989).
51. W.E. Vehse, K.H. Lee, S.I. Yun and W.A.Sibley, J. Lumin., 10, 149 (1975)
52. J.F. Donegan, F.J.Bergin, T.J. Glynn, G.F. Imbusch, J.P. Remeika, J.Lumin. 35, 57 (1986).
53. Radiationless Processes, Nato Advanced Study Institutes Series B-62; ed. B. DiBartolo (Plenum, New York, 1979).

54. C.W. Struck, W.H. Fonger, J. Lumin. 10, 1 (1975).
55. Y. Suzuki, W. A. Sibley, O.H. El Bayaumi, T. M. Roberts, and B. Bendon, Phys. Rev. B35, 4472 (1987).
56. L.J. Andrews et al, Report DOE/ER/04996-4, U.S. Department of Energy (1983).
57. S. Hampshire, R.A.L. Drew, K.H. Jack, Phys. Chem. Glasses 26, 182 (1985).
58. J.F. Donegan, F.J. Bergin, G.F. Imbusch, and J.P. Remeika, J. Lumin. 31/32, 378 (1984).
59. R.J. Wyckoff, Crystal Structures Vol. III (Interscience, New York, 1965) p. 362.
60. Pappalardo, D.L. Wood, R.C. Linares, J.Chem.Phys. 35, 2041 (1961)
61. W. Jia et al, Phys. Rev. B43, 5234 (1991).
62. G. walker and T.J. Glynn, J. Lumin. 54, 131 (1992) 131.
63. H. Rager, S. Hosaya, and G. Weiser, Phys. Chem. Minerals 15, 383 (1988).
64. J.C. Walling, O.G. Peterson, H.P. Jenssen, R.C.Morris, and E. Wayne O'Dell, IEEE J. Quantum Electron. QE-16, 1302 (1980).
65. J.M. Moreau, C. Michel, R. Gerson, and W.J. James, J. Phys. Chem. Solids 32, 1315 (1971)
66. A.S. Barker, Jr. and R. Loudon, Phys. Rev. 158, 433 (1967)
67. S.M. Healy, C.J. Donnelly, T.J. Glynn, G.F. Imbusch and G.P. Morgan, J. Lumin. 44, 65 (1989).
68. A.M. Glass, J.Chem. Phys. 50, 1501 (1969)
69. C.J. Donnelly, S.M. Healy, T.J. Glynn, G.F. Imbusch, and G.P. Morgan, J. Lumin. 42, 119 (1988).
70. A.A. Kaminskii, Laser Crystals: their physics and properties, Springer-verlag (1990).
71. Petricevic, S.G. Gayen, and R.R. Alfano, Appl. Phys. Lett. 53, 2590 (1988) Also Opt. Lett. 14, 612 (1989).
72. H.R. Verdun, L.M. Thomas, D.M. Androuskas, T.McCollum and A. Pinto, Appl. Phys. Lett. 53, 2593 (1989).
73. H. Rager, Phys. Chem. Minerals 1, 371 (1977).
74. A. Kaminskii, in Proc. International School on Excited States of Transition Elements (Poland, 1988) World Scientific 669 (1988).
75. L.D. Merkle et al, Opt. Mater. 1 (1992) 91.

FLN STUDY OF $\text{LiGa}_5\text{O}_8:\text{Co}^{2+}$

J.F. DONEGAN, T.J. GLYNN and G.F. IMBUSCH

Department of Physics, University College, Galway, Ireland

Absorption, luminescence, and lifetime measurements have been carried out on $\text{LiGa}_5\text{O}_8:\text{Co}^{2+}$. The emission consists of three broad bands, peaking at 675 nm, 950 nm, and 1.2 μm , which are assigned to spin-allowed transitions between the ${}^4\text{T}_1({}^4\text{P})$ state and lower crystal field levels of the Co^{2+} ions in tetrahedral sites. The radiative decay rate, common to all the emission, is ~ 200 ns, even up to room temperature. FLN techniques were used to study the zero-phonon line of the visible transition, which occurs at 15157 cm^{-1} . These studies reveal fine structure in the inhomogeneously broadened line and a ground-state splitting of $\sim 20\text{ cm}^{-1}$, indicating that the cobalt ions occupy rather distorted tetrahedral sites.

1. Introduction

The Co^{2+} ion has been studied as a dopant ion in many host materials, in which it can occupy sites of octahedral symmetry, for example in MgF_2 [1], or sites of tetrahedral symmetry, for example in ZnO [2]. However, given a choice of sites this ion shows a strong preference for the tetrahedral site [3,4]. LiGa_5O_8 contains both types of site but absorption, luminescence, and lifetime data [5] indicate that the cobalt substitutes for Ga^{3+} ions as Co^{2+} and only in tetrahedral sites. We find no spectroscopic evidence for cobalt ions in any valence state in octahedral sites. The dopant cobalt shows two zones of concentration in this material. Elec-

tron beam microprobe measurements on one sample gave 0.5% for the dark blue core region of the sample and 0.12% in the pale blue outer edges [6].

2. Spectroscopic measurements

By comparison with the absorption spectra from dopant Co^{2+} ions in tetrahedral sites in other materials [3,4] we have assigned the three main luminescence bands from this material – at 675 nm, 950 nm, and 1200 nm – to transitions from the ${}^4\text{T}_1({}^4\text{P})$ level to ${}^4\text{A}_2({}^4\text{F})$, ${}^4\text{T}_2({}^4\text{F})$, and ${}^4\text{T}_1({}^4\text{F})$, respectively. A summary of the relevant spectra is shown in fig. 1. The visible emission

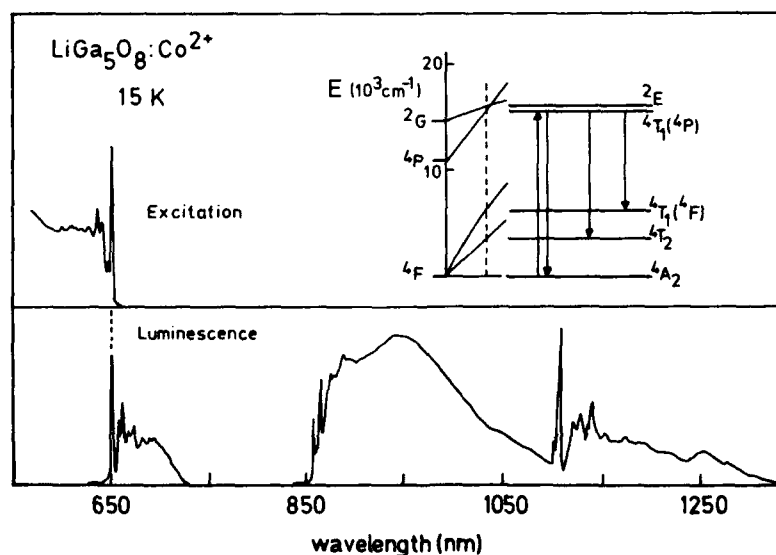


Fig. 1. Energy level structure along with excitation and luminescence spectra of Co^{2+} ions in tetrahedral sites in LiGa_5O_8 at 15 K.

nally, if the laser frequency coincides with transitions from the two components of the ground state to the lower level of the ${}^4\text{T}_1({}^4\text{P})$ state, situations illustrated in fig. 3(c) and (d), then we would expect to obtain a true FLN signal as we are resonantly exciting the lowest level of the excited state. The expected emission in this case is a pair of lines equally spaced from the exciting laser frequency. Again referring to fig. 2 we observe that the emission shown in spectra (f) and (g) does in fact consist of a pair of sharp lines, which we interpret as transitions to the two components of the ground ${}^4\text{A}_2({}^4\text{F})$ state. The separation between the laser frequency and one of these components gives the ground state splitting which we measure to be approximately 20 cm^{-1} in this case. The separation between the exciting laser and the rather broad emission in spectrum (a) in fig. 2 should by analogy give the excited state splitting of the ${}^4\text{T}_1({}^4\text{P})$ level. This splitting is measured to be $\sim 35\text{ cm}^{-1}$. Some of the sideband features also became much narrower – 3 cm^{-1} – when the luminescence was excited by the laser within the zero-phonon line.

4. Conclusion

FLN experiments show an amount of fine structure in the inhomogeneously broadened ${}^4\text{T}_1({}^4\text{P})$ – ${}^4\text{A}_2({}^4\text{F})$ luminescence transition in $\text{LiGa}_5\text{O}_8:\text{Co}^{2+}$ and reveal a ground state splitting of approximately 20 cm^{-1} . This is a large value for the ${}^4\text{A}_2({}^4\text{F})$ level, indicating that the distortion of the tetrahedral site is large, due perhaps to local charge compensation effects. The short lifetime of

the excited state makes it unsuitable for flashlamp pumping, but suggests a potentially high gain in the infrared depending on the branching ratio between the various transitions. These data suggest that similar systems based on Co^{2+} ions in tetrahedral coordination may find application as tunable solid-state laser media in the near infrared.

Acknowledgements

Research sponsored by the Air Force Office of Scientific Research, Air Force Systems Command, USAF, under Grant Number AFOSR 88-0355. The US Government is authorised to reproduce and distribute reprints for Governmental purposes notwithstanding any copyright notation thereon.

References

- [1] L.F. Johnson, R.E. Dietz and H.J. Guggenheim, *Appl. Phys. Lett.* 5 (1964) 21.
- [2] R. Pappalardo, D.L. Wood and R.C. Linares Jr., *J. Chem. Phys.* 35 (1961) 2041.
- [3] D.L. Wood and J.P. Remeika, *J. Chem. Phys.* 46 (1967) 3595.
- [4] J. Ferguson, D.L. Wood and L.C. Van Uitert, *J. Chem. Phys.* 51 (1969) 2904.
- [5] J.F. Donegan, F.J. Bergin, G.F. Imbusch and J.P. Remeika, *J. Lumin.* 31 & 32 (1984) 278.
- [6] R.M. MacFarlane and J.C. Vial, *Phys. Rev.* B34 (1986) 1.

Optical and magnetic-circular-dichroism—optically-detected-magnetic-resonance study of the Co^{2+} ion in LiGa_5O_8

J. F. Donegan

*Department of Experimental Physics, University College, Galway, Ireland;
Optronics Ireland Research Centre and Department of Pure and Applied Physics, Trinity College, Dublin 2, Ireland;
and Sherman Fairchild Laboratory and Physics Department, Lehigh University, Bethlehem, Pennsylvania 18015*

F. G. Anderson

*Department of Experimental Physics, University College, Galway, Ireland
and Sherman Fairchild Laboratory and Physics Department, Lehigh University, Bethlehem, Pennsylvania 18015*

F. J. Bergin, T. J. Glynn, and G. F. Imbusch

*Department of Experimental Physics, University College, Galway, Ireland
(Received 19 June 1991)*

Optical and magnetic-circular-dichroism—optically-detected-magnetic-resonance studies have been carried out on Co-doped LiGa_5O_8 . The Co ions are found to be predominantly in the $2+$ charge state and to substitute for tetrahedrally coordinated Ga^{3+} in the LiGa_5O_8 lattice, in sites which are shown to have C_3 point-group symmetry. The strong absorption bands from the ground state ${}^4A_2({}^4F)$ to the excited states ${}^4T_1({}^4P)$ and ${}^4T_1({}^4F)$ are each split by the low-symmetry C_3 field. A combination of the low-symmetry field and spin-orbit coupling is responsible for the ground-state splitting of $19.5 \pm 0.5 \text{ cm}^{-1}$ observed by fluorescence line narrowing. Strong broadband luminescence is observed from the ${}^4T_1({}^4P)$ level to three lower levels, ${}^4A_2({}^4F)$, ${}^4T_2({}^4F)$, and ${}^4T_1({}^4F)$, with a lifetime that is constant at 200 ns from 10 K up to room temperature. The optically-detected magnetic-resonance studies show that the Co^{2+} ions are in sites which have axial symmetry along $\langle 111 \rangle$ -type axes of the unit cell, indicative of the C_3 symmetry present in these substitutional sites. We give a detailed crystal-field model for the Co^{2+} ion in the C_3 site in LiGa_5O_8 and deduce the crystal-field parameters from our experimental data.

I. INTRODUCTION AND BACKGROUND

When cobalt (Co) is added as a dopant to wide band-gap oxide materials, they acquire a characteristic color due to electronic transitions on the Co ions in the visible region of the spectrum. The cobalt ions are generally found in the $2+$ and $3+$ charge states in these oxide hosts. In 1961, Pappalardo, Wood, and Linares¹ carried out a study of the spectroscopic properties of cobalt in a number of oxide crystals. They investigated cobalt doping of MgO and ZnO , which offer full octahedral and tetrahedral symmetry for the dopant Co ions, respectively. These are therefore ideal test systems to establish the spectroscopic properties of dopant Co ions in oxide materials. The simplicity of the observed spectra allowed Pappalardo *et al.*¹ to perform a detailed crystal-field analysis of the spectra. These researchers also carried out investigations of cobalt-doped spinel (MgAl_2O_4) and YAG ($\text{Y}_3\text{Al}_5\text{O}_{12}$), each of which offer both tetrahedral and octahedral environments for the dopant Co ions. On the basis of the work in $\text{MgO}:\text{Co}^{2+}$ and $\text{ZnO}:\text{Co}^{2+}$, they found that their spinel and YAG samples were dominated by Co^{2+} spectra and that, given a choice, the Co^{2+} ions greatly preferred tetrahedral to octahedral coordination in these materials. A subsequent study of Co absorption spectra in garnet hosts was carried out by Wood and Remeika² in 1967. The observed spectra were ascribed to

Co^{2+} and Co^{3+} ions, mainly in distorted tetrahedral environments. The tetrahedral Co^{3+} spectrum observed in the garnet material YAG is dominated by a broad double-peaked band centered near 9000 cm^{-1} . On the other hand, the tetrahedral Co^{2+} spectrum in YAG shows three absorption regions. The strongest absorption occurs in the visible peaking near 16000 cm^{-1} , giving the YAG:Co samples a characteristic blue color, and two absorption bands occur in the near infrared, peaking at 7100 and 4700 cm^{-1} .

The material LiGa_5O_8 crystallizes with the spinel (MgAl_2O_4) structure, which is adopted by a large number of compounds whose general formula is XY_2O_4 . In general, two types of spinel are distinguished: "normal" and "inverse," and the cube in Fig. 1 represents the unit cell of normal spinel. For convenience, the cell is divided into octants, and the arrangements of ions in two of the octants are shown. These arrangements are repeated in alternate octants. The octahedral and tetrahedral sites may be distinguished in this figure. Whereas in normal spinel the octahedral and tetrahedral sites are occupied by trivalent and divalent ions, respectively, in inverse spinel one-half of the trivalent ions occupy tetrahedral sites while the other half, together with the divalent ions, occupy octahedral sites, and the structure can be represented by the formula $\text{Y}(\text{XY})\text{O}_4$.

The LiGa_5O_8 arrangement is a variation of the inverse

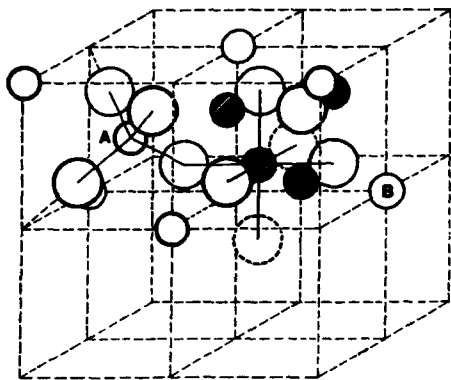


FIG. 1. Schematic diagram of the unit cell of normal spinel (MgAl_2O_4). For clarity, only two octants of the unit cell are shown. The large open circles are the oxygen ions, the small open circles are the tetrahedrally coordinated ions, and the hatched circles are the octahedrally coordinated ions. Atoms A and B in the figure are in tetrahedrally coordinated environments.

spinel structure and contains 4 formula units in the cubic cell shown in Fig. 1. The monovalent Li^+ ions and three-fifths of the Ga^{3+} ions are distributed among the octahedral sites in an ordered manner so that each row of octahedral ions in a $\langle 110 \rangle$ -type direction contains a lithium ion in every fourth position.³ This distribution of Li ions results in the arrangement shown in Fig. 2 for the second-nearest-neighbor shell of cations about a gallium ion in the tetrahedrally coordinated site. The nearest-neighbor oxygen ions are not shown. The Li ions are arranged symmetrically about the $[1\bar{1}1]$ direction of the cell. This arrangement of the Li ions means that the site symmetry for the tetrahedrally coordinated Ga^{3+} ions is reduced from T_d to C_3 , and, as we will see later, the

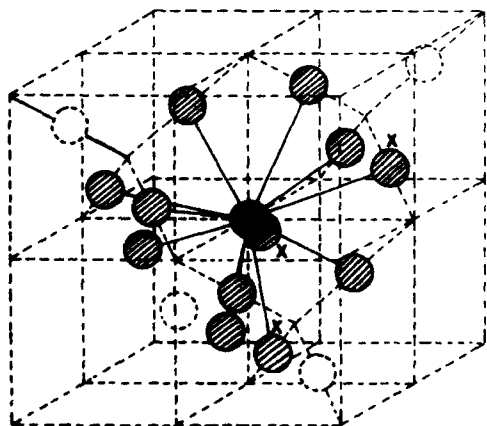


FIG. 2. Environment of the Co^{2+} ion in LiGa_5O_8 showing the shell of second-nearest-neighbor cations. This cube in this figure is shifted by a distance equal to half the cube edge with respect to the cube in Fig. 1 (so that the atom marked B in Fig. 1 is now at the center of the cell) and the oxygen nearest-neighbor ions are omitted for clarity. The solid circle is the Co^{2+} ion and the hatched circles are the octahedrally coordinated second-nearest-neighbor ions. The circles marked X are the Li^+ ions. The C_3 symmetry axis for the Co^{2+} ion in the center of the shell is the $[1\bar{1}1]$ direction.

Co^{2+} ions substitute for Ga^{3+} at these sites in LiGa_5O_8 . There are four possible inequivalent Co^{2+} sites in the unit cell, with C_3 axes along $\langle 111 \rangle$ -type directions. The crystal structure of LiGa_5O_8 has been described in detail by Gorter.⁴

In the past, extensive optical spectroscopic studies have been carried out on Cr^{3+} , Mn^{4+} , Fe^{3+} , and Ni^{2+} ions in LiGa_5O_8 .⁵⁻⁹ In this study we have combined optical and magnetic-circular-dichroism-optically-detected-magnetic-resonance (MCD-ODMR) spectroscopies to obtain a detailed account of the electronic structure and environment of the Co^{2+} ion in LiGa_5O_8 . The experimental results are consistent with the C_3 site symmetry expected for substitutional Co^{2+} in the tetrahedrally coordinated sites in this material. A crystal-field model is developed for the Co^{2+} ion in LiGa_5O_8 , and values for the crystal-field parameters are derived from the data.

II. EXPERIMENTAL DETAILS

The luminescence and excitation measurements were carried out in an Air-Products flow cryostat with temperatures in the range 10–300 K. An Aviv spectrophotometer was used for the absorption experiments along with a cold-finger cryostat with liquid- N_2 cooling. For the luminescence work, an Ar^+ laser with 100-mW power at 514.5 nm was employed. The excitation spectra were recorded using a cw dye laser with DCM or RG6 as the active dye medium. Both photomultipliers (with S20 and GaAs photocathodes) and a liquid- N_2 -cooled Ge detector were used to monitor the light signals.

The MCD and ODMR experiments are illustrated in Fig. 3. In this illustrative example, the ground and excit-

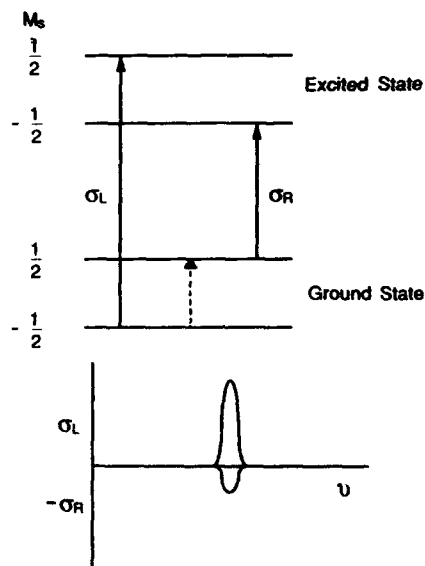


FIG. 3. An illustrative example of MCD with the ground and excited states both described by $S = \frac{1}{2}$. The lower Zeeman level in the ground state is more heavily populated than the upper state at low temperature, giving rise to a MCD signal. The ODMR transition in the ground state is indicated by a dashed line.

ed states are spin doublets, and these are each split into two by the magnetic field. The two circularly polarized absorption transition, σ_L and σ_R , are shown. These are transitions in which the light travels along the direction of the magnetic field. The oscillator strength of the two transitions are equal, but the absorption strength will depend on the populations in the ground-state sublevels. In this case, where there is a greater population in the lower level, in accordance with the Boltzmann formula, then σ_L will be greater than σ_R and the MCD signal, which is proportional to $(\sigma_L - \sigma_R)$, will be nonzero.

If now the sample is irradiated with microwave power at a frequency corresponding to the Zeeman splitting of the ground state, this will tend to equalize the populations in the two levels and there will be a decrease in the MCD signal. Thus, the ground-state resonance condition shows up as a change in the optical signal and this constitutes the optically-detected-magnetic-resonance signal.

The MCD-ODMR experiments were carried out at 1.6 K in an Oxford Instruments SM-3 superconducting magnet cryostat. The sample was mounted at the center of a 35-GHz TE_{011} microwave cavity having optical access. A Hinds SM-3 quartz modulator produced alternating left and right circularly polarized light at 50.3 kHz. The MCD signals were detected using both Si and Ge detectors combined with standard lock-in techniques. For the ODMR experiments, ~ 50 mW of microwave power was introduced into the cavity. For the case in which the absorption coefficients σ_L and σ_R are small, the MCD signal is given by

$$\text{MCD} = (\sigma_L - \sigma_R) \propto (I_R - I_L), \quad (1)$$

where I_L and I_R are the transmitted intensities for left and right circularly polarized light.

The samples of LiGa_5O_8 used in this study were grown by the flux method, and the dopant cobalt ions exhibit two zones of concentration in the material: a deep blue core and an outer pale blue region. Electron microprobe measurements of the cobalt concentration in one sample gave 0.5% in the core and 0.12% in the pale area.¹⁰ All measurements were carried out on samples cut from the lightly doped region. For the magnetic resonance experiments a small sample (dimensions 1 mm \times 1 mm \times 1.5 mm) was cut so that it could be positioned in the microwave cavity with the magnetic field in the $(01\bar{1})$ plane.

III. EXPERIMENTAL RESULTS

The $\text{LiGa}_5\text{O}_8:\text{Co}^{2+}$ system shows two regions of strong absorption, and their spectra recorded at 85 K are shown in Fig. 4. These spectra show a very strong similarity to those of Co^{2+} ions in tetrahedrally coordinated environments in $\text{Y}_3\text{Al}_5\text{O}_{12}$ and ZnAl_2O_4 .^{2,11} A Tanabe-Sugano energy level diagram for the lowest energy levels of a d^7 ion in a tetrahedral crystal field is also given in Fig. 4, and we assign the visible absorption band to the ${}^4A_2({}^4F) \rightarrow {}^4T_1({}^4P)$ transition and the infrared band to the ${}^4A_2({}^4F) \rightarrow {}^4T_1({}^4F)$ transition. A third absorption transition due to the ${}^4A_2({}^4F) \rightarrow {}^4T_2({}^4F)$ transition, expected to lie in the region of 4000 cm^{-1} , could not be detected even in samples with nominal Co concentration of 1%. The weak band in Fig. 4 with a zero-phonon line at 13580 cm^{-1} is tentatively assigned to Co^{3+} in the octahedrally coordinated site in LiGa_5O_8 by comparison with previous studies of Co-doped $\text{Y}_3\text{Al}_5\text{O}_{12}$.²

On inspection of Fig. 4 we see that both absorption bands are split; the band in the visible has two broad components at 15400 and 16600 cm^{-1} , while the band in

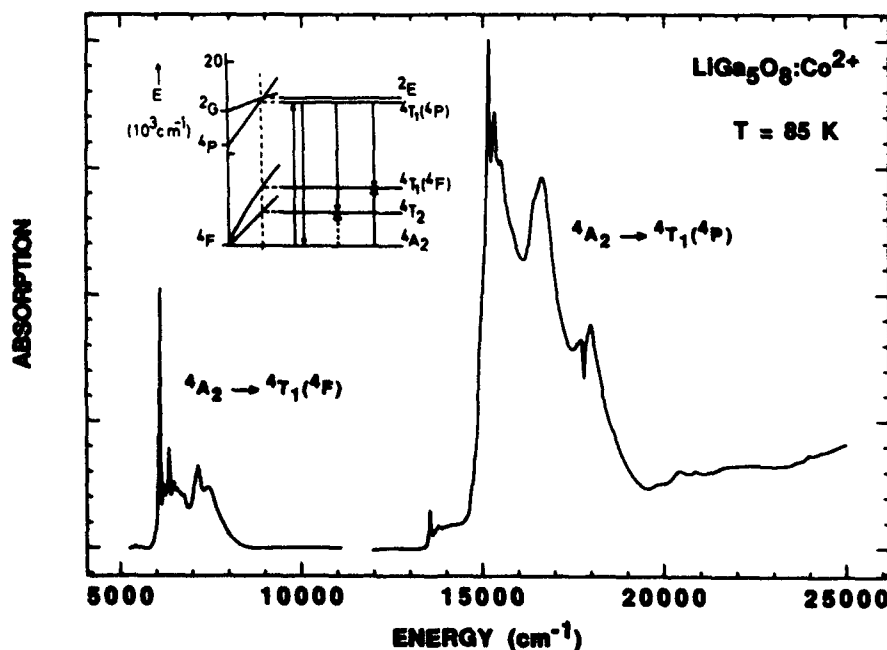


FIG. 4. The absorption spectrum of $\text{LiGa}_5\text{O}_8:\text{Co}^{2+}$ recorded at 85 K showing the ${}^4A_2({}^4F) \rightarrow {}^4T_1({}^4P)$ and the ${}^4A_2({}^4F) \rightarrow {}^4T_1({}^4F)$ transitions. The inset shows a Tanabe-Sugano energy-level scheme for Co^{2+} in LiGa_5O_8 . The absorption transitions are indicated on the energy-level scheme.

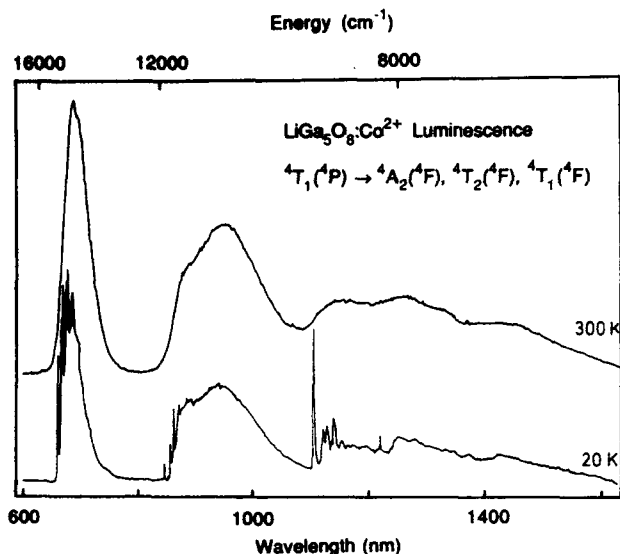


FIG. 5. The luminescence spectrum of $\text{LiGa}_5\text{O}_8:\text{Co}^{2+}$ recorded at 20 K and room temperature showing the three luminescence transitions. An Ar^+ laser with 100-mW power was used for excitation. The luminescence transitions are indicated on the energy-level scheme in Fig. 4.

the near infrared has two broad components at 7210 and 6300 cm^{-1} . A similar splitting was observed by Wood and Remeika in the corresponding Co^{2+} spectra in $\text{Y}_3\text{Al}_5\text{O}_{12}$.² There is some sharp-line structure evident in both transitions, which makes it difficult to unambiguously distinguish between electronic and vibrational fine structure.

Using Ar^+ laser excitation at 514.5 nm, three luminescence transitions are observed and the complete luminescence spectrum at 20 K and room temperature are shown in Fig. 5. This spectrum was recorded using a Ge detector and is not corrected for the system response. We note that, as the Ge detector has a poor response in the visible,

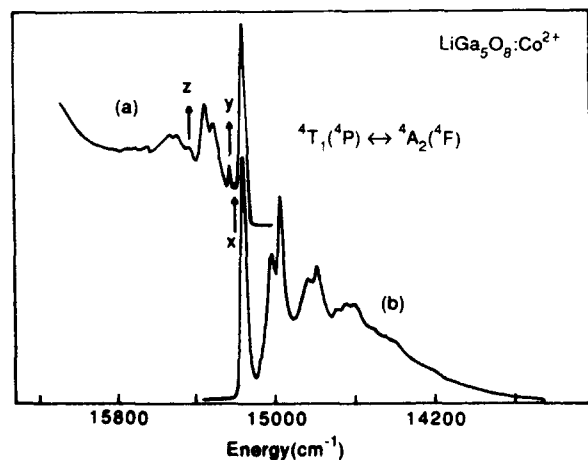


FIG. 6. (a) The excitation spectrum of all three luminescence transitions shown in Fig. 5 recorded at 15 K and (b) the ${}^4T_1({}^4P) \rightarrow {}^4A_2({}^4F)$ luminescence transition recorded at 15 K. These two spectra are clearly mirror images of one another apart from the features marked *x*, *y*, and *z* in the figure.

TABLE I. Comparison of the sideband features (in cm^{-1}) in luminescence and excitation of the ${}^4A_2({}^4F) \leftrightarrow {}^4T_1({}^4P)$ transitions for Co^{2+} ions in LiGa_5O_8 .

Luminescence	Excitation
	46
	63
149	146
185	188
	277
333	340
374	378
474	460
520	507
564	565
630	626
657	
714	704
768	

the first luminescence transition in the red is much stronger than the other two. The zero-phonon line of the first luminescence transition at 15 157 cm^{-1} recorded at 15 K coincides with the first sharp peak of the visible absorption band in Fig. 4. All three luminescence bands of Fig. 5 are found to have the same excitation spectrum [recorded at 15 K and shown in Fig. 6(a)] and the same lifetime. Therefore, these are assigned to transitions originating on the same ${}^4T_1({}^4P)$ level. The red luminescence is the ${}^4T_1({}^4P) \rightarrow {}^4A_2({}^4F)$ transition (see the energy-level diagram in Fig. 4) while the two near-infrared luminescence transitions in Fig. 5 are assigned to the

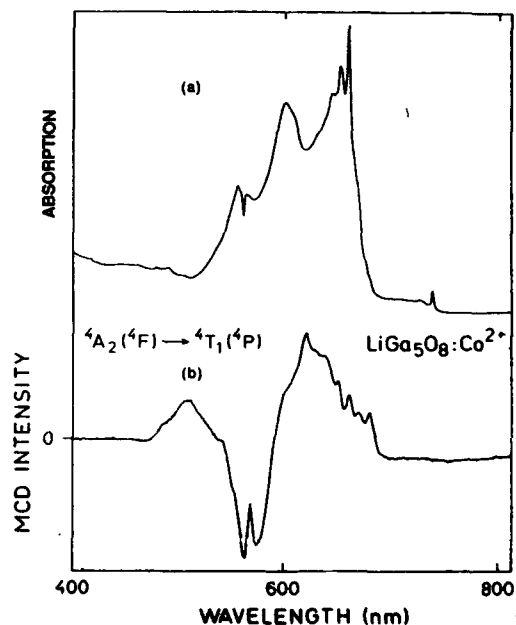


FIG. 7. (a) The ${}^4A_2({}^4F) \rightarrow {}^4T_1({}^4P)$ absorption transition recorded at 85 K. (b) The wavelength dependence of the MCD signal for the ${}^4A_2({}^4F) \rightarrow {}^4T_1({}^4P)$ transition recorded at 1.6 K. The sharp dip in the MCD signal at 566 nm is ascribed to a Fano antiresonance effect.

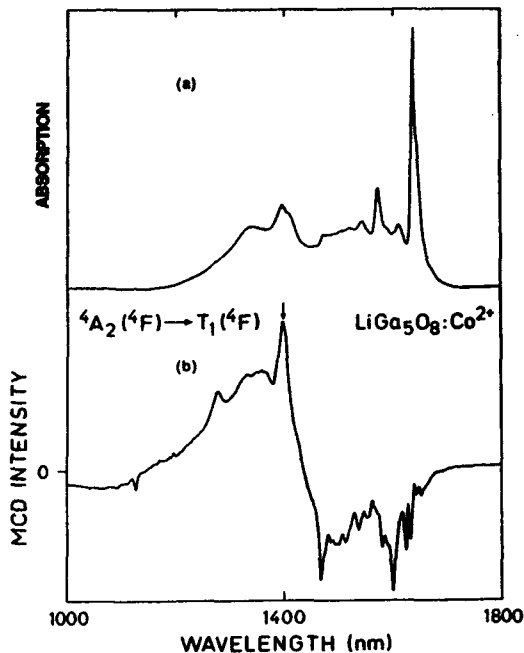


FIG. 8. (a) The ${}^4A_2({}^4F) \rightarrow {}^4T_1({}^4F)$ absorption transition recorded at 85 K. (b) The wavelength dependence of the MCD signal for the ${}^4A_2({}^4F) \rightarrow {}^4T_1({}^4F)$ transition recorded at 1.6 K.

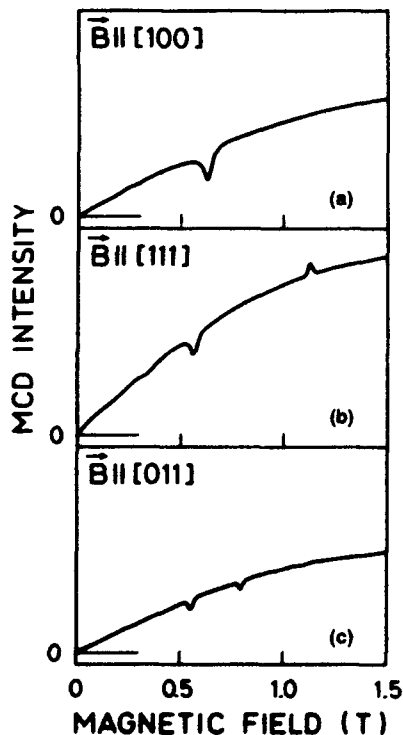


FIG. 9. The magnetic-field dependence of the MCD signal along the (a) [100], (b) [111], and (c) [011] directions recorded at the arrowed wavelength position (1400 nm) in Fig. 8. For comparison, the scaling of the y axis for the three signals is the same. The dips and peaks in the spectra are due to ODMR transitions. Note the "positive" ODMR transition for the [111]-oriented spectrum.

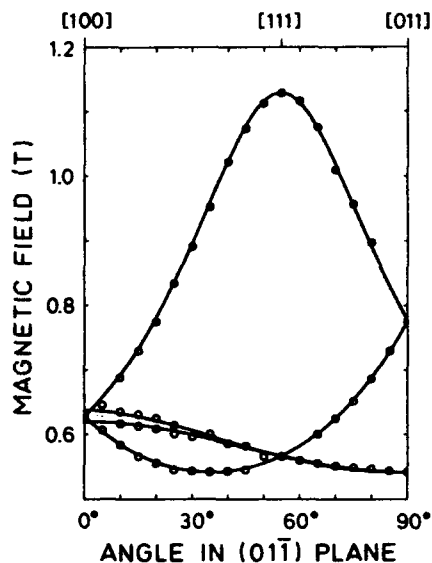


FIG. 10. The angular dependence of the ODMR signal with $B \parallel (01\bar{1})$. The C_3 symmetry for the Co^{2+} impurity is evident from the spectrum. The solid points are due to increases in the MCD signals at resonance and the open circles are due to decreases in the MCD signals at resonance. The splitting of the ODMR lines near [100] is due to a small misalignment ($\sim 2^\circ$) of the $\text{LiGa}_5\text{O}_8:\text{Co}^{2+}$ crystal.

${}^4T_1({}^4P) \rightarrow {}^4T_2({}^4F)$ and ${}^4T_1({}^4P) \rightarrow {}^4T_1({}^4F)$ transitions, respectively. The lifetime of all the luminescence bands at 10 K was found to be 200 ± 20 ns. This lifetime is constant up to room temperature within experimental error.

The red luminescence transition, recorded in greater detail at 15 K, is shown in Fig. 6(b) along with the luminescence excitation spectrum in Fig. 6(a). The two spectra in Fig. 6 are clearly mirror images of one another except for the features marked *x*, *y*, and *z* in the excitation spectrum. The frequencies (with respect to the zero-phonon line at $15\,157\text{ cm}^{-1}$) of all the fine-structure features in the spectra of Fig. 6 are given in Table I. The extra fine-structure lines in the excitation spectrum are at 46, 63, and 277 cm^{-1} from the zero-phonon line position.

In Figs. 7 and 8 we present the MCD spectra recorded at $B = 1.64\text{ T}$ and $T = 1.6\text{ K}$ for the $\text{LiGa}_5\text{O}_8:\text{Co}^{2+}$ system along with the corresponding absorption transitions at $T = 85\text{ K}$. The MCD spectra have not been corrected for the system response. The MCD band in Fig. 8(b) contains a great wealth of fine structure at this temperature, even more than is evident at 85 K in the absorption spectrum in Fig. 8(a). In the MCD spectrum of Fig. 7(b) there is a rather interesting feature at 566 nm. It is seen to be a "dip" in the MCD signal at this point. This feature is also observed as a dip in absorption strength in the absorption spectrum of Fig. 7(a).

The magnetic field variation of the MCD signal taken at $\lambda = 1400\text{ nm}$ along the [100], [111], and [011] directions is shown in Fig. 9. We note that the intensity of the MCD signal is not isotropic, as it would be if the Co^{2+} ion was at a site of full T_d symmetry. We find instead that it shows a maximum along the [111] direction [Fig.

9(b)], suggesting an axis of symmetry along this direction. In this figure we also show the ODMR transitions, identified as peaks and dips in the MCD signals. It is interesting to note that the high-field ODMR transition along [111] shows an increase in the strength of the MCD band.

The angular variation of the Co^{2+} ODMR transitions with the magnetic field B in the (011) plane is shown in Fig. 10. The solid points are due to ODMR transitions which show an increase in the total MCD signal (positive ODMR), and the open points are due to transitions which show a decrease in the MCD signal (negative ODMR). The "positive" ODMR signal is strongest along [111] and weakens quickly as the crystal is rotated towards either the [100] or [011] direction. The splitting of the ODMR lines near [100] is due to a small misalignment ($\sim 2^\circ$) of the $\text{LiGa}_5\text{O}_8:\text{Co}^{2+}$ crystal; the small size of the sample making alignment difficult.

IV. CRYSTAL-FIELD MODEL

In this section we describe our crystal-field model for the Co^{2+} center in LiGa_5O_8 . This model includes a full treatment of the C_3 crystal field which acts upon the Co^{2+} ion. We start with the electron-electron interaction, and then include the crystal-field interaction. Lastly, we consider the spin-orbit interaction, which gives rise to a splitting of the ground state. This leads to an expression for the fine-structure parameter D for the ground state.

A. Electron-electron interaction

The Co^{2+} impurity in LiGa_5O_8 has the d^7 configuration, which we treat as a three-hole configuration. In accordance with Hund's rule, the ground-state term is a 4F term. There is a second spin quadruplet, a 4P term. In the case of a free Co^{2+} ion, the 4P term is the first excited term, lying approximately $15\,500\text{ cm}^{-1}$ above the ground term.¹² The 4P - 4F splitting is reduced for the case of the Co^{2+} impurity in crystals, as a result of the greater extent of the wave functions when the ion is in a crystalline environment. We denote the 4P - 4F splitting, which can be expressed in terms of the Racah parameter B , by the single parameter Δ .

B. Crystal-field interaction

1. T_d component

We decompose the crystal-field potential into two components, which we treat separately. The first component is a field of T_d symmetry, resulting primarily from the first shell of neighbors that consists of four oxygen ions in tetrahedral coordination about the Co^{2+} ion as shown in Fig. 1. In addition, the third shell of neighbors consists of four gallium ions also in tetrahedral coordination about the Co^{2+} ion. These gallium ions are located in the corners of the left-hand octant in Fig. 1. The tetrahedral crystal field splits the one-hole d states so that the t_2 -symmetry holes are lower in energy than the e -symmetry holes by an amount $10Dq$. The partial removal of the

fivefold degeneracy of the d states splits the 4F term into three manifolds: 4A_2 , 4T_2 , and $^4T_1(^4F)$. The 4P term spans the manifold $^4T_1(^4P)$. These splittings are shown in Fig. 11, which indicates schematically the effect of various perturbations on the Co^{2+} ion in LiGa_5O_8 . The many-hole ($M_s = \frac{3}{2}$) states for these manifolds are given by

$$\begin{aligned} ^4A_2 &= (\xi, \eta, \zeta), \\ ^4T_2 &= (\epsilon, \eta, \xi), \\ ^4T_{1z}(^4F) &= 1/\sqrt{5}[(\xi, \eta, \theta) + 2(\zeta, \theta, \epsilon)], \\ ^4T_{1z}(^4P) &= 1/\sqrt{5}[2(\xi, \eta, \theta) - (\zeta, \theta, \epsilon)], \end{aligned} \quad (2)$$

where (X_1, X_2, X_3) denotes the Slater determinant of the orbitals X_1 , X_2 , and X_3 . In addition, the tetrahedral crystal field gives rise to a mixing between the $^4T_1(^4F)$ and $^4T_1(^4P)$ manifolds, resulting in the repulsion of these levels, as shown in the middle of Fig. 11.

2. C_3 component

The second component of the crystal-field potential is a component of C_3 symmetry. The second shell of neighbors around the Co^{2+} impurity consists of nine gallium ions and three lithium ions arranged as shown in Fig. 2. If all the ions in the second shell were identical, i.e., gallium ions in this case, then the site symmetry would be T_d . It is the three lithium ions that are responsible for lowering the symmetry to C_3 . Contrary to a note by Macfarlane,¹³ there is a distinction between C_3 and C_{3v} potentials, though, like the C_{3v} potentials, the C_3 potential splits each orbital triplet into an orbital singlet and an orbital doublet. [We consider an expansion of the potential in terms of spherical harmonics. The linear combination of $L=4$ spherical harmonics (neglecting the $M=0$ har-

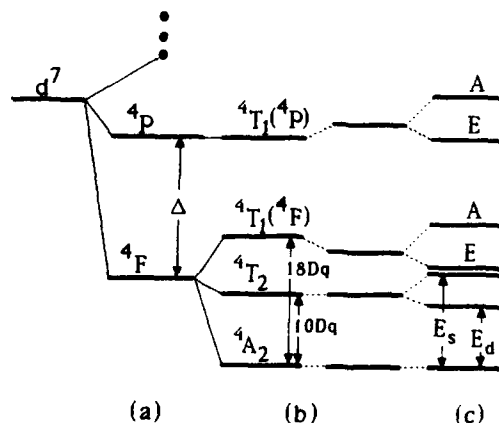


FIG. 11. Energy-level diagram showing the splittings of the d^7 configuration for the Co^{2+} impurity in LiGa_5O_8 , due to (a) the electron-electron interaction, (b) the tetrahedral component of the crystal field, and (c) the C_3 component of the crystal field. The C_3 crystal field splits each orbital triplet (T_1, T_2) into a doublet (E) and a singlet (A). The energies E_D and E_S used in the determination of the fine-structure parameter D are also shown.

monic) which describes a C_{3v} potential is $(Y_{43} - Y_{4-3})$, which is proportional to $\cos(3\phi)$,¹³ where ϕ is measured about the three-fold axis with $\phi=0$ defining one of the three reflection planes. Reflections through these planes change ϕ , but not $\cos(3\phi)$. In lowering the symmetry to C_3 , an additional term must be added to the potential and this term does not remain unchanged with reflections through these three planes but retains the three-fold rational symmetry. The linear combination $(Y_{43} + Y_{4-3})$, which is proportional to $\sin(3\phi)$, is such a term. This additional term is the distinction between the C_{3v} and the C_3 potentials.^{14]}

We write the one-electron C_3 potential within d states in terms of operators which span irreducible representations of the T_d point group. We find

$$V_{C_3} = \alpha A_1 + V(T_{2\xi} + T_{2\eta} + T_{2\zeta}) + W(T_{1x} + T_{1y} + T_{1z}), \quad (3)$$

where α , V , and W are constants. Analytic expressions for these constants can be derived, for example, by assuming a point-ion model. However, we proceed by treating these as parameters. We note that it is the last term in Eq. (3) which distinguishes this potential from one of C_{3v} symmetry. We define the following reduced matrix elements for $i, j = \xi, \eta, \zeta$ and $k = \theta, \epsilon$:

$$\begin{aligned} \langle t_{2i} | V_{C_3} | t_{2i} \rangle &= \alpha_i, \\ \langle e_k | V_{C_3} | e_k \rangle &= \alpha_e, \\ \langle t_{2i} | V_{C_3} | t_{2j} \rangle &= v/3 \quad (i \neq j), \\ \langle t_{2\xi} | V_{C_3} | e_\theta \rangle &= \sqrt{2/3}v', \\ \langle t_{2\xi} | V_{C_3} | e_\epsilon \rangle &= \sqrt{2/3}w. \end{aligned} \quad (4)$$

The parameters α_i and α_e give a contribution, in addition to that of the tetrahedral component of the crystal field, to the splitting between the t_2 and e holes. We therefore incorporate this additional contribution into the parameter $10Dq$. The parameters v and v' , which result from the $T_{2\xi} + T_{2\eta} + T_{2\zeta}$ operator, are defined following Macfarlane.¹³ The parameter w results from the $T_{1x} + T_{1y} + T_{1z}$ operator, and so does not appear as a parameter for a C_{3v} potential. Using these parameters and Eq. (3) in conjunction with the Wigner-Eckart theorem, we have exactly

prescribed the one-hole matrix elements of a C_3 potential within a basis of d holes. The nature of this potential is better understood if we make a change of basis for the t_2 states that reflects the axial nature ($\langle 111 \rangle$ -type directions) of the C_3 potential. Consider the basis set defined by

$$\begin{aligned} t_{2z} &= 1/\sqrt{3}(t_{2\xi} + t_{2\eta} + t_{2\zeta}), \\ t_{2\theta} &= 1/\sqrt{6}(2t_{2\xi} - t_{2\eta} - t_{2\zeta}), \\ t_{2\epsilon} &= 1/\sqrt{2}(t_{2\xi} - t_{2\eta}). \end{aligned} \quad (5)$$

In the basis set of d states $(t_{2z}, t_{2\theta}, t_{2\epsilon}, e_\theta, e_\epsilon)$, the one-hole matrix elements of the C_3 potential are

$$\mathcal{H}_{C_3} = \begin{bmatrix} 2v/3 & 0 & 0 & 0 & 0 \\ 0 & -v/3 & 0 & v' & w \\ 0 & 0 & -v/3 & -w & v' \\ 0 & v' & -w & 0 & 0 \\ 0 & w & v' & 0 & 0 \end{bmatrix}. \quad (6)$$

From Eq. (6), we readily see the difference in how the C_{3v} and C_3 potentials act within d states. The parameter v' mixes the $t_{2\theta, 2\epsilon}$ states with $e_{\theta, \epsilon}$ states in one sense, while the parameter w mixes these states in the opposite sense.

The matrix elements of the C_3 potential taken between the many-hole states of the four manifolds prescribed in Eq. (2) are readily determined from the one-hole matrix elements given in the previous paragraph. This results in a 10×10 matrix. This matrix can be reduced in to a 4×4 block and a 6×6 block through a change of basis for the orbital-triplet manifolds like that given in Eq. (5). Within the basis set $\{^4A_2, ^4T_{1z}(^4F), ^4T_{2z}, ^4T_{1z}(^4P)\}$, the many-hole matrix elements of the full crystal-field interaction and the electron-electron interaction are

$$\mathcal{H} = \begin{bmatrix} -6G & I & -2J & 2I \\ I & 3G+2L & -4K & -2G+2N \\ -2J & -4K & -G+2H & 2K \\ 2I & -2G+2N & 2K & F+2M \end{bmatrix}. \quad (7)$$

Within the basis set $\{^4T_{1\theta}(^4F), ^4T_{1\epsilon}(^4F), ^4T_{2\theta}, ^4T_{1\theta}(^4P), ^4T_{1\epsilon}(^4P)\}$, the many-hole matrix elements of the crystal-field and electron-electron interaction are

$$\mathcal{H} = \begin{bmatrix} 3G-L & 0 & 2K & -P & -2G-N & -J \\ 0 & 3G-L & P & 2K & J & -2G-N \\ 2K & P & -G-H & 0 & -K & -Q \\ -P & 2K & 0 & -G-H & Q & -K \\ -2G-N & J & -K & Q & F-M & 0 \\ -J & -2G-N & -Q & -K & 0 & F-M \end{bmatrix}. \quad (8)$$

The variables F, G, H, \dots, Q given above are defined by

$$\begin{aligned} F &= \Delta, \quad L = 1/5(3v/2 + 2\sqrt{2}v'), \\ G &= 2Dq, \quad M = 1/5(v - 2\sqrt{2}v'), \\ H &= v/6, \quad N = 1/5(-v/3 + 3\sqrt{2}v'/2), \\ I &= \sqrt{2/5}v', \quad P = 1/\sqrt{5}(\sqrt{3}v/2 + \sqrt{2}v'), \\ J &= w/\sqrt{2}, \quad Q = 1/\sqrt{5}(-v + v'/\sqrt{2}), \\ K &= w/\sqrt{10}. \end{aligned} \quad (9)$$

From Eqs. (7) and (8), we can show that, as required by symmetry, the C_3 potential splits the orbital triplets into an orbital singlet and an orbital doublet, as shown in Fig. 11, and we can also show how the differences between the C_3 and C_{3v} potentials affect the mixing of the orbital triplets. Diagonalizing the matrices in Eqs. (7) and (8) yields the many-hole energy levels and eigenstates for the Co^{2+} impurity in the site of C_3 symmetry.

C. Spin-orbit interaction

The spin-orbit interaction has the effect of splitting in first order each of the orbital doublets into four Kramers doublets. (Note that $S = \frac{3}{2}$.) In addition, the spin-orbit interaction in second order splits the orbital singlets into two Kramers doublets. We concentrate on the splitting of the 4A_2 ground manifold.

The spin-orbit interaction mixes the 4A_2 ground manifold with the 4T_2 manifold. The many-hole matrix elements of the orbital angular momentum L taken between the states of these two manifolds is characterized by

$$\langle T_{2c} | L_z | A_2 \rangle = 2i, \quad i = \sqrt{-1}. \quad (10)$$

This matrix element is unchanged if we transform to the basis set for the 4T_2 manifold defined by Eq. (5) and perform a similar transformation on the orbital momentum operators. For example, we define L'_z , by

$$L'_z = 1/\sqrt{3}(L_x + L_y + L_z), \quad (11)$$

which yields

$$\langle T_{2c} | L'_z | A_2 \rangle = 2i \quad (12)$$

and similarly for T_{2a} and T_{2e} with L'_x and L'_y , respectively.

We neglect for the moment the mixing of the 4T_2 manifold with the other orbital-triplet manifolds, but consider only the splitting, due to the C_3 symmetry field, of this manifold into an orbital doublet, at an energy E_D above the 4A_2 manifold, and an orbital singlet, at an energy E_S above the 4A_2 manifold. The spin-orbit interaction between the 4T_2 and 4A_2 manifolds splits the 4A_2 manifold into two Kramers doublets. One doublet is comprised of the $M_s = \pm \frac{3}{2}$ states, the second of the $M_s = \pm \frac{1}{2}$ states. The second-order energies of these two doublets are given by

$$\begin{aligned} E(\pm \frac{3}{2}) &= -3\lambda^2(3/E_S + 2/E_D), \\ E(\pm \frac{1}{2}) &= -\lambda^2(1/E_S + 14/E_D), \end{aligned} \quad (13)$$

where λ is the many-electron spin-orbit parameter. For the free Co^{2+} ion, λ is approximately -180 cm^{-1} .¹⁵ For the ion in a crystalline environment, λ is somewhat reduced (typically to 0.8 of the free-ion value) from this value.

The ground-state fine-structure parameter denoted D is a measure of the splitting between the two Kramers doublets within the ground 4A_2 manifold. We now include the mixing of the 4T_2 manifold with the other orbital-triplet manifolds. We define the fraction of the 4T_2 wave function within the i th ($i=1,2,3$) orbital doublet to be β_i , and the fraction of the 4T_2 wave function in the i th orbital singlet (neglecting the 4A_2) to be α_i . We find then that D is given by

$$\begin{aligned} D &= \frac{1}{2}[E(\pm \frac{3}{2}) - E(\pm \frac{1}{2})] \\ &= 4\lambda^2 \left[\sum_{i=1}^3 \beta_i / E_{D_i} - \sum_{i=1}^3 \alpha_i / E_{S_i} \right]. \end{aligned} \quad (14)$$

Since the fine-structure splitting is large compared with the Zeeman splitting as measured here by ODMR, we can treat the two Kramers doublets resulting from the 4A_2 manifold independently, with each doublet being described by an effective spin $S' = \frac{1}{2}$. The effective-spin Hamiltonian for each of the doublets is

$$\mathcal{H}_{\text{eff}} = \mu_B \mathbf{B} \cdot \mathbf{g} \cdot \mathbf{S}'. \quad (15)$$

The g tensor has two independent components: g_{\parallel} (along the three-fold axis) and g_{\perp} (perpendicular to the three-fold axis). In first order, the g values in the $\pm \frac{3}{2}$ manifold are $g_{\parallel} = 3g_e$ ($g_e = 2.0023$) and $g_{\perp} = 0$. The g values in first order in the $\pm \frac{1}{2}$ manifold are $g_{\parallel} = g_e$ and $g_{\perp} = 2g_e$.¹⁶

Departures of the experimental g values from these theoretical values within the $M_s = \pm \frac{1}{2}$ manifold are explained using the usual second-order corrections involving the spin-orbit interaction and the orbital Zeeman interaction. As with the fine-structure splitting, the mixing with excited states involves the states of the 4T_2 manifold. We find that

$$\begin{aligned} g_{\parallel} &= g_e - 8\lambda \sum_{i=1}^3 \alpha_i / E_{S_i}, \\ g_{\perp} &= 2 \left[g_e - 8\lambda \sum_{i=1}^3 \beta_i / E_{D_i} \right]. \end{aligned} \quad (16)$$

The results in Eq. (16) have a similar form to those in Eq. (14). Indeed, we can relate the g values to the fine-structure parameter by

$$g_{\perp}/2 - g_{\parallel} = -2D/\lambda. \quad (17)$$

V. ANALYSIS OF RESULTS AND DISCUSSION

We now proceed with the analysis of our experimental data in light of the theory developed in the previous section and of the assignments made for the observed optical transitions in Sec. III. We noted that both absorption transitions in Fig. 4 show a splitting into two bands; this splitting is due to the C_3 crystal field present at the Co^{2+}

site. The additional band with a peak at $18\,200\text{ cm}^{-1}$ in Fig. 4 is most likely due to higher-lying levels arising from the 2G free-ion level as shown in the energy-lying diagram in Fig. 4.¹⁷ Values for Δ and $10Dq$ can be estimated by fitting the average energies of the ${}^4A_2({}^4F) \rightarrow {}^4T_1({}^4P)$ and ${}^4A_2({}^4F) \rightarrow {}^4T_1({}^4F)$ transition. The experimental positions we choose for the fitting process are at $6300, 7210\text{ cm}^{-1}$ for the ${}^4A_2({}^4F) \rightarrow {}^4T_1({}^4F)$ transition and $15\,400, 16\,600\text{ cm}^{-1}$ for the ${}^4A_2({}^4F) \rightarrow {}^4T_1({}^4P)$ transition. Choosing these positions is somewhat difficult due to the presence of much vibrational structure in these spectra. Values for $v, v',$ and w are then chosen and the matrices in Eqs. (7) and (8) are diagonalized iteratively until a good fit to the experimental positions is found. The following values are found from our analysis:

$$\begin{aligned}\Delta &= +10\,781\text{ cm}^{-1}, \quad v = +1362\text{ cm}^{-1}, \\ 10Dq &= +3770\text{ cm}^{-1}, \quad v' = -10\text{ cm}^{-1}, \\ w &= \pm 20\text{ cm}^{-1}.\end{aligned}\quad (18)$$

These values give an excellent fit to the experimental positions. Hund's rule requires that the ground state be the 4F term; so we require Δ to be positive. The strong tetrahedral component of the crystal field, coming primarily from the four nearest-neighbor oxygen ions, determines the sign of $10Dq$. These oxygen ions are negatively charged. The lobes of the t_2 -symmetry hole orbitals are closer to the oxygen ions than the lobes of the e -symmetry hole orbitals. Hence, the t_2 -symmetry holes are lower in energy than the e -symmetry holes, making $10Dq$ positive. Setting the signs of these parameters we find that the signs of v and v' are determined to be positive and negative, respectively. The fit to the data is insensitive to the sign of w . This fitting procedure suggests that, for each orbital triplet, the doublet is shifted down in energy and the singlet shifted up in energy by the C_3 crystal field.

The positive sign of v is physically reasonable. In an ionic model, the gallium ions possess a $+3e$ charge and the lithium ions a $+1e$ charge. Hence, the perturbation potential resulting from the lithium ions is that of three negatively charged ions in a C_3 symmetry configuration. The lobes of the t_{2z} hole orbital lie in a plane perpendicular to the C_3 symmetry axis and the lobes of the $t_{2\theta}$ and t_{2e} hole orbitals, are therefore closer to the lithium ions. Hence, these latter two orbitals have a lower energy than the t_{2z} orbital. Equation (6) therefore implies that v is positive.

The signs of v' and w are much harder to explain in physical terms. We note, however, that, in the point-ion model for this defect, v' is predicted to have a sign opposite to that of v , and w is predicted to have the same sign as v . We recall that the sign of w is not determined in our fit. In any event, both v' and w are found to be small in our case.

An interesting feature of this Co^{2+} system is the sharp dip observed at 566 nm in the absorption spectrum in Fig. 7(a) and in the MCD signal of Fig. 7(b). We believe that the dip is due to Fano antiresonance effect such as has been observed in $\text{KMgF}_3:\text{V}^{2+}$ and in Cr^{3+} doped

glasses.^{18,19} Consulting the Tanabe-Sugano diagram for a d^7 ion in tetrahedral symmetry,¹⁷ we find that there are a number of levels originating on the free-ion 2G level which are expected to lie in this general spectral region. We are unable to make any definitive electronic assignment for the antiresonance feature.

The width of the zero-phonon $15\,157\text{-cm}^{-1}$ line of the ${}^4T_1({}^4P)$ level in luminescence is 24 cm^{-1} (full width at half maximum) at 15 K . A series of nonresonant fluorescence line narrowing (FLN) experiments were performed in order to investigate structure hidden within this large inhomogeneous profile. The detailed results of this investigation have been published elsewhere.²⁰ From these FLN measurements, the ground-state splitting due to a combination of the C_3 crystal field and spin-orbit coupling is 19.5 cm^{-1} , from which we obtain $D = 9.75\text{ cm}^{-1}$.

The optical spectra in Figs. 4–8 show a considerable number of sharp-line features. As indicated above, each of the crystal-field levels is further split by spin-orbit coupling, the doublet into four components and the singlet into two components. As a result the ${}^4A_2({}^4F) \rightarrow {}^4T_1({}^4P)$ absorption spectrum in Fig. 4 should contain six electronic components among a large number of vibrational side-band features. It is difficult to identify transitions to these electronic levels in the absorption spectra shown in Fig. 4 which were taken at 85 K . However, in the excitation spectrum of the ${}^4T_1({}^4P) \rightarrow {}^4A_2({}^4F)$ luminescence transition shown in Fig. 6(a), recorded at 15 K under much higher resolution, the features labeled x, y, z are clearly electronic as they are not observed in the corresponding luminescence spectrum. We tentatively identify the line at $15\,157\text{ cm}^{-1}$ and the features at $46, 63,$ and 277 cm^{-1} above $15\,157\text{ cm}^{-1}$ as the spin-orbit split components of the orbital doublet level coming from ${}^4T_1({}^4P)$. The possible presence of levels arising from the 2G free-ion level in this spectral region is a complicating factor making our identification rather tentative. The ${}^4A_2({}^4F) \rightarrow {}^4T_1({}^4F)$ transition in Figs. 4 and 8 is particularly rich in spectral features making identification of the six expected electronic components very difficult. Nevertheless, we can reasonably assign the lines at 6060 and 7140 cm^{-1} to electronic transitions.

The very fast radiative decay time of the luminescence transitions at low temperature indicates that these transitions have a strong electric dipole character and, consequently, have a large oscillator strength. This comes about because, in the tetrahedral site (in which the site symmetry is C_3), in LiGa_5O_8 the odd-parity crystal field mixes the $3d$ states of Co^{2+} with higher-energy states of opposite parity, and this mixing is responsible for the electric-dipole character of this transition. The lack of discernible change in the lifetime up to room temperature indicates the absence of a competing nonradiative decay process for this level and strongly suggests that the luminescence process is very efficient. The room-temperature luminescence spectrum in Fig. 5 shows three broadbands which have high luminescence efficiency. In contrast to both $\text{ZnO}:\text{Co}^{2+}$ (Ref. 21) and $\text{ZnAl}_2\text{O}_4:\text{Co}^{2+}$ (Ref. 11), the luminescence bands in Fig. 5 originate on the ${}^4T_1({}^4P)$ level rather than the 2E level. From the

Tanabe-Sugano diagram¹⁷ we find that luminescence transitions originating on the ${}^4T_1({}^4P)$ are very broad due to the sensitivity of the ${}^4T_1({}^4P)$ level to the crystal-field environment. Luminescence transitions from the 2E level consist of sharp lines due to its insensitivity to the crystal field. The three luminescence transitions observed in $\text{LiGa}_5\text{O}_8 \cdot \text{Co}^{2+}$ are also spin allowed, which contributes to their large oscillator strength. The combination of broad luminescence transitions coupled with a large oscillator strength makes $\text{LiGa}_5\text{O}_8 \cdot \text{Co}^{2+}$ an ideal candidate for a tunable solid-state laser in the visible and near infrared.

The "positive" ODMR lines in Figs. 9 and 10 are an interesting feature of these samples. We would intuitively feel that the ODMR transition should equalize the populations of the ground-state levels as illustrated in Fig. 3 and thereby cause a reduction of the MCD signals in Fig. 9. Along the [100] direction the four Co^{2+} sites in the unit cell all make the same angle with the applied magnetic field B . We therefore see only a single ODMR transition as in Fig. 9(a). When the applied magnetic field is along the [111] direction, the four $\langle 111 \rangle$ -type centers are no longer equivalent; the center aligned along the magnetic field is distinguished from the other three. In this case we expect to see two ODMR transitions as observed in Fig. 9(b). The low-field ODMR transition shows a reduction in the MCD signal as expected. On the other hand, the high-field ODMR transition appears to show an increase in the total MCD signal. The total MCD signal observed is a combination of the parallel MCD signal and the MCD signals from the other three centers. The MCD signal for the parallel center must therefore be opposite in sign to that from the other centers. For the example shown in Fig. 3, this would mean that the Zeeman splitting of the ground or excited states for the parallel center is opposite to that for the other three centers. We find that, as the magnetic field is rotated away from the [111] direction, the intensity of the "positive" ODMR lines weakens (Fig. 10) and eventually the ODMR lines become negative. This result is a further demonstration that the site occupied by the Co^{2+} ion has an axis of symmetry along $\langle 111 \rangle$ -type directions. Along the [111] direction the coupling between the Kramers doublets participating in the MCD signal with all the other Kramers doublets within the d^7 shell is at a minimum. Rotating the magnetic field B away from [111] results in an admixture into the ground and excited states which eventually leads to a reversal of the Zeeman splitting as the magnetic field approaches the [100] and [011] directions (Fig. 10). This effect was also observed by Ahlers *et al.*²² for the Ti^{3+} center in KCl. While this gives a qualitative explanation for the observed effect, the microscopic origin for this reversal of the Zeeman splitting has not been determined.

The ODMR line positions in Fig. 10 can be fitted to the spin Hamiltonian in Eq. (15) with the two independent g values, $g_{\perp} = 2.215$, $g_{\parallel} = 4.628$. The fit to the experimental data is shown as the solid lines in Fig. 10. These g values indicate that the observed ODMR transitions are within the $\pm \frac{1}{2}$ levels of the ground state and so the sign

of the fine-structure parameter D is positive from Eq. (14). As $g_{\perp}/2 > g_{\parallel}$, we are again led to the conclusion from Eq. (16) that the orbital doublets arising from the orbital triplet manifolds are lower in energy than the orbital singlets. At the low temperatures of the MCD-ODMR experiments the population of the $\pm \frac{1}{2}$ levels is very small and so no signals were observed in this doublet. From Eq. (17) we estimate the spin-orbit constant to be $\lambda = -193 \text{ cm}^{-1}$. We can also estimate λ from Eq. (14). In doing this we use the theoretical estimate for the positions of the 4T_2 doublet and singlet split levels and in this case we find $\lambda = -190 \text{ cm}^{-1}$. Both values are quite similar but somewhat surprising as we would normally expect to see a reduction in λ from the free-ion case.

Both the ODMR and the optical zero-phonon linewidths are quite broad. The ODMR linewidth is 20 mT and exhibits no resolved hyperfine structure associated with the ${}^{57}\text{Co}$ nucleus (100% abundant) which has a nuclear spin of $I = \frac{7}{2}$. We noted earlier that the inhomogeneous optical zero-phonon transition linewidth is 24 cm^{-1} so that the large ground-state splitting could not be resolved. The Co^{2+} ion substitutes for Ga^{3+} in the lattice and some charge compensation is thus required to maintain charge neutrality. Both of these broad linewidths are probably due to a distribution of positions for the charge compensating ions which would result in a distribution of strains at the sites of the substitutional Co^{2+} ions in the LiGa_5O_8 lattice. At present we do not know what species is providing the charge compensation for the Co^{2+} . It is interesting to note that the behavior shown in Fig. 10 is consistent with the C_3 symmetry deduced from the crystal structure, and this would imply that either the charge compensating ion is far away from the Co^{2+} ion or located along a $\langle 111 \rangle$ -type direction.

VI. CONCLUSIONS

The optical spectra of Co^{2+} in LiGa_5O_8 provide clear evidence that the Co^{2+} ions substitute for tetrahedrally coordinated Ga^{3+} ions in this lattice and therefore occupy sites of C_3 symmetry, as illustrated in Fig. 2. We have presented a detailed crystal-field model for the Co^{2+} ion in this site, and we have deduced the crystal-field parameters. Strong luminescence with a lifetime of 200 ns is observed to three lower levels from the ${}^4T_1({}^4P)$ level. In a previous publication this system was suggested as a possible candidate as a visible-infrared laser system.⁹ Further experiments to look at excited-state absorption effects would have to be undertaken to determine the potential of $\text{LiGa}_5\text{O}_8 \cdot \text{Co}^{2+}$ as a laser system. Within the accuracy of the ODMR experiment, the site symmetry of the Co^{2+} ion is C_3 , suggesting that charge compensating ions are either far removed from the Co^{2+} or are along the C_3 axis.

ACKNOWLEDGMENTS

We would like to express our gratitude to Professor G. D. Watkins of Lehigh University where the MCD-

ODMR measurements were performed. This work was supported in part by Optronics Ireland, a division of EO-LAS, and by the Air Force Office of Scientific Research, Air Force Systems Command, USAF, under Grant No. AFOSR 88-0355. The work carried out at Lehigh University (by FGA and JFD) was supported by the U.S.

Office of Naval Research, under Grant No. N00014-90-J-1264 and by the National Science Foundation under Grant No. DMR-85-20269. The Ge detector was obtained through a grant from the University College Galway Development Fund which we gratefully acknowledge.

- ¹R. Pappalardo, D. L. Wood, and R. C. Linares, Jr., *J. Chem. Phys.* **35**, 2041 (1961).
- ²D. L. Wood and J. P. Remeika, *J. Chem. Phys.* **46**, 3595 (1967).
- ³T. J. Glynn, L. Kelleher, G. F. Imbusch, D. M. Larkin, F. R. Merritt, and M. J. Berggren, *J. Chem. Phys.* **55**, 2925 (1971).
- ⁴E. W. Gorter, *Philips Res. Rep.* **9**, 295 (1954).
- ⁵T. J. Glynn, J. P. Larkin, G. F. Imbusch, D. L. Wood, and J. P. Remeika, *Phys. Lett.* **30A**, 189 (1969).
- ⁶T. Abritta, N. V. Vugman, F. de Souza Barros, and N. T. Melamed, *J. Lumin.* **31&32**, 281 (1984).
- ⁷C. McShera, P. J. Collieran, T. J. Glynn, G. F. Imbusch, and J. P. Remeika, *J. Lumin.* **28**, 41 (1983).
- ⁸J. F. Donegan, F. J. Bergin, T. J. Glynn, G. F. Imbusch, and J. P. Remeika, *J. Lumin.* **35**, 57 (1986).
- ⁹J. F. Donegan, G. P. Morgan, T. J. Glynn, and G. Walker, *J. Mod. Opt.* **37**, 769 (1990).
- ¹⁰R. M. Macfarlane and J.-C. Vial, *Phys. Rev. B* **34**, 1 (1986).
- ¹¹J. Ferguson, D. L. Wood, and L. G. Van Uitert, *J. Chem. Phys.* **51**, 2904 (1969).
- ¹²C. E. Moore, *Atomic Energy Levels*, Natl. Bur. Stand. (U.S.) Circ. No. 467 (U.S. GPO, Washington, D.C., 1952), Vol. II, p. 85.
- ¹³R. M. Macfarlane, *J. Chem. Phys.* **39**, 3118 (1963).
- ¹⁴The authors would like to thank Professor F. S. Ham for helpful discussions on this point.
- ¹⁵J. S. Griffith, *The Theory of Transition-Metal Ions* (Cambridge University, Cambridge, 1961), p. 437.
- ¹⁶G. E. Pake and T. L. Estle, *The Physical Principles of Electron Paramagnetic Resonance* (Benjamin, London, 1973), p. 127.
- ¹⁷B. Henderson and G. F. Imbusch, *Optical Spectroscopy of Inorganic Solids* (Oxford Science, Oxford, 1989), p. 130.
- ¹⁸M. D. Sturge, M. J. Guggenheim, and M. H. L. Pryce, *Phys. Rev. B* **2**, 2459 (1970).
- ¹⁹A. Lempicki, L. Andrews, S. J. Nettel, and B. C. McCollum, *Phys. Rev. Lett.* **44**, 1234 (1980).
- ²⁰J. F. Donegan, T. J. Glynn, and G. F. Imbusch, *J. Lumin.* **45**, 23 (1990).
- ²¹R. M. Macfarlane and J.-C. Vial, *Mater. Sci. Forum* **10-12**, 845 (1986).
- ²²F. J. Ahlers, F. Lohse, J.-M. Spaeth, and L. K. Mollenauer, *Phys. Rev. B* **28**, 1249 (1983).

Luminescence from Cr^{3+} centres in forsterite (Mg_2SiO_4)T.J. Glynn, G.F. Imbusch and G. Walker¹*Department of Physics, University College, Galway, Ireland*

Laser action, tunable around 1.2 μm , has been reported in Cr-activated forsterite (Mg_2SiO_4). We have examined the emission from this material in the region 650-850 nm via photoluminescence, excitation and lifetime studies over a range of temperature. Our measurements indicate that the emission in this region can be assigned to transitions on Cr^{3+} ions in high-field octahedral sites. The emission from the M1 site is clearly identified. We propose a simple model to account for the temperature dependence of the luminescence.

1. Introduction

When doped with chromium ions, forsterite (Mg_2SiO_4) has been shown to support laser action over a limited spectral range around 1.2 μm [1-4]. However, although several studies have concentrated on this system, there is still some doubt about the Cr valence state responsible for the lasing transition and about the exact nature of the particular sites occupied by these Cr ions. Forsterite has an orthorhombic crystal structure with two inequivalent octahedral sites occupied by Mg^{2+} ions, one with inversion symmetry (M1) and one with mirror symmetry (M2). Although the initial report ascribed the lasing band at room temperature to the ${}^4\text{T}_2 \rightarrow {}^4\text{A}_2$ transition on Cr^{3+} ions in such sites [1], more recent investigations [3,4] have assigned the lasing emission to transitions on Cr^{4+} ions in tetrahedral sites (replacing the Si ions). The complete luminescence spectrum of Cr-doped forsterite is shown in fig. 1 and consists of many overlapping bands, which extend from 650 nm to beyond 1.4 μm , and the relative intensities of these bands vary with the wavelength and polarization of the excitation source. In this investigation, we have concentrated on the emission in the region 650-850 nm which we ascribe to Cr^{3+} centres in distorted octahedral sites.

¹ Permanent address: Dept. of Pure and Applied Physics, UMIST, P.O. Box 88, Manchester M60 1QD, UK.

2. Experimental results

Oriented samples of Cr-doped forsterite, Czochralski-grown and containing (A) 0.013%, (B) 0.027% and (C) 0.08% Cr by weight, were used in our studies. Previous EPR measurements by Rager [5] on sample (A) showed clearly the presence of Cr^{3+} ions in M1 and M2 sites in the ratio M1 : M2 ~ 3 : 2. The ground-state splitting, obtained from the EPR data, was 2.2 cm^{-1} in M1 and 1.4 cm^{-1} in M2.

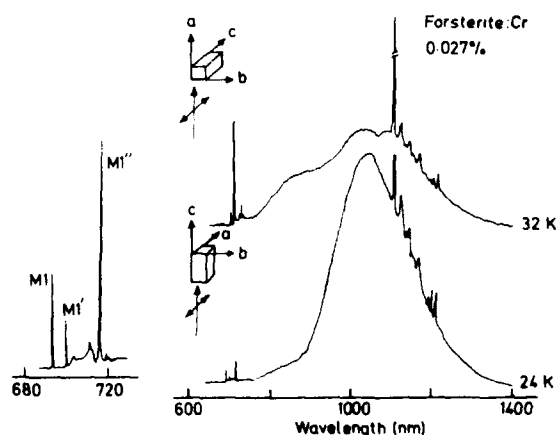


Fig. 1. The low-temperature emission from Mg_2SiO_4 (forsterite) doped with chromium excited by an argon-ion laser (all lines). The sharp features around 700 nm are shown at higher resolution. These spectra are not corrected for the response of the germanium diode detector.

The low temperature luminescence spectrum around 700 nm for sample (B) is shown in the inset in fig. 1 and for samples (B) and (C), at higher resolution, in fig. 2. It consists of a sharp electronic transition at about 14 437 cm⁻¹ and an associated phonon sideband. Based on the splitting of 2.2 cm⁻¹ observed in this line at low temperature, it is assigned to the R₁-line transition from the lowest ²E level to the ⁴A₂ ground state of the Cr³⁺ ion in the M1 site. Additional sharp lines at 14 295 and 13 967 cm⁻¹ (indicated by M1' and M1'') show splittings of 2.15 and 1.8 cm⁻¹, respectively, and may be due to emission from M1 sites perturbed by neighbouring charge-compensating vacancies. Some additional satellite features on the M1 line may have a similar origin. These satellite lines are more clearly evident in the spectrum of the (C) sample (0.08% Cr) shown in fig. 2 and an additional band appears in this sample at about 12 900 cm⁻¹ (775 nm), which may be due to different Cr³⁺ centres for which the ⁴T₂ level lies lowest at low temperature (i.e. low-field sites). Even at low doping, additional broad bands are observed at about 850 and 1050 nm (fig. 1) whose origin is also uncertain. The relative intensities of

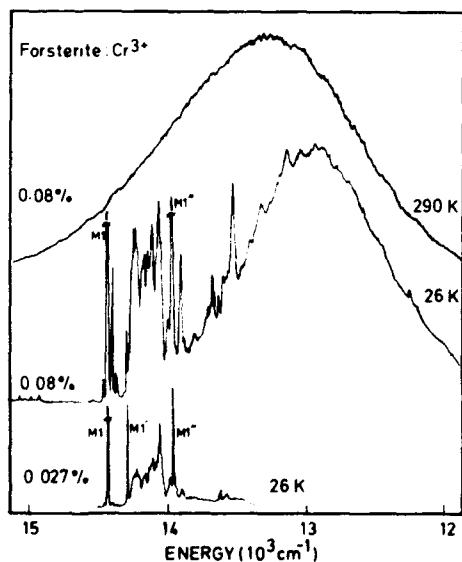


Fig. 2. The luminescence from Cr³⁺ centres in forsterite samples (B) and (C) (see text). An argon ion laser (all lines) was used for excitation. The photomultiplier response was S20.

all the features depend on the excitation wavelength and polarisation, and on the Cr doping level.

The M1 site has inversion symmetry, and the measured lifetime at low temperature of the R₁ line is 8.8 ms, consistent with a magnetic dipole transition in the R₁ line and a vibronic process – an electric dipole transition induced by odd-parity vibrations – in the sidebands. We expect the vibronic sideband process to dominate the M1 emission at low temperatures. Assuming that the M1' and M1'' sites do not have inversion symmetry, both their R₁ lines and sidebands should be electric dipole processes, and the R₁ to sideband ratio should be much larger for these centres than for the M1 sites [6]. The sideband shown in fig. 2 is therefore due mainly to emission from M1 sites. From the variation with temperature of the luminescence spectrum (fig. 3), and from excitation studies, the R₁-R₂ separation of the M1 and M1' centres were measured to be 196 and 265 cm⁻¹, respectively. The R₂ line from the M1'' centre could not be located with certainty. The splittings of both the ²E and ⁴A₂ levels of Cr³⁺ ions in M1 and M1' sites are unusually large and indicate significant distortion of the octahedral environment of these sites.

The energy level structure for the Cr³⁺ ions in forsterite is similar to that in alexandrite [7] and, as the temperature is increased, the higher-lying ⁴T₂ level becomes populated and emission from this level dominates the spectrum at room temperature (fig. 3). Since the transition from the ⁴T₂ level is spin-allowed, it will have a higher oscillator strength and the overall lifetime will decrease. The variation of the lifetime of the principal emission lines with temperature is shown in fig. 4. The lifetime of the M1 line varies from 8.8 ms at low temperature to 340 μs at room temperature. Assuming that non-radiative relaxation does not occur, and ignoring the splittings in the ²E and ⁴T₂ levels, the variation of the lifetime τ with temperature is given by [7]

$$\frac{1}{\tau} = \frac{f_E + 3f_T \exp(-\Delta/kT)}{1 + 3 \exp(-\Delta/kT)}, \quad (1)$$

where f_E , f_T are the radiative rates from the ²E and ⁴T₂ levels, respectively, and Δ is the energy separation between ²E and ⁴T₂. A value of 114 s⁻¹ is

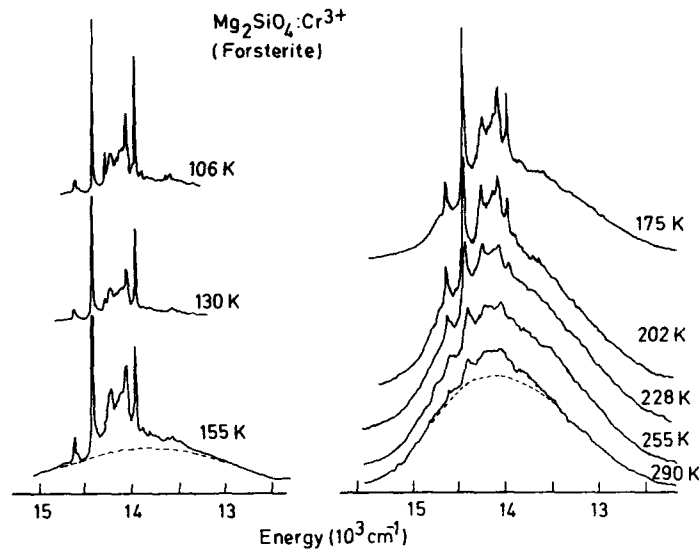


Fig. 3. The luminescence from Cr³⁺ centres in sample (B) (0.027% Cr) at various temperatures. The dotted lines indicate the assumed separation of the broad band and sharp-line features in the emission.

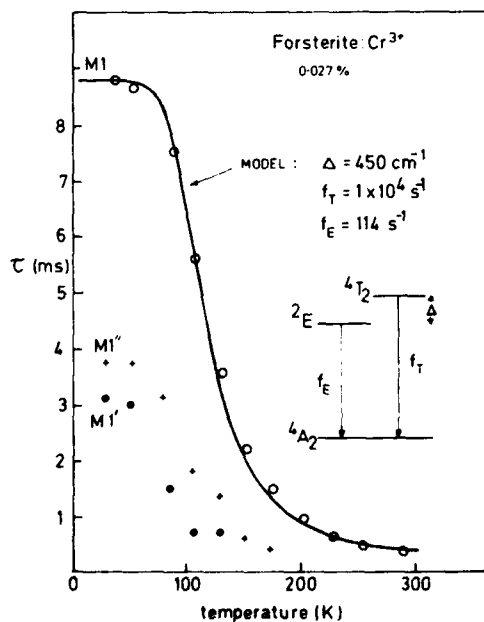


Fig. 4. The variation of the lifetime with temperature for the principal features in the luminescence spectrum. The solid curve is a plot of eq. (1) using the parameters shown in the figure.

obtained for f_E from the low temperature lifetime. The ratio of the intensities I_B in the broad band (${}^4T_2 \rightarrow {}^4A_2$) and I_S in the sharp (M1) line (${}^2E \rightarrow {}^4A_2$) should vary with temperature approximately as [8]

$$I_B/I_S \propto 3(f_T/f_E) \exp(-\Delta/kT), \quad (2)$$

and so a plot of $\ln(I_B/I_S)$ versus $1/T$ should give a straight line with slope Δ . The ratio I_B/I_S was calculated as a function of temperature from the spectra in fig. 3 by inferring the relative contributions from 2E and 4T_2 from the shape of the total luminescence spectrum (indicated by dotted lines in fig. 3). When fitted to eq. (2) a value of 420 cm^{-1} was indicated for Δ . Using this value as a guide, the parameters in eq. (1) were varied until a best fit to the data in fig. 4 was obtained. The calculated variation is shown as the solid line in fig. 4, with the parameter values shown in the figure. In spite of the crudeness of the model, the agreement is excellent. (There is a similar decrease in the lifetime of the M1' and M1'' centres, indicating in these cases also the presence of an adjacent 4T_2 state.) At the concentration of Cr in sample (B), there is no evidence for any energy transfer from

Cr³⁺ ions to the lasing centre which emits at 1.2 μm, which was suggested by other workers [2], or for any non-radiative component in the emission from these ions up to room temperature. The above analysis suggests that the radiative quantum efficiency of the system is high and the energy-level structure and lifetimes make it a suitable candidate for tunable operation in the near IR. However, Cr-doped forsterite contains many complex centres [9] and, at low doping levels, the centre responsible for laser action at longer wavelengths seems to be dominant. This centre absorbs throughout the visible and near IR and appears to prevent lasing on the Cr³⁺ centres described above.

3. Conclusion

The nature of the lasing centre in forsterite:Cr is still not established with certainty and much work remains to be done in unravelling the many complex centres in this material. We have concentrated on identifying the emission from Cr³⁺ ions in various sites so that their role in the luminescence of the forsterite system can be clearly established.

Acknowledgements

We wish to thank H. Rager, University of Marburg, FRG, for several samples of forsterite used in these studies, and W.M. Yen, University

of Athens (Georgia), for helpful discussions and for communicating his results on this material prior to publication. The Ge detector was obtained through a grant from the University College Galway Development Fund which we acknowledge with gratitude. This research work was supported in part by the Air Force Office of Scientific Research, Air Force Systems Command, USAF, under grant number AFOSR-88-0355.

References

- [1] V. Petricevic, S.G. Gayen, R.R. Alfano, K. Yamagishi, H. Anzai and Y. Yamaguchi, *Appl. Phys. Lett.* 52 (1988) 1040.
- [2] V. Petricevic, S.G. Gayen and R.R. Alfano, *Appl. Phys. Lett.* 53 (1988) 2590.
V. Petricevic, S.G. Gayen and R.R. Alfano, *OSA Proc. on Tunable Solid State Lasers*, Vol. 5, eds. M.L. Shand and H.P. Jenssen (1989) p. 77.
- [3] H.R. Verdun, L.M. Thomas, D.M. Androuskas, T. McCollum and A. Pinto, *Appl. Phys. Lett.* 53 (1989) 2593.
- [4] H.R. Verdun, L.M. Thomas and D.M. Androuskas, *OSA Proc. on Tunable Solid State Lasers*, Vol. 5, eds. M.L. Shand and H.P. Jenssen (1989) p. 85.
- [5] H. Rager, *Phys. Chem. Minerals* 1 (1977) 371.
- [6] J.F. Donegan, T.J. Glynn, G.F. Imbusch and J.P. Remeika, *J. Lumin.* 36 (1986) 93.
- [7] J.C. Walling, O.G. Peterson, H.P. Jenssen, R.C. Morris and E. Wayne O'Dell, *IEEE J. Quantum Electron.* QE-16 (1980) 1302.
- [8] B.D. MacCraith, T.J. Glynn, G.F. Imbusch and C. McDonagh, *J. Phys. C* 13 (1980) 4211.
- [9] R. Moncorge, D.J. Simkin, G. Cormier and J.A. Capobianco, *OSA Proc. on Tunable Solid State Lasers*, Vol. 5, eds. M.L. Shand and H.P. Jenssen (1989) p. 93.

New materials for tunable lasers in the near infrared

J. F. DONEGAN, G. P. MORGAN, T. J. GLYNN
and G. WALKER†

Physics Department, University College, Galway, Ireland

Abstract. There has been considerable recent effort aimed at realising tunable near-infrared laser action in solid-state media. Beyond $1\ \mu\text{m}$ Ni^{2+} and Co^{2+} emissions have been mainly studied, and laser action has been achieved in several materials doped with these ions although usually only at low temperatures. Luminescence from Co^{2+} and Ni^{2+} in the host material LiGa_5O_8 is described and evidence is presented for a high quantum efficiency, even up to room temperature. We describe also the results of our lifetime and luminescence measurements on the various active centres in the $\text{Mg}_2\text{SiO}_4:\text{Cr}$ laser system.

1. Introduction

Renewed activity in development of solid-state lasers operating in the $0.7\text{--}2.0\ \mu\text{m}$ region of the spectrum has been stimulated by the achievement of laser action in alexandrite ($\text{BeAl}_2\text{O}_4:\text{Cr}^{3+}$), the first tunable solid-state laser to operate at room temperature [1]. The success of this system, tunable from 700 to 800 nm, has led to a revival of research on such phonon-terminated solid-state lasers [2, 3]. Efforts to extend the range covered directly by primary tunable laser systems further into the i.r. are driven by specific needs for such systems, for example, semiconductor characterisation, remote sensing, integrated optica, communications and medical applications.

Much work has been concentrated on Co^{2+} and Ni^{2+} -doped materials as potential laser media, and indeed laser action has been achieved in the range $1.15\text{--}1.8\ \mu\text{m}$ for systems based on Ni^{2+} [4] and in the range $1.5\text{--}2.4\ \mu\text{m}$ for systems based on Co^{2+} [5]. With one exception, these lasers operate only at low temperature and extension to room temperature has been inhibited by luminescence quenching (due to non-radiative effects) and by excited state absorption (ESA) [4]. Thus the search for more efficient laser materials for the near i.r. region will entail the investigation of new host materials, the elucidation of the non-radiative processes and accurate spectroscopic analyses to identify the levels and transitions responsible for ESA. In this paper, we give details of the spectroscopic properties of $\text{LiGa}_5\text{O}_8:\text{Co}^{2+}$ and $\text{LiGa}_5\text{O}_8:\text{Ni}^{2+}$ which are potential tunable laser media for room-temperature operation in the near i.r. We will also present preliminary measurements on the latest chromium-doped laser system, $\text{Mg}_2\text{SiO}_4:\text{Cr}$.

†Department of Pure and Applied Physics, UMIST, P.O. Box 88, Manchester M60 1QD, England.

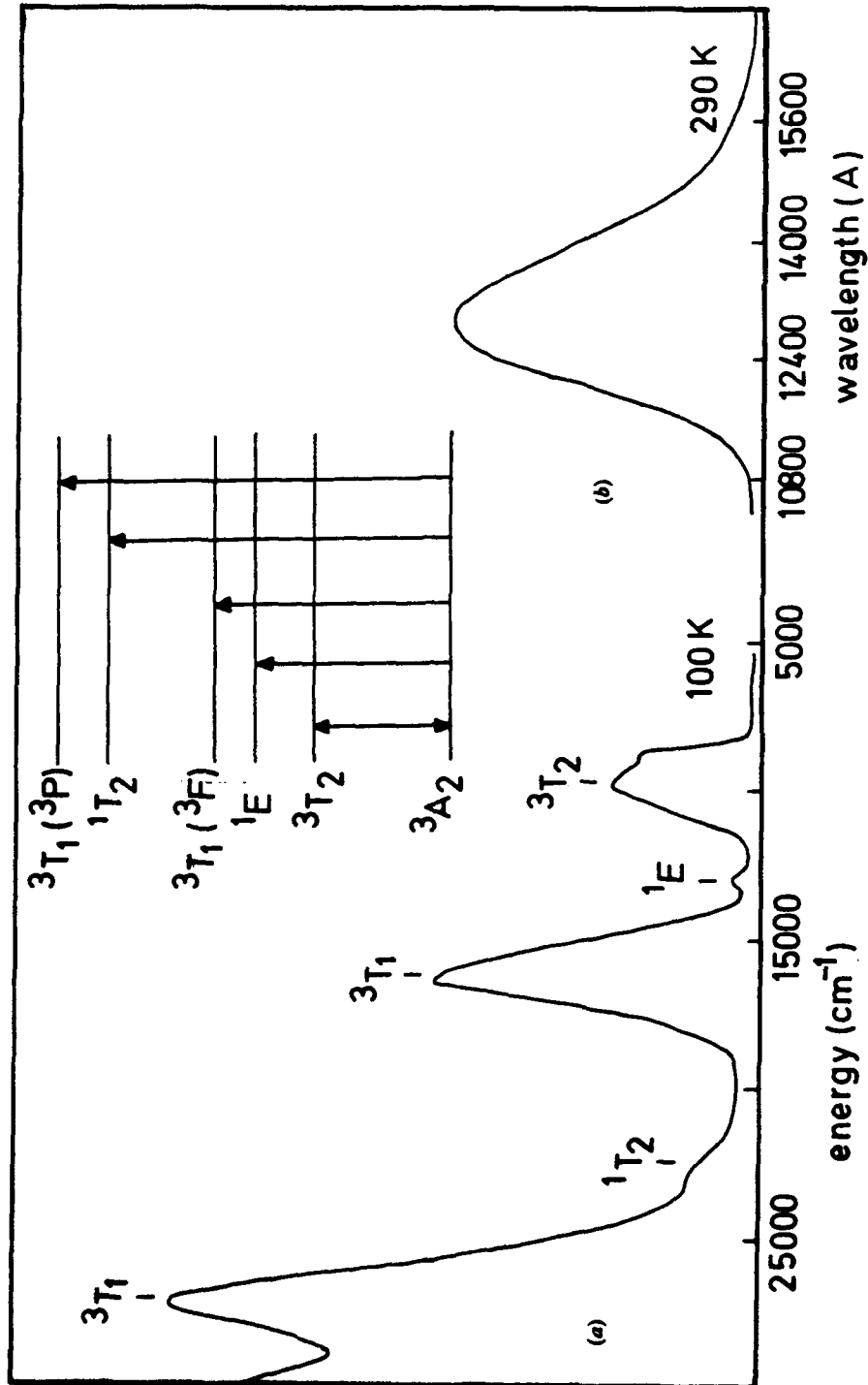


Figure 1. (a) The absorption spectrum, and (b) the luminescence spectrum of $\text{LiGa}_3\text{O}_8:\text{Ni}^{2+}$ at 100 K and 290 K respectively. The energy level structure for the Ni^{2+} ion in LiGa_3O_8 is also shown.

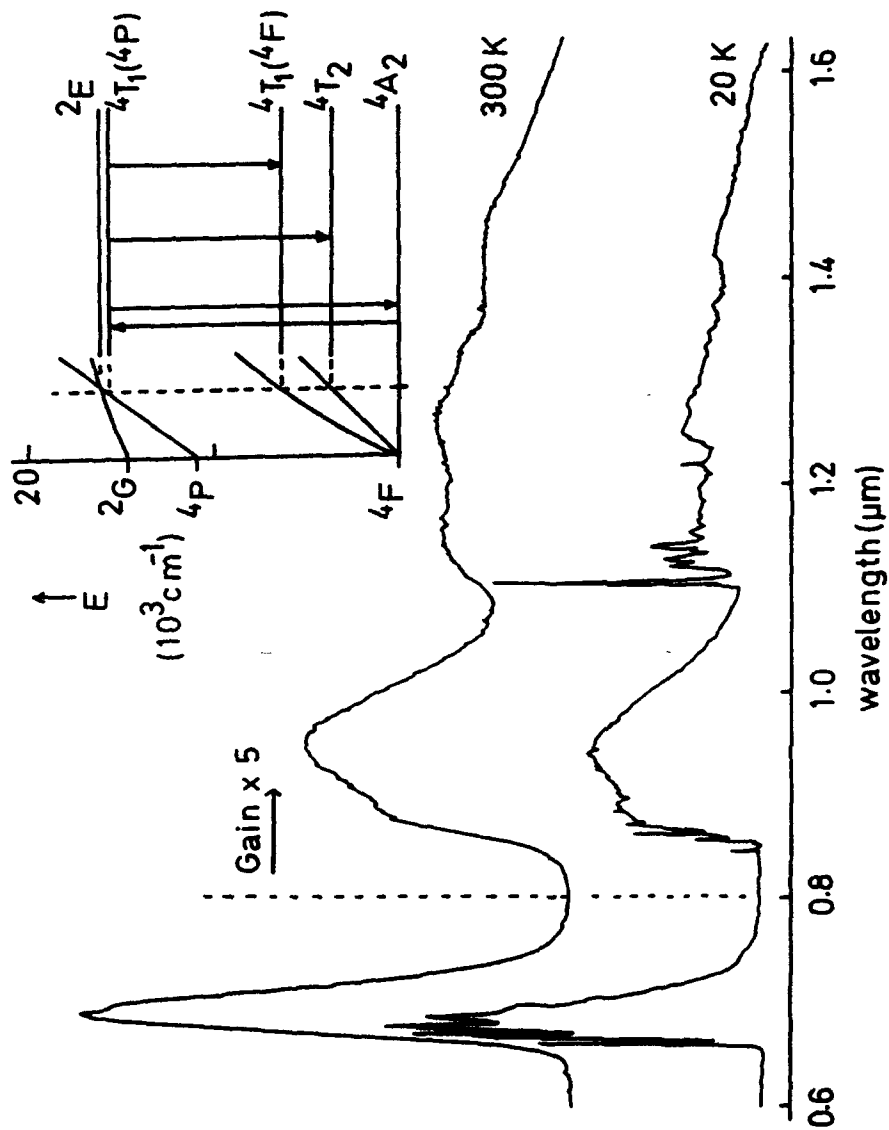


Figure 2. The luminescence spectrum of $\text{LiGa}_5\text{O}_8 : \text{Co}^{3+}$ recorded at 24 K and 300 K. The energy level structure of the Co^{3+} ion in a tetrahedral site in this material is also shown.

2. Experimental results

2.1. $\text{LiGa}_5\text{O}_8 : \text{Ni}^{2+}$

The spectroscopy of the Ni^{2+} ion incorporated as an impurity in various host materials has been well studied [4, 6]. Investigations of Ni^{2+} in MgO , MgF_2 , KMgF_3 , [6] and in fluorozirconate glass [7] show that luminescence in the visible (green and red) and infrared is observed from the Ni^{2+} ions in these materials. Referring to the schematic energy-level diagram shown in figure 1, which is typical of the Ni^{2+} ion in oxide crystals, the strongest absorption transitions in the Ni^{2+} ion are ${}^3T_1({}^3P) \leftarrow {}^3A_2$ (blue), ${}^3T_1({}^3F) \leftarrow {}^3A_2$ (red) and ${}^3T_2 \leftarrow {}^3A_2$ in the near infrared. The visible emission originates in transitions from 1T_2 to two lower levels (3T_2 , 3A_2) and the infrared emission is from the lowest excited state (3T_2) to the ground state 3A_2 . In all these materials the fluorescence lifetime and quantum efficiency fall off rapidly with increasing temperature. This has been ascribed to an increase in the non-radiative relaxation rate, due to multiphonon relaxation from the emitting state, which competes with the radiative decay process. In contrast to this trend, there is only one luminescence transition in Ni^{2+} -doped LiGa_5O_8 , a spinel-type crystal in which Ni^{2+} replaces Ga^{3+} on octahedral sites [8]. This is the ${}^3T_2 \rightarrow {}^3A_2$ transition indicated in figure 1, which consists of a broad band centred at $1.3 \mu\text{m}$. Furthermore, the lifetime of the Ni^{2+} luminescence remains effectively constant from 15 K to above room temperature, with a decay time of $650 \mu\text{s}$. As the temperature is raised above about 350 K we observe a decrease in the intensity and corresponding decrease in lifetime. The theoretical formula for the non-radiative decay rate, based on the single-configurational-coordinate model, provides a quantitatively correct explanation for the temperature variation of the lifetime [8] and is strong evidence of a high luminescence quantum efficiency. This material is, to our knowledge, unique in that (1) all the emission occurs in the near infrared, and (2) the emission has a high quantum efficiency at room temperature. Our samples were flux-grown, showed non-uniform green colouration, and were of poor optical quality. With good quality samples, tunable laser operation in the region of $1.3 \mu\text{m}$ should be possible.

2.2. $\text{LiGa}_5\text{O}_8 : \text{Co}^{2+}$

Whereas the Ni^{2+} ion has a strong preference for octahedral coordination, the Co^{2+} ion has been studied in both octahedral and tetrahedral coordination [9, 10]. For a Co^{2+} ion (d^7) in octahedral coordination, the fluorescence is usually from the lowest excited state (4T_2) to the ground state (4T_1) [9]. At low temperatures, this emission is strong and provides the basis for low-temperature laser action in several Co^{2+} -doped materials, for example, MgF_2 . As in the case of Ni^{2+} , however, the intensity falls off drastically with increasing temperature. In tetrahedral sites [10] (as in ZnO , ZnAl_2O_4) non-radiative relaxation among excited states is again sufficiently rapid to make the transition from the lowest excited state, 4T_2 , to the ground state, 4A_2 , the most likely emission process. In tetrahedral symmetry, this transition is forbidden by electric dipole radiation. Again, our recent studies have shown that the material LiGa_5O_8 doped with Co^{2+} is unusual in that emission occurs in three distinct transitions from a higher crystal field level in this material. The emission in two of these bands has been briefly described previously [11]. The complete luminescence spectrum, recorded using a germanium detector, extends from 650 nm to beyond 1500 nm and is shown in figure 2. Referring to the schematic energy-level

diagram in figure 2, the crystal field in most Co^{2+} -doped systems with tetrahedral coordination is such that the ${}^2\text{E}$ level lies lower than the ${}^4\text{T}_1({}^4\text{P})$ level. However, in $\text{LiGa}_5\text{O}_8:\text{Co}^{2+}$ the ${}^4\text{T}_1({}^4\text{P})$ level lies below ${}^2\text{E}$ and the spin-allowed transitions ${}^4\text{T}_1({}^4\text{P}) \rightarrow {}^4\text{T}_1({}^4\text{F})$, ${}^4\text{T}_1({}^4\text{P}) \rightarrow {}^4\text{T}_2({}^4\text{F})$, and ${}^4\text{T}_1({}^4\text{P}) \rightarrow {}^4\text{A}_2({}^4\text{F})$ can compete successfully with the non-radiative relaxation processes from this level. At room temperature, the peak wavelengths for the three fluorescence signals are respectively 685 nm, 950 nm and 1.25 μm . The low-temperature lifetime of the luminescence is approximately 200 ns, a very fast lifetime for a transition metal ion, and is a consequence of the lack of inversion symmetry in the tetrahedral site. It remains relatively constant up to room temperature but decreases rapidly between 300 K and 500 K, as does the overall intensity of the luminescence. This system is important and interesting in that it provides several broad transitions in the near infrared, with a common upper level, which could be used to obtain tunable laser action in this region.

2.3. $\text{Mg}_2\text{SiO}_4:\text{Cr}$

Forsterite (Mg_2SiO_4), like alexandrite [1], is a member of the olivine family, with an orthorhombic crystal structure. When doped with Cr ions, it can support laser action over a limited spectral range around 1.2 μm [12, 13]. However, there is some controversy concerning both the Cr valence state and the sites occupied by the Cr ions in this material. We have investigated the spectroscopy of this material doped with various levels of chromium. The complete luminescence spectrum, which is quite sensitive to the wavelength and the polarisation of the excitation [12] is shown in figure 3. At low temperatures, it consists of several sharp features at around 700 nm, some broad bands at about 800 nm and 1000 nm, and further sharp features at 1100 nm. The latter broaden with increasing temperature (see figure 3) and develop into the lasing band at room temperature. The sharp line emission in the 700 nm region corresponds to the ${}^2\text{E} \rightarrow {}^4\text{A}_2$ transition on Cr^{3+} ions which replace Mg^{2+} ions in distinct octahedral sites, one with inversion symmetry (M1) and one with mirror symmetry (M2), as well as a perturbed M1 site, possibly arising from charge compensation. Cr^{3+} ions in such sites have distinct ground-state splittings, measured using electron parametric resonance (EPR) [14], which are resolved in the R_1 emission at low temperature and which clearly identify the Cr^{3+} site. The energy-level structure for the Cr^{3+} ions is similar to that in alexandrite [1] and with increasing temperature the higher-lying ${}^4\text{T}_2$ level becomes populated so that emission from this level dominates the spectrum at room temperature (figure 4). The lifetime varies from 8.9 ns at low temperature to 340 μs at room temperature and can be fitted to a purely radiative model for the emission. The variation of the lifetime τ can be fitted to the expression

$$\frac{1}{\tau} = \frac{f_B + 3f_T \exp(-\Delta/kT)}{1 + 3 \exp(-\Delta/kT)}$$

with values of 114 s^{-1} and 10^4 s^{-1} for the radiative rates f_B and f_T from the ${}^2\text{E}$ and ${}^4\text{T}_2$ levels, and 450 cm^{-1} for the energy separation Δ between ${}^2\text{E}$ and ${}^4\text{T}_2$. We find no evidence for any energy transfer from Cr^{3+} ions to the i.r. lasing centre, which was suggested by other workers [12], or for any non-radiative component in the emission from these ions up to room temperature. Despite its high efficiency, this system is prevented from lasing due to absorption by another centre (assigned by several workers to Cr^{4+} in tetrahedral Si sites [12, 13]) which is the basis for the

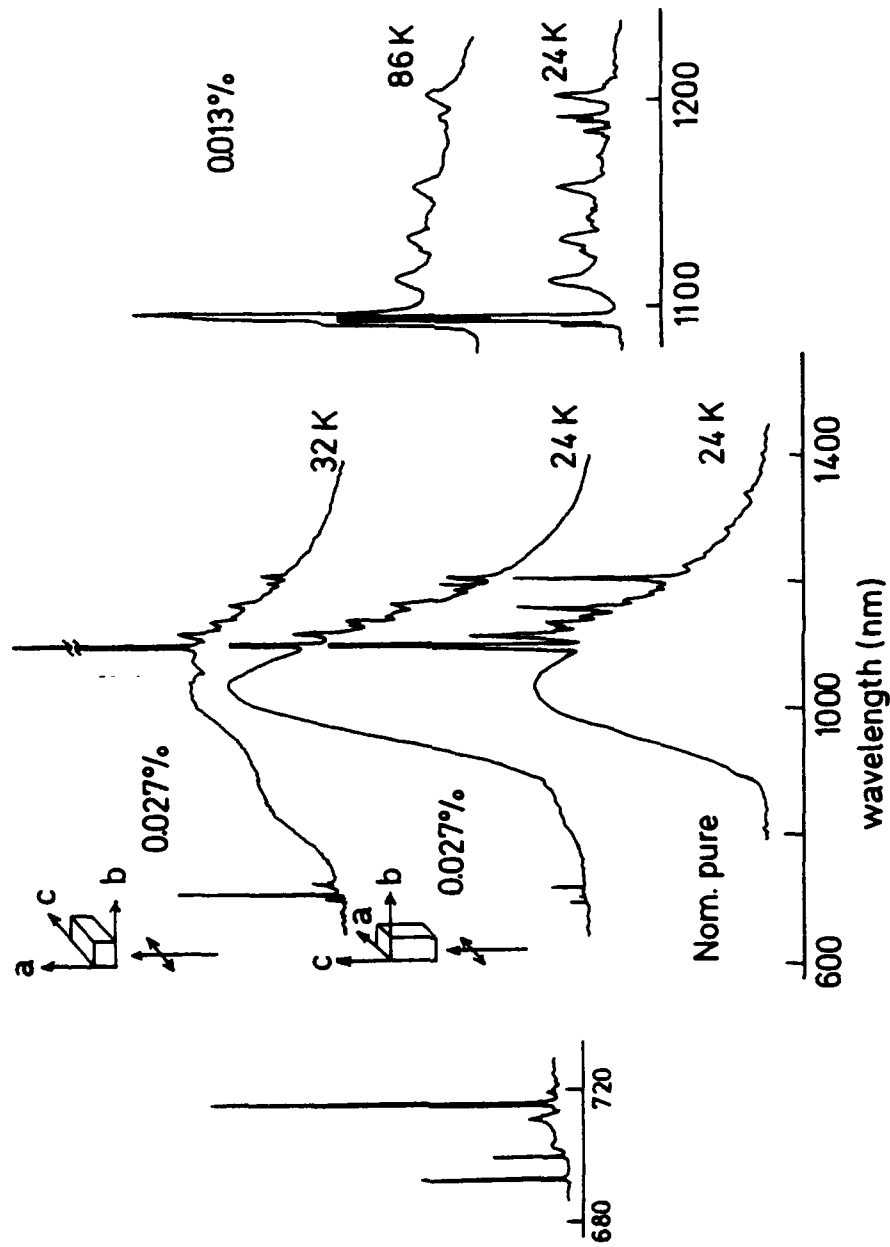


Figure 3. The low-temperature emission from Mg₂SiO₄ (forsterite) doped with chromium excited by an argon-ion laser (all lines). The sharp features at ~700 nm and ~1100 nm are shown at higher resolution.

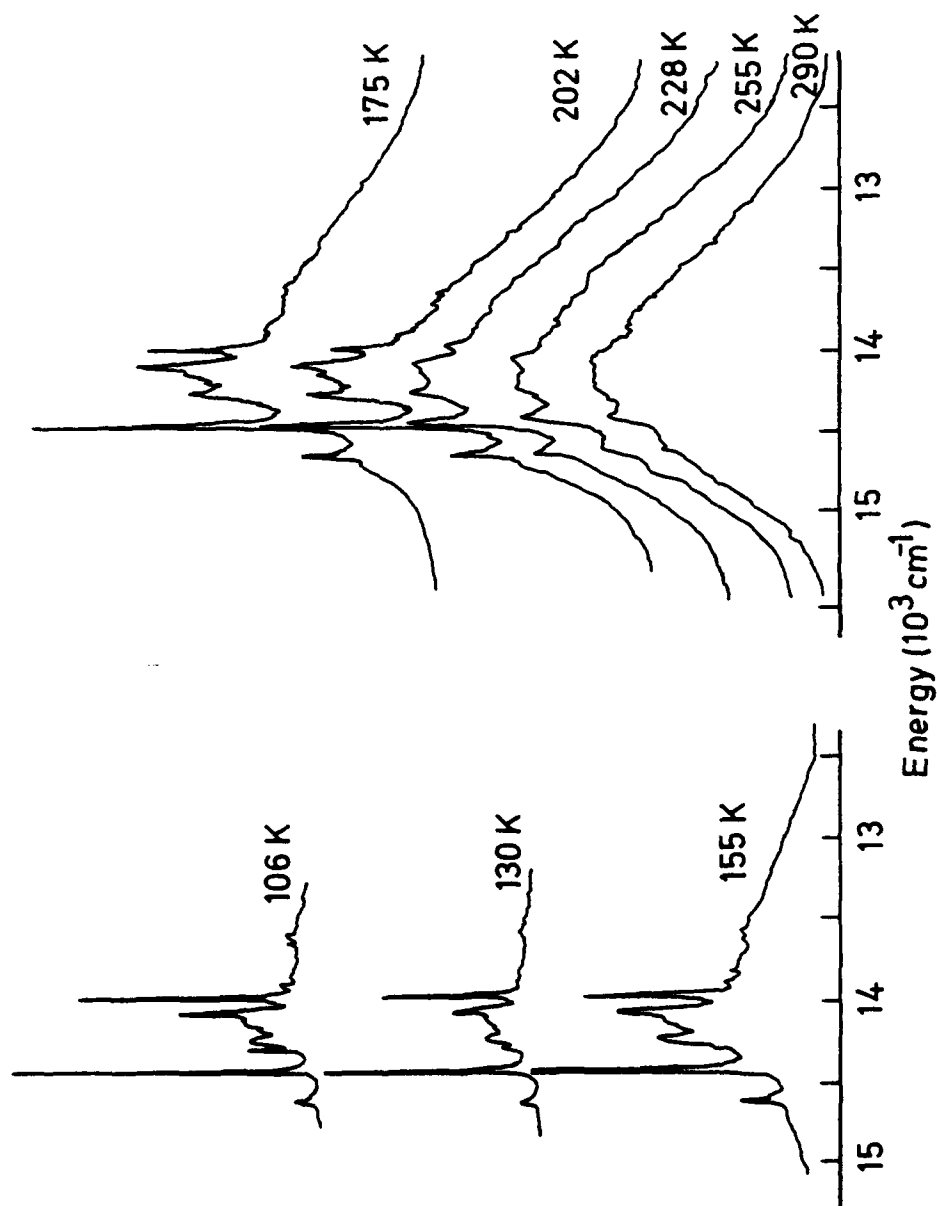


Figure 4. The luminescence from Cr³⁺ centres in forsterite at various temperatures. The chromium doping level was 0.027%.

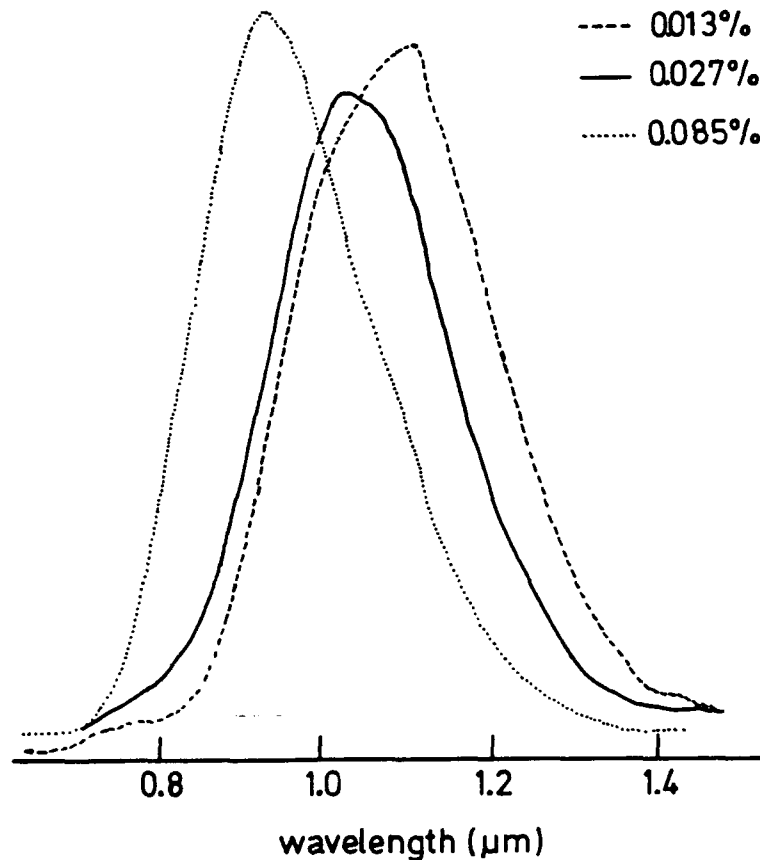


Figure 5. The near-infrared emission band in chromium-doped forsterite for different concentrations of chromium excited by an argon-ion laser at 290 K (all lines). Tunable laser operation has been obtained over about 75 nm centred on 1.2 μm [12].

demonstrated laser action in this material in a band centred at 1.2 μm . (The latter may be pumped almost anywhere in the visible and even at 1.06 μm .) The energy level diagram for Cr^{4+} in a tetrahedral site is similar to that for Ni^{2+} in an octahedral site and the lasing emission is tentatively assigned to the ${}^3\text{T}_2 \rightarrow {}^3\text{A}_2$ transition in this system [13]. The structured low-temperature spectrum shown in figure 3 becomes a broad band at room temperature and it peaks at different wavelengths around 1.1 μm depending on the excitation wavelength and on the Cr concentration (figure 5). Emission in this wavelength region, and the measured lifetime of 2.5 μs at room temperature, is difficult to reconcile with the known spectroscopic properties of Cr^{3+} ions in oxide crystals. The identification of the lasing centre in this material remains an interesting problem for further study. We note that similar laser action, with a tuning range of more than 300 nm and extending to beyond 1.2 μm in some

cases, has recently been reported by Kaminskii [15] in a range of Cr-doped oxide crystals. If indeed these results are due to Cr^{4+} then this ion may prove to be a worthwhile laser centre in its own right which can extend the range beyond that of Cr^{3+} in the infrared and new crystal hosts should be sought which can stabilise this oxidation state.

3. Conclusion

The spectroscopy of three materials with potential as laser media in the near infrared has been described. For the systems based on LiGa_5O_8 , further improvements in sample quality and additional spectroscopic studies will be necessary to assess their viability as tunable laser systems. The nature of the lasing centre in forsterite: Cr is still not established with certainty and much work remains to be done in unravelling the many complex centres in this material. Such studies, in this relatively simple lattice, will provide guidance in interpreting the spectroscopy of the more complex chromium-doped materials recently reported [15].

Acknowledgments

This research work was supported in part by the Air Force Office of Scientific Research, Air Force Systems Command, USAF, under grant number AFOSR-88-0355. The Ge detector was obtained through a grant from the University College Galway Development Fund which we acknowledge with gratitude. We wish to thank Dr H. Rager, Universität Marburg, West Germany, for several samples of forsterite used in these studies.

References

- [1] WALLING, J. C., PETERSON, O. G., JENSEN, H. P., MORRIS, R. C., and O'DELL, E. WAYNE, 1980, *IEEE J. quant. Electron.*, **16**, 1302.
- [2] CAIRD, J. A., PAYNE, S. A., STAVER, P. R., RAMPONI, A. J., CHASE, L. L., and KRUPKE, W. E., 1988, *IEEE J. quant. Electron.*, **24**, 1077.
- [3] MOULTON, P. F., 1986, *Laser Handbook* edited by M. Bass and M. L. Stitch (New York: Elsevier), pp. 203-285.
- [4] JOHNSON, L. F., GUGGENHEIM, H. J., BAHNCK, D., and JOHNSON, A. M., 1983, *Optics Lett.*, **8**, 371.
- [5] MOULTON, P. F., 1986, *IEEE J. quant. Electron.*, **21**, 1582.
- [6] VEHSE, W. E., LEE, K. H., YUN, S. I., and SIBLEY, W. A., 1975, *J. Lumin.*, **10**, 149.
- [7] SUZUKI, Y., SIBLEY, W. A., EL BAYAUMI, O. H., ROBERTS, T. M., and BENDON, B., 1987, *Phys. Rev. B*, **35**, 4472.
- [8] DONEGAN, J. F., BERGIN, F. J., GLYNN, T. J., IMBUSCH, G. F., and REMEIKA, J. P., 1986, *J. Lumin.*, **35**, 57.
- [9] MOULTON, P. F., 1982, *IEEE J. quant. Electron.*, **18**, 1185.
- [10] FERGUSON, J., WOOD, D. L., and VAN UITERT, L. G., 1969, *J. chem. Phys.*, **51**, 2904.
- [11] DONEGAN, J. F., BERGIN, F. J., IMBUSCH, G. F., and REMEIKA, J. P., 1984, *J. Lumin.*, **31/32**, 278.
- [12] PETRICEVIC, V., GAYEN, S. G., and ALFANO, R. R., 1988, *Appl. Phys. Lett.*, **53**, 2590; 1989, *Optics Lett.*, **14**, 612.
- [13] VERDUN, H. R., THOMAS, L. M., ANDROUSKAS, D. M., MCCOLLUM, T., and PINTO, A., 1989, *Appl. Phys. Lett.*, **53**, 2593.
- [14] RAGER, H., 1977, *Phys. Chem. Minerals*, **1**, 371.
- [15] KAMINSKII, A., 1988, *Proceedings of the International School on Excited States of Transition Elements (Poland, 1988)* (New York: World Scientific), pp. 669-701.

Infra-red luminescence of iron-doped synthetic forsterite

G. Walker

Department of Pure and Applied Physics, UMIST, Manchester M60 1QD, UK

T.J. Glynn

Physics Department, University College, Galway, Ireland

Received 29 January 1992

Revised 23 March 1992

Accepted 25 March 1992

Luminescence spectra of an iron-doped (0.2%) synthetic crystal of forsterite have been measured at low temperature (15 K). These show several zero-phonon lines at 813, 1025, 1093 and 1134 nm, all with phonon side bands. The emission at 1093 nm is due to chromium (Cr^{4+}) and occurs also in both nominally pure crystals and chromium-doped samples. However, the 813 nm line is ascribed to Fe^{3+} ions, probably in tetrahedral (Si) sites, on the basis of the measured lifetime (15.5 ± 0.5 ns) and the analysis of excitation spectra. The 1025 and 1134 nm lines have measured lifetimes of 8.4 and $5.7 (\pm 0.5)$ μs respectively at 20 K and are similar in other respects. It is suggested that these lines may be due to Fe^{2+} ions in octahedral (Mg) sites.

1. Introduction

Recently, chromium-doped forsterite (Mg_2SiO_4) has been shown to exhibit tunable laser action in the near infra-red, in the range 1100–1300 nm, and consequently has been the subject of extensive studies [1–6]. Although Cr^{3+} emission is evident in this material, the emission responsible for laser action in the near infra-red is thought to be due to Cr^{4+} , an unusual valence state of chromium, substituting for Si [1–6]. Apart from a detailed study of Mn^{2+} luminescence in forsterite [7], there are few, if any, reports of luminescence of other transition-metal ions in this host material. Here we present spectra of an iron-doped forsterite (0.2 wt% Fe) and provide evidence of infra-red emission from both Fe^{3+} and Fe^{2+} ions in this material.

Fe^{3+} is known to exhibit emission in the red or near infra-red in a variety of materials, including

naturally occurring feldspars, usually substituting for Al^{3+} or Ga^{3+} . Luminescence from tetrahedrally coordinated Fe^{3+} is more common [8–11], but emission from octahedrally coordinated Fe^{3+} has also been reported [12–14]. On the other hand, reports of Fe^{2+} luminescence are comparatively rare; emission from tetrahedrally coordinated Fe^{2+} in III–V semiconductors has been reported at around 3000 nm [15,16] but emission bands ascribed to Fe^{2+} in various other host materials may have other origins. However, absorption spectra of Fe^{2+} in olivines (of which forsterite is a relatively iron-free variety) have been studied in detail [17,18] but usually in samples with high concentrations of iron ranging from a few percent to over 90%. Strong broad absorption bands in the range 800–1400 nm have been assigned to Fe^{2+} ions in both metal cation sites (M1 and M2); the most prominent peak close to 1 μm is due to Fe^{2+} in M2 sites.

Olivines show very weak absorption in the range 550–800 nm, but show strong absorption in the

Correspondence to: Dr. G. Walker, Department of Pure and Applied Physics, UMIST, Manchester M60 1QD, UK.

blue and UV due to charge transfer bands. There are also some sharp spin-forbidden transitions in the blue region which have been assigned to both Fe^{2+} and Fe^{3+} by various authors.

2. Cation site symmetries

Both the degree and type of distortion exhibited by the available cation sites in forsterite from simple cubic (tetrahedral or octahedral) symmetry have a pronounced effect on the energy levels of substitutional transition-metal impurities. The crystal structure of forsterite is well-known and has been described many times elsewhere [19,20]. It belongs to the orthorhombic space group $Pbnm$ and consists of separate silica tetrahedra linked by divalent metal cations (Mg^{2+} in the case of pure forsterite) in two inequivalent, distorted octahedral sites. The smaller of these, usually designated M1, retains its centre of symmetry and has C_1 point symmetry. The slightly larger M2 site retains a mirror plane and is of C_2 symmetry although a C_{2v} pseudosymmetry has been found to be useful in spectroscopic analyses of polarised spectra of Mn^{2+} [7]. The Si tetrahedral site is also of C_2 symmetry, but is much smaller than the octahedral M1 and M2 sites in terms of bond lengths [20]. The removal of degeneracy from the E and T states of simple cubic symmetry is therefore to be expected and in view of the degree of distortion quite large splittings may occur.

3. Experimental

The iron-doped single crystal studied was kindly provided by Dr. Rager of the University of Marburg, Germany. The crystal was clear with a slight yellow tinge and measured approximately $3 \times 4 \times 7$ mm after cutting and polishing; the crystallographic axes were roughly parallel to the crystal edges. A similar undoped colourless crystal was also studied for comparison purposes and found to contain trace amounts of chromium and manganese which gave rise to luminescence emission although the manganese was only evident in

cathodoluminescence. Luminescence emission spectra were measured at various temperatures down to about 15 K using a closed-cycle helium cryostat. Excitation was by means of either an argon-ion laser (458, 488 or 515 nm lines) or an argon-ion pumped dye laser (616 nm), at power levels ranging from 50–500 mW. A 1 m grating spectrometer was used and detection was by either a cooled germanium detector (North Coast Optical Co.) or by a cooled photomultiplier with an S1 type photocathode. Lock-in amplification was employed for spectral measurements but photon-counting techniques and a multichannel analyser were used for lifetime measurements with the S1 photomultiplier. Excitation spectra of the long-lived emission were determined using a "double-chopper" technique and a xenon arc or tungsten-halogen lamp as a continuum source as described elsewhere [7].

4. Emission and excitation spectra of Fe^{3+} in forsterite

When excited by 200 mW of the 488 nm argon-ion line, the overall emission spectrum between 700 and 1400 nm at 15 K shows what appears to be at least four separate zero-phonon lines plus phonon side bands. In addition there is a very broad emission band underlying these with a maximum at around 1100 nm (9100 cm^{-1}). The first of these apparent zero-phonon lines with side band is at 813 nm (12300 cm^{-1}) and is shown in detail in fig. 1(a); it persists with decreasing intensity up to at least 200 K. Lifetime measurements at 20 K reveal that this emission line and its phonon side band have a lifetime of 15.5 ± 0.5 ms. However, lifetime measurements and phase-tuning experiments in which the strong zero-phonon line is phase-tuned out to give a zero or even negative signal show that there are two other weaker peaks at 850 and 866 nm (11770 and 11550 cm^{-1}) which are buried in the phonon side band of the 813 nm peak (fig. 1(b)). These weaker peaks have much shorter lifetimes and, although these are difficult to measure accurately, they are certainly of the order of 1 ms.

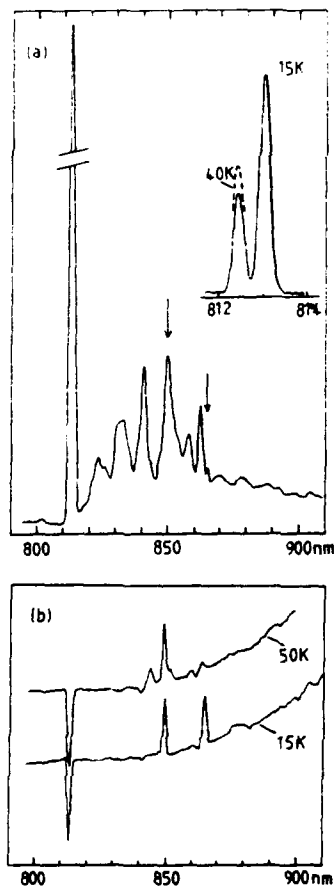


Fig. 1. (a) Emission spectrum of Fe^{3+} at 15 K showing a strong zero-phonon peak at 813 nm. 200 mW of 488 nm excitation was used, chopped at a frequency of 7 Hz. The insert shows the zero-phonon peak to be a temperature dependent doublet at this resolution (0.2 nm). The phonon side band overlaps two further zero-phonon peaks indicated by arrows at 850 and 866 nm. These peaks are more evident when the excitation is modulated at a higher frequency (e.g. 90 Hz) for which the main emission suffers attenuation. (b) Phase-tuned spectra in which the main zero-phonon peak is almost phase-tuned out on the lock-in amplifier giving a small negative signal. The 850 and 865 nm peaks show a positive signal indicating a significantly different lifetime from the main emission.

Higher resolution spectra show that the primary zero-phonon line at 813 nm is at least a doublet; the higher energy component increases in intensity

relative to the lower energy component with increasing temperature indicates that excited state splitting rather than ground state splitting is responsible. In view of the large number of known phonon modes in forsterite [21], it is difficult to determine whether the side band contains several phonon replicas or is a single-phonon side band. However, since nearly 40% of the emission intensity is in the zero-phonon line, the Huang-Rhys factor is around unity and the side band is probably single-phonon. The long lifetime is clearly indicative of a spin-forbidden transition; there are three obvious impurity ions which could be responsible, namely Cr^{3+} , Mn^{2+} and Fe^{3+} . However, the 813 nm line and side band are not evident in the spectra of nominally pure (i.e. undoped) samples which show evidence of trace amounts of chromium and manganese, nor in chromium or nickel-doped samples. We therefore assign this emission to Fe^{3+} , although the Huang-Rhys factor is unusually low for a d^5 ion. Electron spin resonance measurements carried out on this and similar crystals [22,23] indicate that Fe^{3+} is present in both octahedral (mainly M2) and tetrahedral (Si) sites, in roughly equal amounts. The spectral position of the emission suggests that either the Fe^{3+} ion is in a small tetrahedral site or a large octahedral site; i.e. the emission could be due to Fe^{3+} in either of the sites in which it has been detected by ESR. In order to gain more information on this point a luminescence excitation spectrum of this emission was determined and is shown in fig. 2. The spectrum, although showing many of the sharp features associated with d^5 ions, does not give the usual clear indication as to the site occupancy of the d^5 ion. However, the very strong sharp peak at 405 nm ($24\,690\text{ cm}^{-1}$) which shows signs of being a doublet, is similar to the dominant ${}^4\text{E}(\text{D})$ peak present in the excitation spectra of tetrahedrally coordinated Fe^{3+} in feldspars, aluminates and other materials. The problem is locating the ${}^4\text{E}(\text{G})$, ${}^4\text{A}_1(\text{G})$ states which do not give rise to very sharp peaks in the spectra of tetrahedrally coordinated Fe^{3+} as they do in spectra of octahedrally coordinated Fe^{3+} and Mn^{2+} [10,13]. The sharp features at 616 nm ($16\,230\text{ cm}^{-1}$) are unlikely to be associated with these states; the depression of the Racah parameters B and C from their free-ion values would

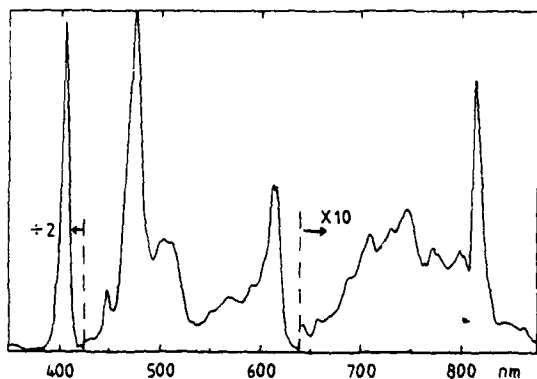


Fig. 2. Excitation spectrum of the Fe^{3+} (813 nm) emission. The spectrum is corrected for spectral variations in excitation intensity, and was evaluated from spectra using either a xenon arc or tungsten halogen source. A photomultiplier with an extended S20 response was used for detection with either a Wratten 87 filter or 820 nm interference filter (FWHM 40 nm).

have to be very large indeed. If the emission was in fact due to Fe^{3+} in the large octahedral M2 sites, a large depression from free-ion values would not be expected. For example, the ${}^4\text{E}(\text{G})$, ${}^4\text{A}_1(\text{G})$ peaks in the absorption spectrum of Fe^{3+} in andradite garnet occur at about 450 nm (22200 cm^{-1}) [24], and even in tetrahedral sites the corresponding transitions occur in the region 450–480 nm ($22200\text{--}20800\text{ cm}^{-1}$) [8–11]. In view of the small Huang–Rhys factor the sharp peaks at 616 nm may be zero-phonon lines connected with the split ${}^4\text{T}_2$ level. The d^5 spectrum could then be that of Fe^{3+} in a tetrahedral (Si) site. A best fit to a d^5 ligand-field diagram was therefore attempted using cubic, strong-field matrices on the basis of the assignment: ${}^4\text{E}(\text{D})\text{--}405\text{ nm}$ (24690 cm^{-1}), ${}^4\text{A}_1$, ${}^4\text{E}(\text{G})\text{--}510\text{ nm}$ (19610 cm^{-1}). Such an analysis gave values for the Racah parameters B and C of 726 and 2470 cm^{-1} respectively and a ligand-field strength 10Dq of around 8000 cm^{-1} using “centre of gravity” values for the positions of the split ${}^4\text{T}_1$ and ${}^4\text{T}_2$ states of 13300 and 17200 cm^{-1} respectively (see fig. 3).

Attempts to obtain a reasonable fit using several other possible assignments proved unsuccessful. In particular, it proved difficult to make a sensible assignment that yielded a value of 10Dq high enough to be compatible with octahedral coordination of Fe^{3+} .

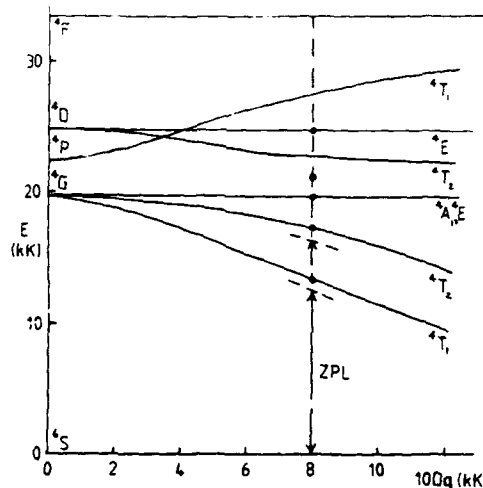


Fig. 3. A d^5 ligand-field diagram for Fe^{3+} in forsterite with Racah parameter values of $B = 726\text{ cm}^{-1}$ and $C = 2470\text{ cm}^{-1}$, and evaluated using cubic strong-field matrices. A best fit to experimental values is obtained at $10\text{Dq} = 8000\text{ cm}^{-1}$. (The unit $1\text{ kK} = 1000\text{ cm}^{-1}$.) However, because of distortions from cubic symmetry, the T states are split and the positions of the lowest split levels for the first two excited states are shown, the double-headed arrow indicating the transition energy of the zero-phonon line as measured in emission and excitation. Another arrow shows the position of the probable zero-phonon line of the lowest component of the ${}^4\text{T}_2(\text{G})$ state as shown in excitation spectra (see fig. 2).

The possibility that the excitation spectrum of fig. 2 could be a composite one, involving more than one type of centre, was also explored by using different isolation filters, different optical chopping frequencies and looking for any temperature dependence of the spectrum; no evidence was found to support this contention. A further possibility is that some of the features on the excitation spectrum may be due to Cr^{4+} absorption, since the 1093 nm (9150 cm^{-1}) line in the emission spectrum has been ascribed to this ion (see below). Nevertheless, none of the major sharp spectral features in this spectrum can be correlated with such features in the Cr^{4+} absorption spectrum [4,5]. As for the other apparent zero-phonon lines at 850 and 866 nm , these could be either satellite lines due to crystal inhomogeneities or tetrahedrally-coordinated Fe^{3+} adjacent to point defects. However there is also the possibility that one or both could be associated

with Fe^{3+} ions in octahedral coordination. The 850 nm line also shows doublet character at higher temperatures (fig. 1(c)) but the somewhat shorter-lived 866 nm line disappears at such temperatures.

5. Emission spectra of Fe-doped forsterite in the region 900–1300 nm

At temperatures below around 100 K there appear to be at least three zero-phonon peaks with side bands and an underlying broad emission band between 900 and 1300 nm (see fig. 4). The peak at 1093 nm can be recognized as the emission which has been ascribed to chromium (in fact to Cr^{4+} in Si sites [1–6]). This peak is, as previously shown [4], at least a triplet. It also occurs in spectra of the nominally "pure" crystal as well as in chromium-doped crystals. The underlying broad band may also be due to chromium – possibly Cr^{3+} in low-field sites. However, the other sharp peaks at 1025 and 1134 nm (9756 and 8818 cm^{-1}) are peculiar to the iron-doped crystal. Decay time measurements yield lifetimes of 8.4 and $5.7 (\pm 0.5) \mu\text{s}$ respectively

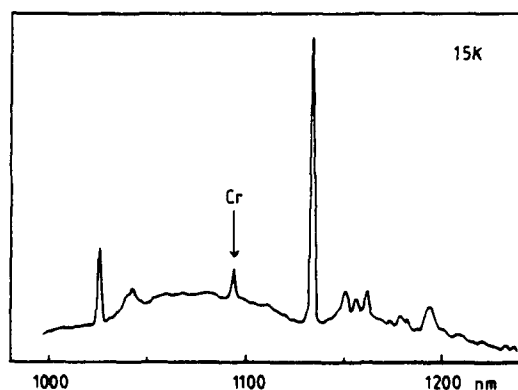


Fig. 4. The emission spectrum of Fe-doped forsterite at 15 K in the range 1000–1250 nm using 488 nm excitation. The peak due to chromium is not evident if 458 nm excitation is used instead but becomes the dominant peak when 515 nm excitation is employed. A cooled germanium detector was used. Intensities are not corrected for spectral response of the instrumentation but the latter shows only a weak spectral dependence over this range.

at 20 K suggesting that these are spin-allowed transitions and therefore are unlikely to originate from Fe^{3+} ions. Electron spin resonance measurements suggest that most of the iron present in the crystal is in fact in the Fe^{2+} rather than the Fe^{3+} valence state [23] and, as already mentioned, Fe^{2+} ions are to be found in both M1 and M2 sites. Emission from Fe^{2+} ions in any host material is not a common event. Nevertheless, the luminescence is in a spectral region where Fe^{2+} emission might be expected on the basis of known absorption spectra of Fe^{2+} in olivines. We might expect emission from Fe^{2+} in the M2 site to be the more intense on account of the lack of inversion symmetry. It is tempting to ascribe the 1025 and 1134 nm emission lines to Fe^{2+} in M1 and M2 sites. However, although the evidence suggests that these emissions may be due to Fe^{2+} in octahedral sites, the actual sites of occupation cannot as yet be ascertained. Further evidence that Fe^{2+} centres may be responsible is found by varying the wavelength of excitation. The 1025 and 1134 nm emission lines are efficiently excited by the 458 nm Ar^+ line whereas the chromium emission at 1093 nm is difficult to detect at this excitation wavelength. Excitation at 488 nm is less efficient but the Fe-related emission lines are still much stronger than the chromium line (see fig. 4). However, with 515 nm excitation the chromium line is stronger than the Fe-related lines which are now much less efficiently excited (≈ 2 cf. 488 nm excitation) although the relative intensities of the 1025 and 1134 nm lines appear to be independent of excitation wavelength in this region. Using dye laser excitation at 616 nm the 1025 and 1134 nm emission lines are entirely absent from the spectrum which is then dominated by Fe^{3+} and chromium emission. Fe^{2+} absorption is very weak at this wavelength and increases as the wavelength becomes shorter, in agreement with the known absorption spectrum of Fe^{2+} in olivines. Excitation spectra, particularly polarised spectra, of the 1025 and 1134 nm lines would be very helpful but these are difficult to obtain using techniques presently available.

High-resolution emission spectra of the zero-phonon lines were measured at different temperatures between 15 and 100 K. The 1134 nm line was found to have at least four components but may

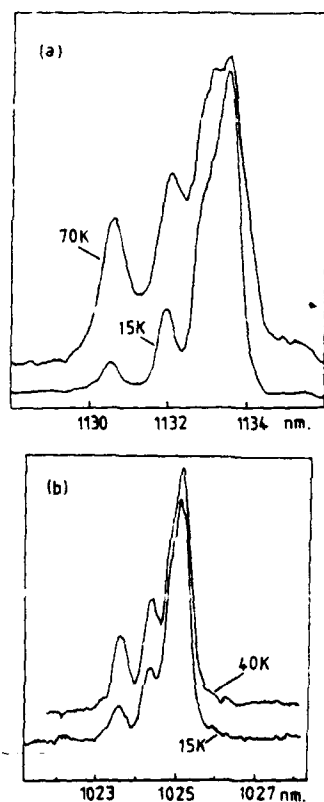


Fig. 5. Fine structure of (a) the 1135 nm and (b) the 1025 nm zero-phonon emissions showing the variation with temperature of the intensity ratios of component peaks. Note the similarity of (a) and (b) although the overall splitting is larger in (a).

contain more features which are unresolved (fig. 5). The increase in relative intensity of the higher energy (shorter wavelength) components with increase in temperature indicates excited-state splitting rather than ground-state splitting. In fact, there is little evidence of any appreciable ground-state splitting at this resolution (2 cm^{-1}). The 1025 nm line appears to have a similar excited-state splitting but the resolution of the spectrum reveals only three definite components although there is a hint that four or five components may be present as in the 1134 nm line.

The transition responsible for the emission in Fe^{2+} in the pure octahedral case would be

${}^5E_g(D) - {}^5T_{2g}(D)$. However, there is evidence from absorption spectra that the degeneracy of both the 5E and 5T_2 states are removed by the distortions from octahedral symmetry and, as previously indicated, this is to be expected from the known site symmetries. Excitation spectra of Mn^{2+} in M2 sites in forsterite also indicate appreciable splitting of octahedral states in this site [7]. Furthermore spin-orbit splitting of both excited and ground state could result in a large number of components. Both excited and ground states are quintets but although the spectra indicate a possible quintet excited state, they give no indication of appreciable ground-state splitting. There is little in the literature that is of help: Fe^{2+} ions in III-V semiconductors are in tetrahedral coordination and hence the ground state and first excited state are reversed with respect to octahedral coordination. However, a detailed analysis of the ${}^4E - {}^4T_2(D)$ luminescence transition of tetrahedrally coordinated Cr^{2+} in GaAs at 1476 nm has been done [25]. This analysis makes it clear that only very high resolution spectra at very low temperatures can resolve the fine details of spin-orbit split states. Nevertheless, there is a degree of similarity in the splitting found. The phonon side band of the 1025 nm line has only one clearly discernible peak at about 160 cm^{-1} . However, the side band of the 1134 nm line is more detailed with apparent phonon modes at 140, 170, 210, 340 and 440 cm^{-1} . As mentioned before, it is difficult to deduce much from the phonon side bands on account of the many possible modes in forsterite except to note that modes of frequency higher than about 400 cm^{-1} do not involve metal cations but are vibrational modes of the silica tetrahedra.

6. Conclusions

The 813 nm emission line and associated phonon side band are due to Fe^{3+} ions, most probably in tetrahedral (Si) sites, the long luminescence lifetime being indicative of the spin-forbidden nature of transitions on d^5 ions. The excitation spectrum of this emission is consistent with that of a d^5 ion in a tetrahedral site and calculation of the cubic

ligand-field parameter $10Dq$ based on likely band assignments provides further evidence that Fe^{3+} ions are responsible. Although the zero-phonon line persists up to around 200 K, it is not evident at room temperature and the emission suffers temperature quenching, as is usual for Fe^{3+} , beginning at about 100 K.

Well-defined phonon modes in the single-phonon side band up to 700 cm^{-1} are compatible with tetrahedral coordination in a Si site. Other minor emission peaks, which are masked by the side band, are also probably due to Fe^{3+} in other environments, the lifetimes also being fairly long ($\sim 1\text{ ms}$).

The origins of the 1025 and 1134 nm lines and side bands are less certain but the experimental evidence so far points to the possibility that Fe^{2+} ions in octahedral sites may be responsible. The two emission lines have a number of features in common, similar but not identical lifetimes, similar spectral absorption characteristics, and similar, but again not identical, zero-phonon splitting patterns. These are in contrast to the completely different properties of the Fe^{3+} emission in these respects.

Acknowledgements

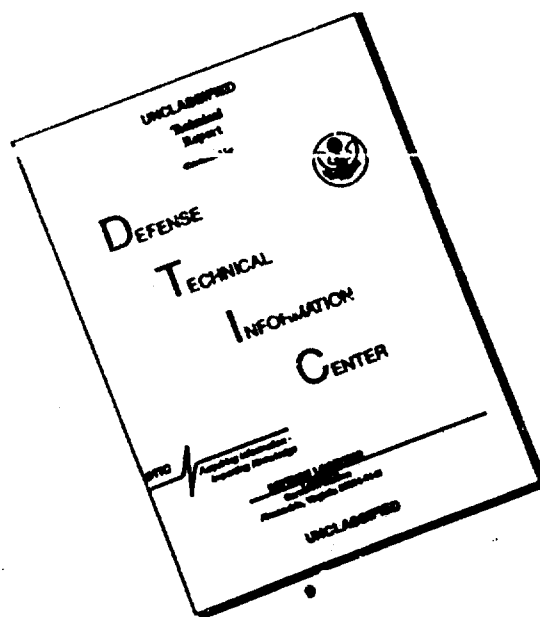
We are greatly indebted to Dr. H. Rager of the University of Marburg, Germany, for the provision of both doped and undoped crystals of forsterite, and for ESR spectra and other information regarding these crystals. We thank Prof. G.F. Imbusch for encouragement and helpful discussions and Dr. G. Morgan for discussions regarding experimental lifetime measurements. We are also grateful to B. Kelly, D. Staunton and P. McBride for experimental assistance at various stages of the work. This work was supported in part by the U.S. Air Force Office of Scientific Research under grant number AFOSR-88-0335. The germanium detector was provided through a grant from the University

College Galway Development Fund which we gratefully acknowledge.

References

- [1] V. Petricevic, S.K. Gayen and R.R. Alfano, *Appl. Phys. Lett.* 53 (1988) 2590.
- [2] H.R. Verdun, L.M. Thomas, D.M. Andrauskas, T. McCollum and A. Pinto, *Appl. Phys. Lett.* 53 (1988) 2593.
- [3] R. Moncorge, G. Cormier, D.J. Simpkin and J.A. Capobianco, *OSA Proc. Tunable Solid State Lasers*, 15 (1989) 93; *IEEE J. Quantum Electron.* 27 (1991) 114.
- [4] W. Jia, H.L. Liu, S. Jaffe and W.M. Yen, *Phys. Rev. B* 43 (1991) 5234.
- [5] H. Rager, M. Taran and V. Khomenko, *Phys. Chem. Minerals* 18 (1991).
- [6] T.J. Glynn, G.F. Imbusch and G. Walker, *J. Lumin.* 48&49 (1991) 541.
- [7] G.R. Green and G. Walker, *Phys. Chem. Minerals* 12 (1985) 271.
- [8] G.T. Pott and B.D. McNicol, *J. Chem. Phys.* 56 (1972) 5246.
- [9] C.Z. Van Doorn, D.J. Schipper and P.T. Bolwijn, *J. Electrochem. Soc.* 119 (1972) 85.
- [10] D.J. Telfer and G. Walker, *Nature* 258 (1975) 694; *Modern Geology* 6 (1978) 199.
- [11] C. McShera, P.J. Colleran, T.J. Glynn, G.F. Imbusch and J.P. Remeika, *J. Lumin.* 28 (1983) 41.
- [12] G.T. Pott and B.D. McNicol, *J. Lumin.* 6 (1973) 225.
- [13] D.J. Telfer and G. Walker, *J. Lumin.* 11 (1976) 315.
- [14] G. O'Connor, C. McDonagh and T.J. Glynn, *J. Lumin.* 48&49 (1991) 545.
- [15] W.H. Koschel, U. Kaufmann and S.G. Bishop, *Solid State Comm.* 21 (1977) 1069.
- [16] S.G. Bishop, D.J. Robbins and P.J. Dean, *Solid State Comm.* 33 (1980) 119.
- [17] R.G. Burns, *Mineralogical Applications of Crystal Field Theory* (CUP, 1970).
- [18] W.A. Runciman, D. Sengupta and J.R. Gourley, *Amer. Mineral.* 58 (1973) 451; 59 (1974) 630.
- [19] J.D. Birlie, G.V. Gibbs, P.B. Moore and J.V. Smith, *Amer. Mineral.* 53 (1968) 807.
- [20] J.R. Smyth and R.M. Hazen, *Amer. Mineral.* 58 (1973) 588.
- [21] K. Iishi, *Amer. Mineral.* 63 (1978) 1198.
- [22] J.M. Gaite and S.S. Hafner, *J. Chem. Phys.* 80 (1984) 2247.
- [23] H. Rager, private communication.
- [24] R.G. Burns, *Can. Spectrosc.* 17 (1972) 51.
- [25] F. Voillot, J. Barrau, M. Brousseau and J.C. Brabant, *Phys. Stat. Sol. (a)* 64 (1981) K39.

DISCLAIMER NOTICE



THIS DOCUMENT IS BEST QUALITY AVAILABLE. THE COPY FURNISHED TO DTIC CONTAINED A SIGNIFICANT NUMBER OF PAGES WHICH DO NOT REPRODUCE LEGIBLY.